



NAVAL POSTGRADUATE SCHOOL

MONTEREY, CALIFORNIA

THESIS

**THRUST AUGMENTATION STUDY OF CROSS-FLOW
FAN FOR VERTICAL TAKE-OFF AND LANDING
AIRCRAFT**

by

Ing Khang Yeo

September 2012

Thesis Advisor:
Second Reader:

Garth V. Hobson
Anthony J. Gannon

Approved for public release; distribution is unlimited

THIS PAGE INTENTIONALLY LEFT BLANK

REPORT DOCUMENTATION PAGE			Form Approved OMB No. 0704-0188	
Public reporting burden for this collection of information is estimated to average 1 hour per response, including the time for reviewing instruction, searching existing data sources, gathering and maintaining the data needed, and completing and reviewing the collection of information. Send comments regarding this burden estimate or any other aspect of this collection of information, including suggestions for reducing this burden, to Washington headquarters Services, Directorate for Information Operations and Reports, 1215 Jefferson Davis Highway, Suite 1204, Arlington, VA 22202-4302, and to the Office of Management and Budget, Paperwork Reduction Project (0704-0188) Washington DC 20503.				
1. AGENCY USE ONLY (Leave blank)		2. REPORT DATE September 2012	3. REPORT TYPE AND DATES COVERED Master's Thesis	
4. TITLE AND SUBTITLE Thrust Augmentation Study of Cross-Flow Fan for Vertical Take-Off and Landing Aircraft			5. FUNDING NUMBERS TDSI/11-007/1A - NPS	
6. AUTHOR(S) Ing Khang Yeo				
7. PERFORMING ORGANIZATION NAME(S) AND ADDRESS(ES) Naval Postgraduate School Monterey, CA 93943-5,000			8. PERFORMING ORGANIZATION REPORT NUMBER	
9. SPONSORING / MONITORING AGENCY NAME(S) AND ADDRESS(ES) TDSI - National University of Singapore 21 Lower Kent Ridge Road Singapore, 119077			10. SPONSORING/MONITORING AGENCY REPORT NUMBER	
11. SUPPLEMENTARY NOTES The views expressed in this thesis are those of the author and do not reflect the official policy or position of the Department of Defense or the U.S. Government. IRB Protocol number ____N/A____.				
12a. DISTRIBUTION / AVAILABILITY STATEMENT Approved for public release; distribution is unlimited			12b. DISTRIBUTION CODE	
13. ABSTRACT (maximum 200 words) Vertical Take-Off and Landing (VTOL) has primarily seen research and development in the two traditional fields, namely the rotary wing and jet propulsion, with each seeking incremental improvements in thrust generation and fuel efficiency, respectively. In recent years, there has been increasing interest in the viability of the Cross-Flow Fans (CFF) being the primary source of aircraft propulsion. There has been measured success in horizontal flight; however, VTOL propulsion with CFFs remains elusive. The current study seeks to determine the feasibility of combining two CFFs in a back-to-back configuration that could augment the thrust generated, thus making VTOL a reality. Making use of an optimized CFF housing, the research aimed to maximize the thrust generated in the above mentioned configuration by varying the gap between the CFFs. Computational fluid simulations of the dual CFF configuration was performed using ANSYS CFX to find the thrust generated as well as the optimal operating point. Analysis was done at three different speeds (3,000 rpm, 5,000 rpm and 8,000 rpm) and four different distances between the dual CFFs (26 mm, 52 mm, 78 mm and 104 mm). Thereafter, an experiment was conducted to compare and validate the results of the simulation.				
14. SUBJECT TERMS Vertical Take-Off, VTOL, Cross-Flow Fan, CFF, Thrust Augmentation			15. NUMBER OF PAGES 137	
			16. PRICE CODE	
17. SECURITY CLASSIFICATION OF REPORT Unclassified	18. SECURITY CLASSIFICATION OF THIS PAGE Unclassified	19. SECURITY CLASSIFICATION OF ABSTRACT Unclassified	20. LIMITATION OF ABSTRACT UU	

THIS PAGE INTENTIONALLY LEFT BLANK

Approved for public release; distribution is unlimited

**THRUST AUGMENTATION STUDY OF CROSS-FLOW FAN FOR VERTICAL
TAKE-OFF AND LANDING AIRCRAFT**

Ing Khang Yeo
Singapore Technologies Kinetics Limited, Singapore
B.S.M.E, Nanyang Technological University of Singapore (NTU), 2004

Submitted in partial fulfillment of the
requirements for the degree of

MASTER OF SCIENCE IN MECHANICAL ENGINEERING

from the

**NAVAL POSTGRADUATE SCHOOL
September 2012**

Author: Ing Khang Yeo

Approved by: Garth V. Hobson
Thesis Advisor

Anthony J. Gannon
Second Reader

Knox T. Millsaps
Chair, Department of Mechanical and Aerospace Engineering

THIS PAGE INTENTIONALLY LEFT BLANK

ABSTRACT

Vertical Take-Off and Landing (VTOL) has primarily seen research and development in the two traditional fields, namely the rotary wing and jet propulsion, with each seeking incremental improvements in thrust generation and fuel efficiency, respectively. In recent years, there has been increasing interest in the viability of the Cross-Flow Fans (CFF) being the primary source of aircraft propulsion. There has been measured success in horizontal flight; however, VTOL propulsion with CFFs remains elusive.

The current study seeks to determine the feasibility of combining two CFFs in a back-to-back configuration that could augment the thrust generated, thus making VTOL a reality. Making use of an optimized CFF housing, the research aimed to maximize the thrust generated in the above mentioned configuration by varying the gap between the CFFs. Computational fluid simulations of the dual CFF configuration was performed using ANSYS CFX to find the thrust generated as well as the optimal operating point. Analysis was done at three different speeds (3,000 rpm, 5,000 rpm and 8,000 rpm) and four different distances between the dual CFFs (26 mm, 52 mm, 78 mm and 104 mm). Thereafter, an experiment was conducted to compare and validate the results of the simulation.

THIS PAGE INTENTIONALLY LEFT BLANK

TABLE OF CONTENTS

I.	INTRODUCTION.....	1
A.	OVERVIEW.....	1
B.	BACKGROUND	1
C.	OBJECTIVE	5
II.	DESCRIPTION OF THE ANALYTICAL MODEL.....	7
A.	OVERVIEW.....	7
B.	SOLID MODELING	7
C.	MESH GENERATION AND BOUNDARY CONDITIONS.....	10
1.	Mesh Generation.....	10
2.	Established Boundary Conditions and Analysis	13
D.	SIMULATION PLAN	17
III.	EXPERIMENTAL SETUP.....	19
A.	PRE-EXPERIMENT CONFIRMATION TEST	19
B.	DRAGONPLATE CFF TEST SETUP.....	20
IV.	RESULTS AND DISCUSSION	23
A.	ANALYTICAL MODEL/SIMULATION	23
B.	EXPERIMENTAL MEASUREMENTS.....	28
C.	ANALYTICAL VERSUS EXPERIMENTAL RESULTS.....	34
D.	LARGER EXHAUST-GROUND DISTANCE EXPERIMENTAL RESULT.....	38
E.	OVERALL SIMULATION/EXPERIMENT DISCUSSION.....	42
V.	CONCLUSION AND RECOMMENDATIONS.....	43
A.	CONCLUSION	43
B.	RECOMMENDATIONS.....	43
	APPENDIX A. ANSYS CFX SETTINGS FOR DUAL CFF (8,000 RPM)	45
	APPENDIX B. SOFASCO CFF EXPERIMENT	51
A.	PRELIMINARY TEST	51
B.	RESULTS ANALYSIS.....	57
	APPENDIX C. SINGLE CFF EXPERIMENT REPEATABILITY TEST & VALIDATION.....	61
A.	PURPOSE OF VALIDATION	61
B.	EQUIPMENT LIST.....	61
C.	EXPERIMENTAL SETUP.....	62
D.	PROCEDURE	62
1.	Battery Charging	62
2.	Programming of Controller	64
3.	CFF Test Operation.....	68
E.	RESULTS OF VALIDATION.....	71
	APPENDIX D. DRAGONPLATE CFF EXPERIMENT PROCEDURE.....	73

A.	PURPOSE OF EXPERIMENTAL PROCEDURE	73
B.	EQUIPMENT LIST.....	73
C.	EXPERIMENTAL SETUP	74
D.	PROCEDURE	74
1.	Battery Charging	74
2.	CFF Test Operation.....	76
APPENDIX E.	DRAGONPLATE CFF SIMULATION RESULTS	81
A.	TORQUE MONITOR AND THRUST PLOTS	81
B.	VELOCITY CONTOUR, STREAMLINE AND VECTOR PLOTS	82
C.	THRUST RESULTS.....	105
APPENDIX F.	DRAGONPLATE CFF EXPERIMENTAL RESULTS.....	107
APPENDIX G.	LARGER EXHAUST-GROUND DISTANCE	
	DRAGONPLATE CFF EXPERIMENTAL RESULTS.....	111
	LIST OF REFERENCES	115
	INITIAL DISTRIBUTION LIST	117

LIST OF FIGURES

Figure 1.	Schematic of a CFF.....	2
Figure 2.	An example of a commercial CFF used for cooling	2
Figure 3.	First working prototype of a CFF-propelled air platform by Propulsive Wing, LLC	3
Figure 4.	Schematic of a Propulsive Wing.....	4
Figure 5.	Schematic of the streamline flowing past Propulsive Wing (Fan On/Off).....	4
Figure 6.	Physical CAD model of CFF & housing	8
Figure 7.	SOLIDWORKS model of 16-bladed DragonPlate CFF rotor flow field	9
Figure 8.	SOLIDWORKS model of CFF housing and surrounding air domain	10
Figure 9.	Mesh quality generated in rotor and stator with single element thickness	12
Figure 10.	Details of mesh with “Sweep” method applied	13
Figure 11.	Dual CFF configuration	14
Figure 12.	Locations of CFF boundaries.....	16
Figure 13.	Dual CFF configuration experimental setup.....	19
Figure 14.	Close-up view of rheostat speed controller.....	20
Figure 15.	Adjustment of dual CFF gap size.....	21
Figure 16.	Plot of torque versus no. of revolutions at 3,000 rpm.....	23
Figure 17.	Plot of thrust versus no. of revolutions at 3,000 rpm.....	24
Figure 18.	Plot of torque versus no. of revolutions at 8,000 rpm.....	25
Figure 19.	Plot of thrust versus no. of revolutions at 8,000 rpm.....	25
Figure 20.	Plot of simulation thrust versus rotational speed	26
Figure 21.	Plot of simulation thrust versus gap size.....	27
Figure 22.	Plot of simulation percentage increase in thrust versus gap size	28
Figure 23.	Upward flow through the gap between the two CFFs	29
Figure 24.	Schematic of splitting of flow in a single CFF configuration.....	30
Figure 25.	Schematic of splitting and re-ingestion of flow in a dual CFF configuration	31
Figure 26.	Plot of experimental thrust versus rotational speed	31
Figure 27.	Plot of experimental thrust versus gap size at different rotational speeds	32
Figure 28.	Plot of experimental percentage change in thrust versus gap size.....	33
Figure 29.	Plot of experimental average percentage change in thrust versus gap size	34
Figure 30.	Plot of torque (wall B.C.) versus no. of revolutions at 5,000 rpm.....	35
Figure 31.	Plot of thrust (wall B.C.) versus no. of revolutions at 5,000 rpm.....	36
Figure 32.	CFX simulation for a single CFF configuration when a “wall” boundary condition is applied at the bottom plane	36
Figure 33.	CFX simulation for a dual CFF configuration when a “wall” boundary condition is applied at the bottom plane	37
Figure 34.	Plot of larger exhaust-ground distance experimental thrust versus rotational speed	39
Figure 35.	Plot of larger exhaust-ground distance experimental thrust versus gap size at different rotational speeds.....	40

Figure 36.	Plot of larger exhaust-ground distance experimental percentage change in thrust versus gap size	40
Figure 37.	Plot of average percentage change in thrust versus gap size (comparison)	41
Figure 38.	SOFASCO CFF rotor (ruler large divisions in inches).....	51
Figure 39.	SOFASCO dual CFF configuration	52
Figure 40.	Side view of SOFASCO dual CFF configuration.....	52
Figure 41.	SOFASCO dual CFF configuration experimental setup.....	53
Figure 42.	Graph of % thrust increase versus gap size	58
Figure 43.	Graph of average % increase in thrust versus gap size.....	59
Figure 44.	Overall experimental setup and major components.....	62
Figure 45.	TP1340C balancer and ALL STATE battery charger.....	62
Figure 46.	TP batteries and extension leads	63
Figure 47.	TP battery connection to balancer circuit board	63
Figure 48.	battery connected to balancer and charging.....	64
Figure 49.	battery and controller connection.....	65
Figure 50.	Laptop, cable link to controller and connection to connector.....	65
Figure 51.	Pulse generator and pulse width adjustment buttons	66
Figure 52.	Selection of waveform on pulse generator.....	66
Figure 53.	Location of “Scorpion ESC Programmer v1.2”	66
Figure 54.	Opened “Scorpion ESC Programmer v1.2” application.....	67
Figure 55.	Location of COM port selection	67
Figure 56.	Control setting for controller	68
Figure 57.	DC power supply	68
Figure 58.	Selection of waveform on pulse generator.....	69
Figure 59.	CFF in housing and white marking on blade	69
Figure 60.	Stroboscope.....	70
Figure 61.	Thermostat	70
Figure 62.	Overall DragonPlate CFF experimental setup and major components.....	74
Figure 63.	TP1340C balancer and ALL STATE battery charger.....	74
Figure 64.	TP batteries and extension leads	75
Figure 65.	TP battery connection to balancer circuit board	75
Figure 66.	battery connected to balancer and charging.....	76
Figure 67.	DC power supply	77
Figure 68.	Pre-setting rheostat before connecting battery.....	77
Figure 69.	battery and controller connection.....	78
Figure 70.	Adjustment of gap size between CFF 1 and CFF 2	78
Figure 71.	Stroboscope.....	79
Figure 72.	CFF in housing and white marking on blade	79
Figure 73.	Thermostat	80
Figure 74.	Plot of torque versus no. of revolutions at 5,000 rpm.....	81
Figure 75.	Plot of thrust versus no. of revolutions at 5,000 rpm.....	81
Figure 76.	Velocity contour for single CFF configuration at 3,000 rpm	82
Figure 77.	Velocity streamline for single CFF configuration at 3,000 rpm.....	82
Figure 78.	Velocity vector for single CFF configuration at 3,000 rpm.....	83
Figure 79.	Velocity contour for single CFF configuration at 5,000 rpm	83

Figure 80.	Velocity streamline for single CFF configuration at 5,000 rpm.....	84
Figure 81.	Velocity vector for single CFF configuration at 5,000 rpm.....	84
Figure 82.	Velocity contour for single CFF configuration at 8,000 rpm	85
Figure 83.	Velocity streamline for single CFF configuration at 8,000 rpm.....	85
Figure 84.	Velocity vector for single CFF configuration at 8,000 rpm.....	86
Figure 85.	Velocity contour for 26 mm gap CFF configuration at 3,000 rpm.....	86
Figure 86.	Velocity streamline for 26 mm gap CFF configuration at 3,000 rpm	87
Figure 87.	Velocity vector for 26 mm gap CFF configuration at 3,000 rpm	87
Figure 88.	Velocity contour for 26 mm gap CFF configuration at 5,000 rpm.....	88
Figure 89.	Velocity streamline for 26 mm gap CFF configuration at 5,000 rpm	88
Figure 90.	Velocity vector for 26 mm gap CFF configuration at 5,000 rpm	89
Figure 91.	Velocity contour for 26 mm gap CFF configuration at 8,000 rpm.....	89
Figure 92.	Velocity streamline for 26 mm gap CFF configuration at 8,000 rpm	90
Figure 93.	Velocity vector for 26 mm gap CFF configuration at 8,000 rpm	90
Figure 94.	Velocity contour for 52 mm gap CFF configuration at 3,000 rpm.....	91
Figure 95.	Velocity streamline for 52 mm gap CFF configuration at 3,000 rpm	91
Figure 96.	Velocity vector for 52 mm gap CFF configuration at 3,000 rpm	92
Figure 97.	Velocity contour for 52 mm gap CFF configuration at 5,000 rpm.....	92
Figure 98.	Velocity streamline for 52 mm gap CFF configuration at 5,000 rpm	93
Figure 99.	Velocity vector for 52 mm gap CFF configuration at 5,000 rpm	93
Figure 100.	Velocity contour for 52 mm gap CFF configuration at 8,000 rpm.....	94
Figure 101.	Velocity streamline for 52 mm gap CFF configuration at 8,000 rpm	94
Figure 102.	Velocity vector for 52 mm gap CFF configuration at 8,000 rpm	95
Figure 103.	Velocity contour for 78 mm gap CFF configuration at 3,000 rpm.....	95
Figure 104.	Velocity streamline for 78 mm gap CFF configuration at 3,000 rpm	96
Figure 105.	Velocity vector for 78 mm gap CFF configuration at 3,000 rpm	96
Figure 106.	Velocity contour for 78 mm gap CFF configuration at 5,000 rpm.....	97
Figure 107.	Velocity streamline for 78 mm gap CFF configuration at 5,000 rpm	97
Figure 108.	Velocity vector for 78 mm gap CFF configuration at 5,000 rpm	98
Figure 109.	Velocity contour for 78 mm gap CFF configuration at 8,000 rpm.....	98
Figure 110.	Velocity streamline for 78 mm gap CFF configuration at 8,000 rpm	99
Figure 111.	Velocity vector for 78 mm gap CFF configuration at 8,000 rpm	99
Figure 112.	Velocity contour for 104 mm gap CFF configuration at 3,000 rpm.....	100
Figure 113.	Velocity streamline for 104 mm gap CFF configuration at 3,000 rpm	100
Figure 114.	Velocity vector for 104 mm gap CFF configuration at 3,000 rpm	101
Figure 115.	Velocity contour for 104 mm gap CFF configuration at 5,000 rpm.....	101
Figure 116.	Velocity streamline for 104 mm gap CFF configuration at 5,000 rpm	102
Figure 117.	Velocity vector for 104 mm gap CFF configuration at 5,000 rpm	102
Figure 118.	Velocity contour for 104 mm gap CFF configuration at 8,000 rpm.....	103
Figure 119.	Velocity streamline for 104 mm gap CFF configuration at 8,000 rpm	103
Figure 120.	Velocity vector for 104 mm gap CFF configuration at 8,000 rpm	104

THIS PAGE INTENTIONALLY LEFT BLANK

LIST OF TABLES

Table 1.	CFF assembly mesh statistics	12
Table 2.	Changes in value settings for each rotational speed	17
Table 3.	List of nominal rotational speeds for dual CFF configuration experiment.....	22
Table 4.	Experimental data for single CFF	54
Table 5.	Experimental data for dual CFF with 7 mm	54
Table 6.	Experimental data for dual CFF with 9 mm	55
Table 7.	Experimental data for dual CFF with 11 mm	55
Table 8.	Experimental data for dual CFF with 14 mm	56
Table 9.	Experimental data for dual CFF with 18 mm	56
Table 10.	Experimental data for dual CFF with 25 mm	57
Table 11.	Consolidated table of % thrust increase at different gap sizes and speeds	57
Table 12.	Thrust measurement comparison with Delagrange's records	71
Table 13.	Single DragonPlate CFF configuration simulation thrust results	105
Table 14.	26 mm gap DragonPlate CFF configuration simulation thrust results	105
Table 15.	52 mm gap DragonPlate CFF configuration simulation thrust results	105
Table 16.	78 mm gap DragonPlate CFF configuration simulation thrust results	105
Table 17.	104 mm gap DragonPlate CFF configuration simulation thrust results	106
Table 18.	Single DragonPlate CFF configuration experimental thrust results	107
Table 19.	26 mm gap DragonPlate CFF configuration experimental thrust results	107
Table 20.	52 mm gap DragonPlate CFF configuration experimental thrust results	107
Table 21.	78 mm gap DragonPlate CFF configuration experimental thrust results	108
Table 22.	104 mm gap DragonPlate CFF configuration experimental thrust results	108
Table 23.	Thrust at various gap sizes for different rotational speeds	108
Table 24.	Percentage thrust increase at various gap sizes for different rotational speeds	109
Table 25.	Average percentage change in thrust at various gap sizes	109
Table 26.	Single DragonPlate CFF configuration experimental thrust results (larger exhaust-ground distance)	111
Table 27.	18 mm gap DragonPlate CFF configuration experimental thrust results (larger exhaust-ground distance).....	111
Table 28.	26 mm gap DragonPlate CFF configuration experimental thrust results (larger exhaust-ground distance).....	111
Table 29.	52 mm gap DragonPlate CFF configuration experimental thrust results (larger exhaust-ground distance).....	112
Table 30.	78 mm gap DragonPlate CFF configuration experimental thrust results (larger exhaust-ground distance).....	112
Table 31.	104 mm gap DragonPlate CFF configuration experimental thrust results (larger exhaust-ground distance).....	112
Table 32.	Thrust at various gap sizes for different rotational speeds (larger exhaust-ground distance).....	113
Table 33.	Percentage thrust increase at various gap sizes for different rotational speeds (larger exhaust-ground distance).....	113

Table 34.	Average percentage change in thrust at various gap sizes (larger exhaust-ground distance).....	113
-----------	--	-----

LIST OF ACRONYMS AND ABBREVIATIONS

2D	Two-Dimensional
A	Area
a_i	Elemental area
CFX-Pre	Part of the ANSYS-CFX package for application of boundary and initial conditions as well as solver settings
CFX-Post	Part of the ANSYS-CFX package for analyzing numerical solutions.
CFX-Solver	Part of the ANSYS-CFX package for numerical computation of fluid model.
CFD	Computational fluid dynamics
CFF	Cross-Flow Fan
δ	Nondimensional total pressure correction term
DC	Direct current
ε	Viscous dissipation
g	gram
h	Enthalpy
HVAC	Heating ventilation and cooling
I	Current
k	Turbulent kinetic energy
K	Degree Kelvin
kg	Kilogram
λ	Thermal conductivity
LiPo	Lithium polymer
LTV	Ling-Temco-Vought

μ	Dynamic viscosity
μ_t	Turbulent viscosity
m	meter
mm	millimeter
N	Newton
p	Pressure
p_o	Total Pressure
Pa	Pascal
ρ	Density
rpm	Revolutions per minute
s	second
S_E	Energy source equation
S_M	Momentum source equation
SOLIDWORKS	Three-dimensional drafting and solid modeling software package
T	Temperature
T_t	Total temperature
TPL	Turbopropulsion laboratory
U	Velocity
V	Voltage
VSD	Vought Systems Division
VTOL	Vertical Take-Off and Landing
WORKBENCH	ANSYS simulation package which ties external CAD software together with the ANSYS suite finite element software

ACKNOWLEDGMENTS

I would like to express my gratitude and appreciation to the following people:

Professor Garth Hobson, for his encouragement, never-ending optimism and genuine excitement about the thesis research I conducted.

Professor Anthony Gannon, for allowing me to tap into his seemingly endless knowledge of CFD analysis, and assisting me with any questions I could devise for him.

Chris Clay, for his assistance and patience in helping me with every aspect of my CFF experimental setup and experimentation.

Finally, with a tremendous amount of love, I thank my fiancé, Shaminta, for her support, encouragement and understanding.

THIS PAGE INTENTIONALLY LEFT BLANK

I. INTRODUCTION

A. OVERVIEW

The ability of aircraft to take off and land vertically has always been of great interest, especially to the military. With the changing combat landscape, this capability is even more crucial where time and space is a luxury. While Vertical Take-Off and Landing (VTOL) has been around since 1950 with the use of rotary wings and jet engines, there has yet to be a propulsion system that is efficient like the former and one which is compact and capable of extremely high thrust like the latter [1]. Furthermore, large and cumbersome rotary wings are a safety concern with their exposed blades. Embedding Cross-Flow Fans (CFF) into fixed-wing aircrafts provides a viable solution to the shortcomings of the currently used VTOL methods. It could possibly provide a safe, efficient propulsion system with high thrust capability necessary for aircraft operations. With the escalating fuel prices, this VTOL alternative makes for a tantalizing solution in a time when cost minimization in the military is paramount.

B. BACKGROUND

Early research of the CFF, also known as the Tangential Fan, was not carried out by established research groups but rather by individuals. It is because of this that there is very little official documentation on its early development even though it was initially patented by Mortier in 1893 [2].

The CFF has a high span-to-diameter ratio, effectively making it a two-dimensional flow away from the ends of the CFF [3]. It consists of a multiple curve blade rotor (an impeller) that is encased in a housing as shown in Figure 1. The air flow passes across the impeller, passing the blades twice before exiting from the housing outlet [2]. The CFF is used extensively in the Heating, Ventilation and Air Conditioning (HVAC) industries. For many years, the CFF's sole function was to act as a cooling system. Its popularity stemmed from its compact shape, low acoustic output and cooling effectiveness [3]. A typical commercial CFF used to cool the interior of a computer server can be seen in Figure 2.

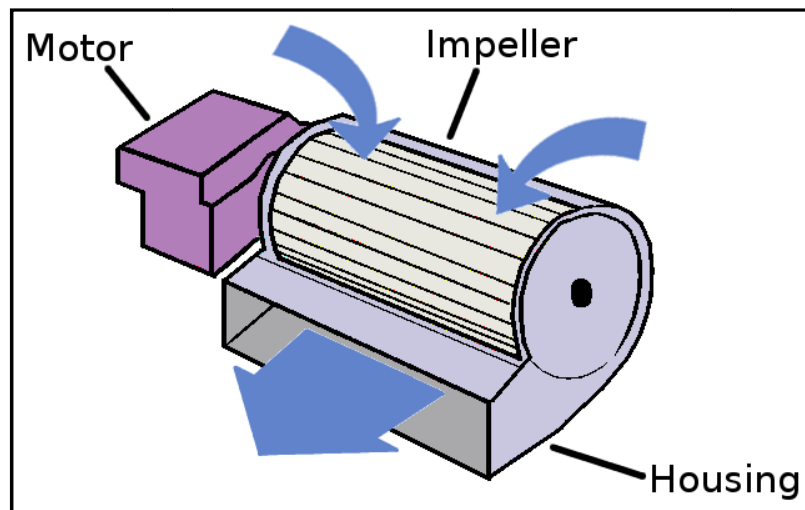


Figure 1. Schematic of a CFF



Figure 2. An example of a commercial CFF used for cooling

The thought of using the CFF as a form of aircraft propulsion came as early as the 1970s. Vought Systems Division (VSD) of the Ling-Temco-Vought (LTV) Aerospace Corporation was awarded the contract by the U.S. Navy to research the possibility of generating sufficient thrust in the CFF for aircraft propulsion [4]. While the research showed that the CFF was capable of producing thrust necessary for aircraft propulsion, the interest in CFF propulsion dwindled and there was little or no further progress until the turn of the century.

The next group of researchers interested in this topic came from the Turbo Propulsion Laboratory (TPL) of the Naval Postgraduate School (NPS). In 2000, D. H.

Gossett suggested utilizing the CFF as a means of thrust augmentation for a light-weight single seat aircraft to perform VTOL [4]. Many studies followed at the NPS's TPL where research was done to optimize the design of the CFF through simulation and/or experiments in order to improve performance for flight such as the optimal number of blades [5]. The latest study was conducted in June 2012 by Delagrange where he utilized the fluid computational software, ANSYS-CFX, to develop and design a CFF housing that would optimize the flow and maximize the thrust generated [6] from a CFF rotor obtained from Propulsive Wing.



Figure 3. First working prototype of a CFF-propelled air platform by Propulsive Wing, LLC

2006 saw the very first prototype of an air platform to be fully propelled by the CFF (Figure 3). The unmanned air platform was designed to have thick wings embedded with CFFs of lengths equal to the span of the wings. While not being able to perform VTOL, it was able to successfully take flight vertically. This air platform design was patented in 2006 by its developers, Propulsive Wing, LLC [7]. The schematic in Figure 4 shows the cross section of the Propulsive Wing design.

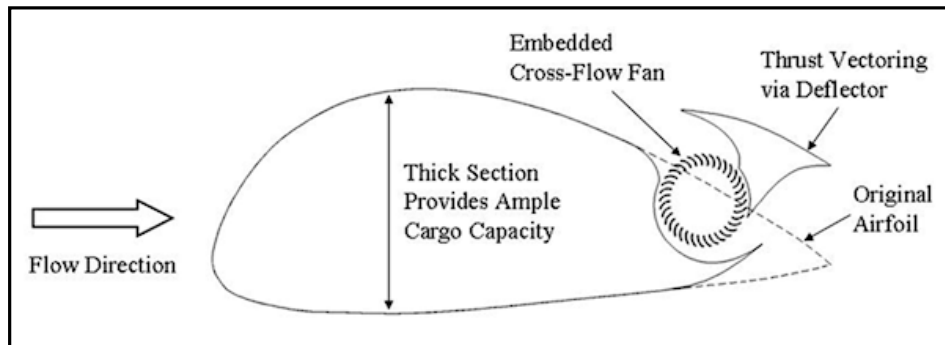


Figure 4. Schematic of a Propulsive Wing

Based on Propulsive Wing, LLC's research, it has been found that the design has many advantages as compared to conventional airfoil wings. It is capable of maintaining smooth fluid flow, increased lift and reduced drag as well as avoiding stall [7]. With the blades being encased, it makes operation safer as compared to traditional rotary wings. When flying at increasing angles of attack, conventional wings experience separation of streamlines, leading to a large wake at the back as can be similarly observed in the left schematic in Figure 5 [7]. This increases drag and decreases lift. When a critical angle of attack is reached, the wing will stall. However, when the CFF is turned on, the streamlines are pulled towards the body of the wing, thus re-attaching the flow, resulting in reduced drag. In fact, the Propulsive Wing is able to operate at an angle of attack of up to 45° [7]. Such flight characteristics show great potential in CFFs performing VTOL with further research.

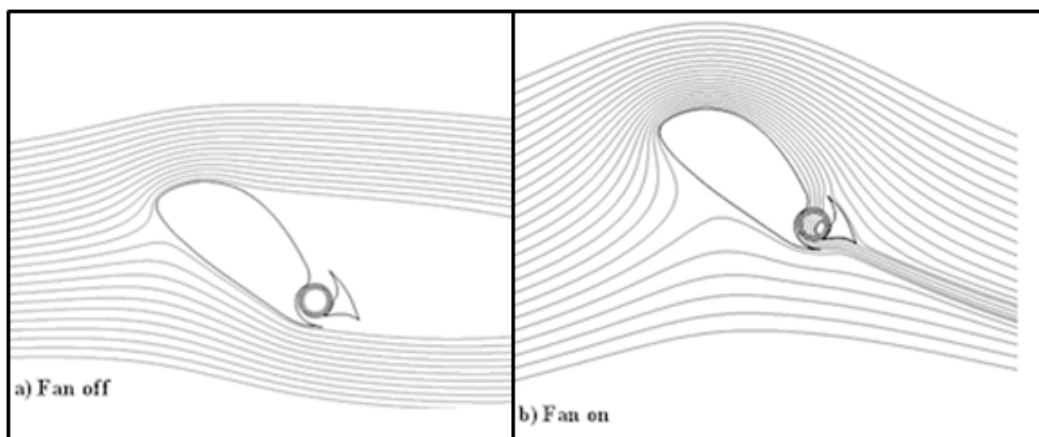


Figure 5. Schematic of the streamline flowing past Propulsive Wing (Fan On/Off)

Propulsive Wing's success has further fuelled interest in aircraft propulsion using CFFs for VTOL as can be seen from the collaboration between NPS and Temasek Defence Science Institute (TDSI) of Singapore in this area of research in 2012.

C. OBJECTIVE

The objective of this thesis is to investigate the thrust augmentation from placing two CFFs in a configuration across from each other. The distance between the two CFFs is varied along with the rotational speed to determine if there is an optimal spacing and whether the optimal spacing is a function of rotational speed. An analytical model will be used to obtain simulation results of the above in addition to conducting an experiment to validate these results.

THIS PAGE INTENTIONALLY LEFT BLANK

II. DESCRIPTION OF THE ANALYTICAL MODEL

A. OVERVIEW

A computational fluid dynamics (CFD) software created by ANSYS called CFX was used to analyze a two dimensional (2D) flow field of a CFF rotor and housing. The analysis used the geometry of a carbon fiber CFF purchased from DragonPlate Carbon Fiber Composites and the housing designed by Christopher T. Delagrange [6]. The difference between this analytical model and that of Delagrange's is that the former encompasses the flow field of the surrounding air outside the housing while the latter is only concerned with the flow field within the walls of the housing. An analysis was done to simulate the thrust generated by a single CFF and that of a CFF when it is positioned behind a second CFF in a mirror image configuration. This is referred to in this thesis as the "Dual CFF Configuration." The analytical model is done at permutations of various rotational speeds and different gap sizes (i.e., distance apart between two CFFs). The percentage augmentation is calculated and the trend studied to determine whether there is an optimal gap size at which maximum thrust is generated.

B. SOLID MODELING

The DragonPlate CFF has a diameter of 78 mm and a span of 210 mm with 16 circular arc blades. It has a supporting disc in the middle of the span. The housing was designed by Delagrange [6]. The 3D CAD model of the physical CFF and housing is shown in Figure 6. SOLIDWORKS, a commercial 3D computer-assisted drafting (CAD) software was used to model the CFF as a rotor flow field and the housing and surrounding air as a separate domain named "stator." Both models were extruded to a depth of 1 mm to simulate a thin slice of the CFF and housing for a 2D analysis. A 3D model would take significantly more computational time than a 2D model. This is due to the fact that a 2D model drastically reduces the mesh size. While a 3D simulation captures more real world effects, a 2D simulation is more suited to the initial design phase.

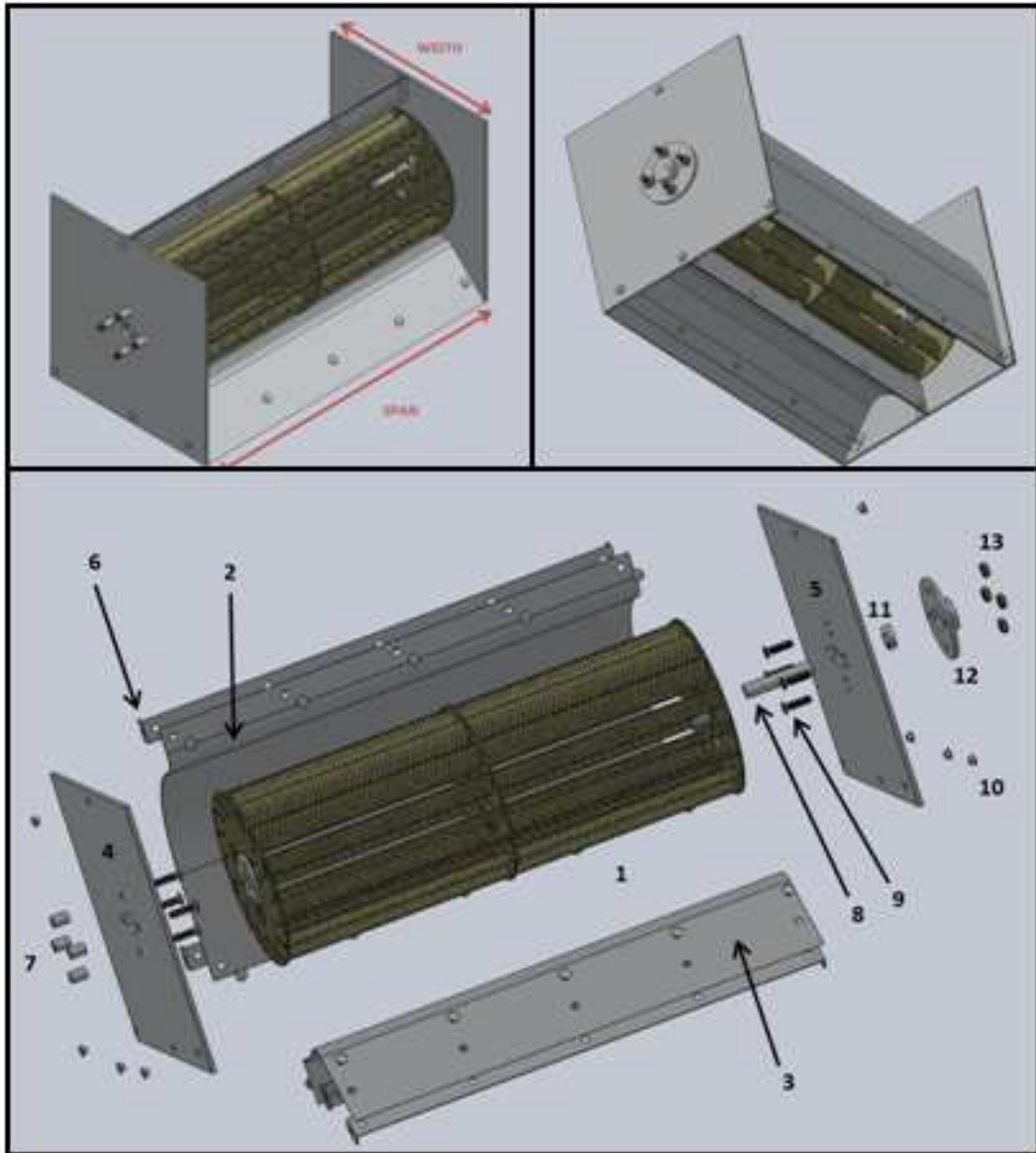


Figure 6. Physical CAD model of CFF & housing

The rotor domain was created by generating a 78 mm diameter solid disc of depth 1 mm. This solid disc is then used as the fluid volume in ANSYS-CFX. The 16 blades were then cut out of the solid disc and the surfaces of the extruded cuts were defined as walls to simulate the blades. The rotor flow field is as shown in Figure 7. It has to be noted that the rotor model had to be created as a separate body from the stator to be able to set the rotor domain to rotate in ANSYS-CFX.

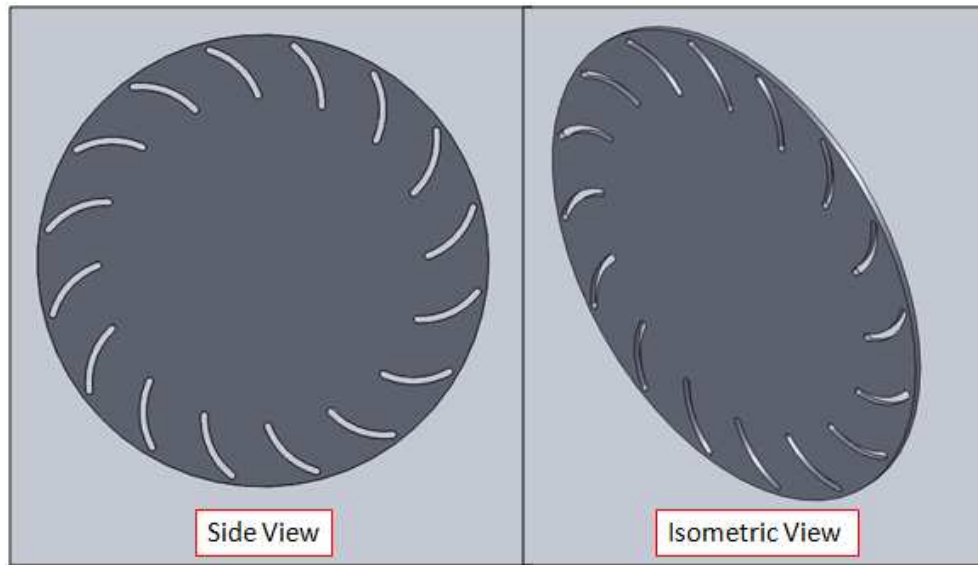


Figure 7. SOLIDWORKS model of 16-bladed DragonPlate CFF rotor flow field

The model for the stator was created by generating a solid rectangular domain of 1 mm thickness. A 78 mm diameter hole was cut out of the domain where the rotor was positioned. This was followed by the extruded cut of the housing cross-sectional profile around the hole. The surfaces of the housing extruded cuts were used to simulate the walls of the housing. Only one CFF and housing was required for simulation as the left face of the model was set as a symmetry plane, thus simulating the dual mode operation of the CFF's. This reduced the mesh size by half and consequently the computational time. As simulations for different gap sizes for the dual CFF configuration were required, a number of different stator models were required. Figure 8 shows the model of a stator flow field. The half-gap distance (as indicated in yellow in Figure 8) was varied based on the gap size of interest. For example, a 26 mm gap required a 13 mm half-gap distance. A total of four gap sizes of 26 mm, 52 mm, 78 mm and 104 mm were investigated.

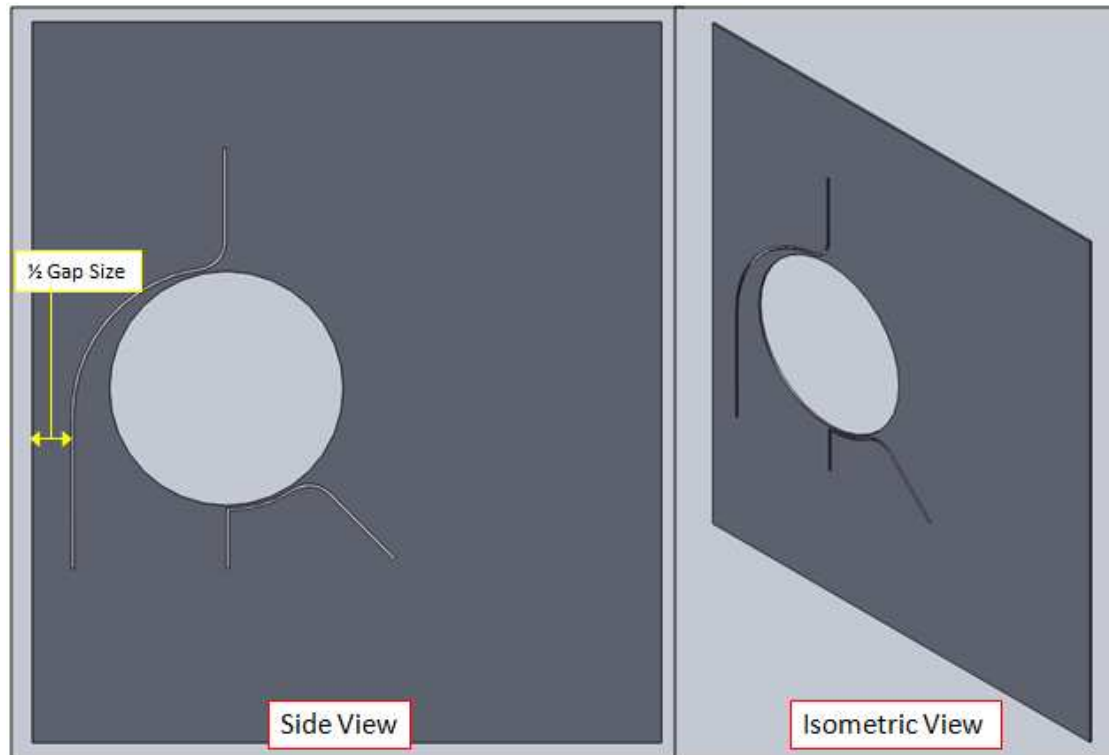


Figure 8. SOLIDWORKS model of CFF housing and surrounding air domain

For the case of the single CFF analysis for comparison, the same stator model was used by changing the boundary condition of the left face in ANSYS-CFX. This will be further described in the next Section. The SOLIDWORKS .SLDPRT (solid part) files were converted to .x_t (parasolid) files for subsequent transferal into ANSYS-CFX/WORKBENCH.

C. MESH GENERATION AND BOUNDARY CONDITIONS

1. Mesh Generation

ANSYS-WORKBENCH was used to insert the rotor and stator geometries as well as to generate the mesh. The simulation setups, numerical computation as well as the analysis of the results were all done using ANSYS-CFX. The rotor geometry was first imported into Design Modeler within ANSYS-WORKBENCH and generated as a fluid.

This was followed by the stator geometry. However, it was generated as a “frozen” material. This pre-setting allowed the rotor to be the rotating object while the stator became the stationary object.

Next in the work flow, the geometries were transferred to the mesher within WORKBENCH. In order to obtain good results, it is necessary to generate a sufficiently fine mesh. However, it has to be carefully balanced such that the mesh is not so fine to the extent that it takes up too much computational time to solve. Changing the coarseness of the mesh to “fine” did not generate enough elements (~10,000), especially around the housing/blade walls and rotor-stator interface. It resulted in the creation of mostly triangular elements which degraded the quality of the mesh. Mesh quality is an important consideration as it affects the control of discretization error when ANSYS-CFX does the numerical computation. There is, therefore, a need to transform most, if not all of the triangular elements into quadrilateral elements. This is described in the paragraph below.

“Edge” sizing was inserted at the blade profiles, housing profile as well as the rotor-stator interface (rotor and stator hole circumference). The reason for this setting was to increase the number of elements at or around these regions as the fluid interactions in these areas are of significant importance as compared to the rest of the fluid field. As seen from the stator model in Figure 8, there were some regions between the housing and the interface where the area is very thin. In order to try to obtain an all quadrilateral element model, a “Sweep” method was employed with a one division along the thickness (single element thickness). It was also necessary to have at least three elements across these thin areas. With these mesh settings done, the number of elements generated were significantly higher without having to set the mesh coarseness to “fine.”

The meshing was done through parallel processing on four to six processes each time in order to reduce the time required to compute the mesh. Each model took around four hours to complete. The mesh statistics for the four different models can be found in Table 1.

Table 1. CFF assembly mesh statistics

MODEL		NODES	ELEMENTS	% ELEMENTS
26 mm Gap	Rotor	110,066	53,887	10%
	Stator	1,030,786	512,786	90%
	Total	1,140,852	566,673	100%
52 mm Gap	Rotor	110,336	54,023	9%
	Stator	1,104,810	549,759	91%
	Total	1,215,146	603,782	100%
78 mm Gap	Rotor	111,530	54,604	9%
	Stator	1,169,224	582,552	91%
	Total	1,280,754	638,156	100%
104 mm Gap	Rotor	111,364	54,531	8%
	Stator	1,240,918	617,801	91%
	Total	1,352,282	672,332	100%

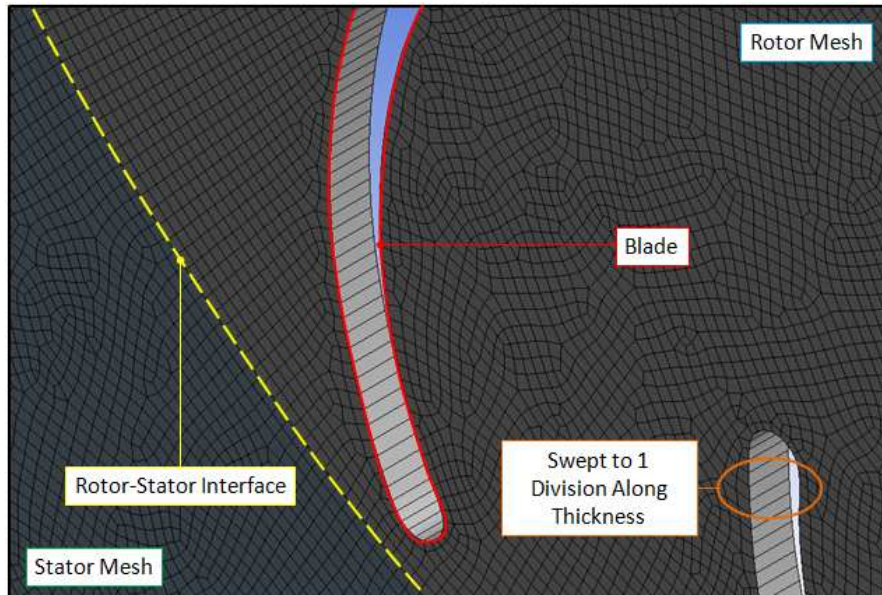


Figure 9. Mesh quality generated in rotor and stator with single element thickness

The effects of the mesh settings can be seen in Figure 9 and Figure 10 where the mesh quality is relatively good with a total of more than 600,000 elements. Figure 9 shows the single element thickness so that the model can be taken as a 2D analysis. Figure 10 shows the minimum three elements across gaps required for the numerical solution to be successful.

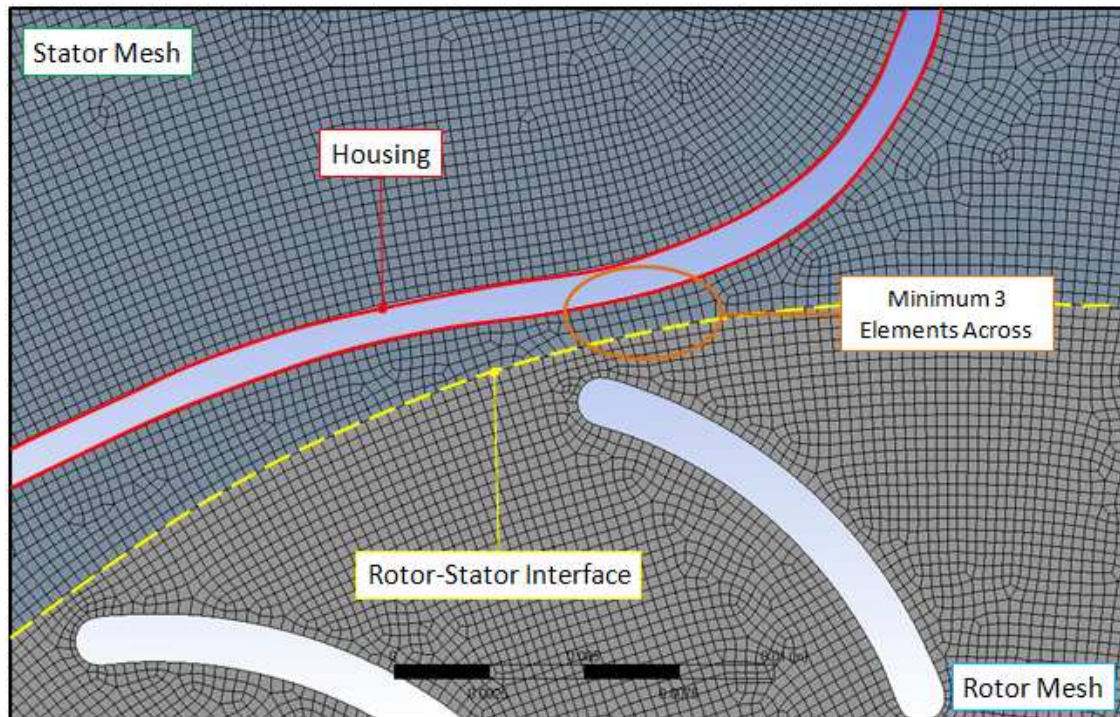


Figure 10. Details of mesh with “Sweep” method applied

2. Established Boundary Conditions and Analysis

As mentioned earlier, other than the import of geometry and meshing, ANSYS-CFX was used for the rest of the simulation tasks. The .CFX file created from the mesher in ANSYS-WORKBENCH was opened in ANSYS-CFX-Pre and the flow condition and boundary settings and a .DEF file was created for the numerical computation of the solution. Figure 11 shows how a dual CFF configuration should look like.

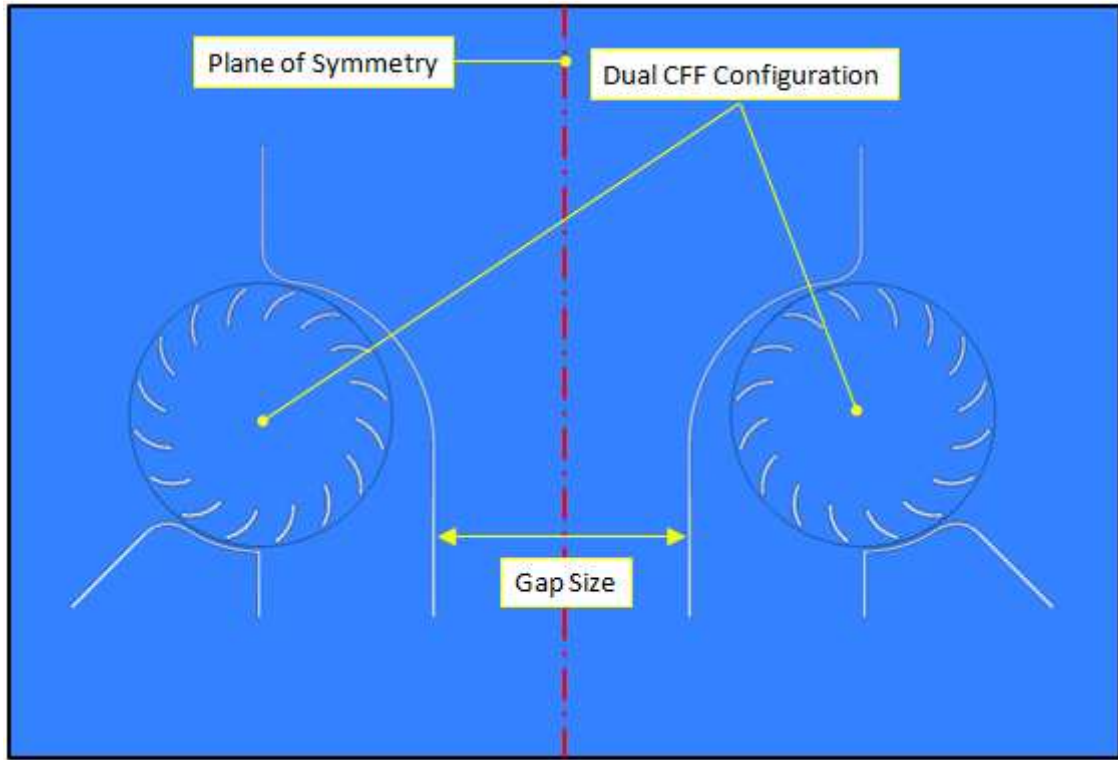


Figure 11. Dual CFF configuration

For the dual CFF CFD analysis, a transient analysis was done for a total of six revolutions of the rotor at which the torque on the rotor blades would have reached a relatively stable state [6]. The analysis was broken down into 2,160 time-steps based on one degree revolution per time step. A transient total energy simulation with k-epsilon turbulence model which included the viscous work term was used in the analysis. This dictated the equations used in the numerical computation of the solution. The equations used were as follows:

Continuity equation:

$$\frac{\partial \rho}{\partial t} + \nabla \cdot (\rho \mathbf{U}) = 0 \quad (1)$$

Momentum equation:

$$\frac{\partial \rho U}{\partial t} + \nabla \bullet (\rho U \otimes U) = \nabla \bullet \left(-p \delta + \mu \left(\nabla U + (\nabla U)^T \right) \right) \quad (2)$$

Energy equation:

$$\frac{\partial \rho h_{tot}}{\partial t} - \frac{\partial \rho}{\partial t} + \nabla \bullet (\rho U h_{tot}) = \nabla \bullet (\mu \nabla T) + \nabla \bullet \left(\mu \nabla U + \nabla U^T - \frac{2}{3} \nabla \bullet U \delta U \right) \quad (3)$$

$$h_{tot}(p, T) = h_{stat}(p, T) + \frac{1}{2} U^2 \quad (4)$$

Turbulent eddy viscosity:

$$\mu_t = C_\mu \rho \frac{\kappa^2}{\varepsilon} \quad (5)$$

Turbulent kinetic energy:

$$\frac{\partial (\rho k)}{\partial t} + \nabla \bullet (\rho U k) = \nabla \bullet \left[\left(\mu + \frac{\mu_t}{\sigma_\kappa} \right) \nabla k \right] + P_k - \rho \varepsilon \quad (6)$$

Turbulent eddy dissipation:

$$\frac{\partial (\rho \varepsilon)}{\partial t} + \nabla \bullet (\rho U \varepsilon) = \nabla \bullet \left[\left(\mu + \frac{\mu_t}{\sigma_\varepsilon} \right) \nabla \varepsilon \right] + \frac{\varepsilon}{\kappa} (C_{\varepsilon 1} P_\kappa - C_{\varepsilon 2} \rho \varepsilon) \quad (7)$$

The equation of state:

$$\rho(p, T) = \frac{p}{R_0 T} \quad (8)$$

The fluid used for both rotor and stator was air as an ideal gas at a relative pressure of 1atm and a temperature of 300K. The turbulence intensity factor was set to a default of 5%. The rotor was simulated at angular velocities of 3,000 rpm, 5,000 rpm and 8,000 rpm in the counter clockwise direction as shown in Figure 12. The stator was set as

a stationary fluid domain. Both the rotor and stator domains were set to have similar initial conditions where the velocities were zero. The interfaces between the rotor and stator were connected by applying the “Transient Rotor-Stator” setting in Frame Change/Model Mixing. This allowed communication between the rotor and stator domains.

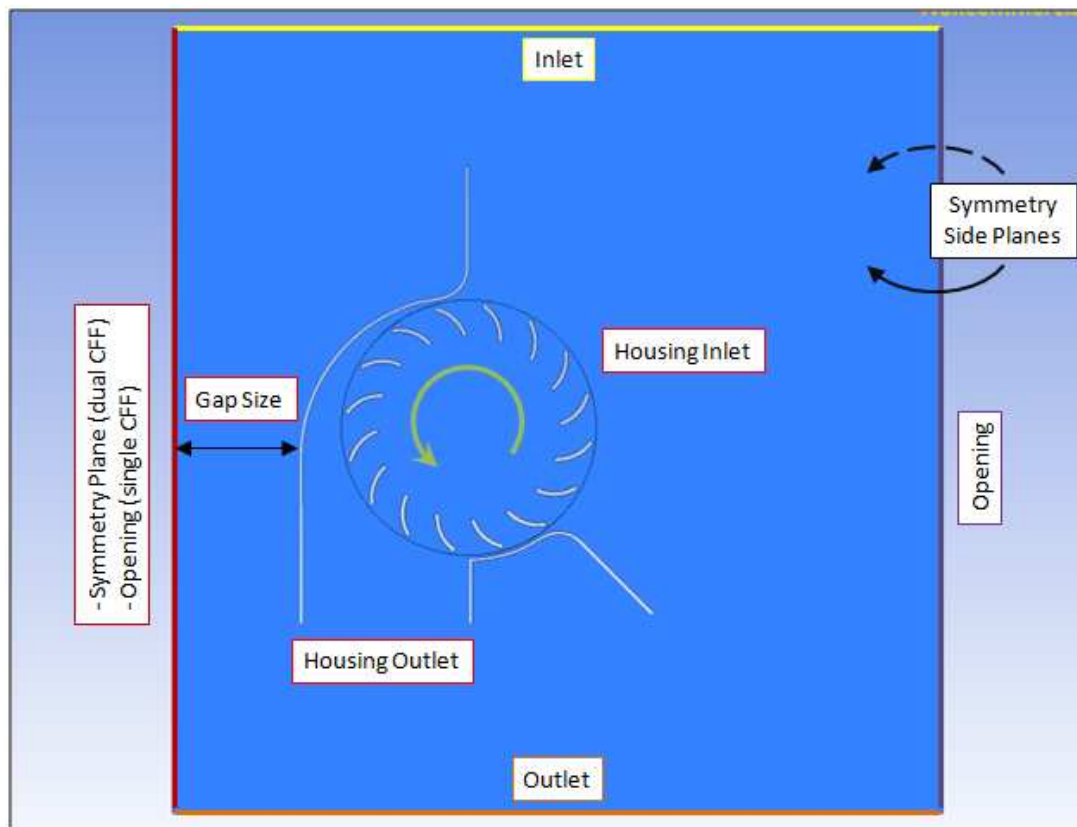


Figure 12. Locations of CFF boundaries

Using Figure 12 as reference, the side planes of the rotor-stator domain were set as “symmetry” boundaries. This was to simulate a thin 2D slice of the CFF span (away from the ends). The left plane, denoted by the red line, was set as a “symmetry” plane as well to simulate the dual CFF configuration as shown in Figure 11 but with less computation required. The top plane was given an “inlet” boundary condition and a vertically downward initializing velocity of 1m/s. This was to ensure that the air is coming into the top plane and entering down into the rotor instead of having an uncertainty in the flow direction as the rotor starts spinning. The right plane was given an

“opening” boundary condition with entrainment. This allowed the flow direction to be dictated by the other boundary conditions. Finally, an “outlet” boundary condition was set at the bottom plane. This was a necessary setting to ensure it is simulated that the air flow moved downwards. A plane would be added in CFX-POST to the bottom plane as if a wall were put in place and the force acting on this wall in the simulation would be the measured thrust from the CFF.

The detailed settings were set as documented in Appendix A for a dual CFF configuration rotating at 8,000 rpm. For the other rotational speeds of 3,000 rpm and 5,000 rpm, only the total time, time-step duration and rotor rotational speeds were changed for each individual scenario. The changes in values for each scenario are as shown in Table 2. In the case of the single CFF analysis, the only other difference was that the Left boundary condition was changed from a symmetry plane to an opening with entrainment.

Table 2. Changes in value settings for each rotational speed

Rotational Speed [RPM]	Total Time [s]	Time-Step Duration [s]
3,000	0.12	5.5556×10^{-5}
5,000	0.072	3.3333×10^{-5}
8,000	0.045	2.0833×10^{-5}

D. SIMULATION PLAN

In order to find the optimum gap size at which the thrust generated is at the maximum, at least three data points were required. Four gap sizes of 26 mm, 52 mm, 78 mm and 104 mm were chosen to be evaluated at rotor rotational speeds of 3,000 rpm, 5,000 rpm and 8,000 rpm. The single rotor model was also run at the same three speeds as a means of comparison with the dual CFF configurations. These simulations were run and the vertical force (y-axis) acting at the bottom was calculated using the function calculator in CFX-Post. The thrust and percentage thrust increase was calculated and the trend was plotted for each rotational speed. The plots were then studied to determine what the optimal gap size was and whether this optimal gap size differed for different speeds.

THIS PAGE INTENTIONALLY LEFT BLANK

III. EXPERIMENTAL SETUP

A. PRE-EXPERIMENT CONFIRMATION TEST

An initial pre-experiment was conducted on the 30 mm SOFASCO CFF (used for cooling in CPUs). This was done to ensure that the dual CFF configuration did indeed lead to thrust augmentation. The details of the experiment and results of the dual SOFASCO CFF setup can be found in Appendix B. Once thrust augmentation was confirmed for the configuration, a similar test setup was built for the DragonPlate CFFs used in Delagrange's research [6].

A repeatability test was also conducted for the CFF experiment (Delagrange's) to ensure that results could be reproduced. This is described in Appendix C. There were a few modifications to Delagrange's test setup as there were problems repeating the experiment due to loss of control of the programmed controller. The final configuration, which is similar to Delagrange's setup is as shown in Figure 13. The pulse width programmed controller to control the rotational speed of the CFF was replaced by a manually adjusted rheostat as shown in Figure 14 and a single ThunderPower LiPo battery was used instead of two in series for a CFF. The full setup description will be discussed in the next section.

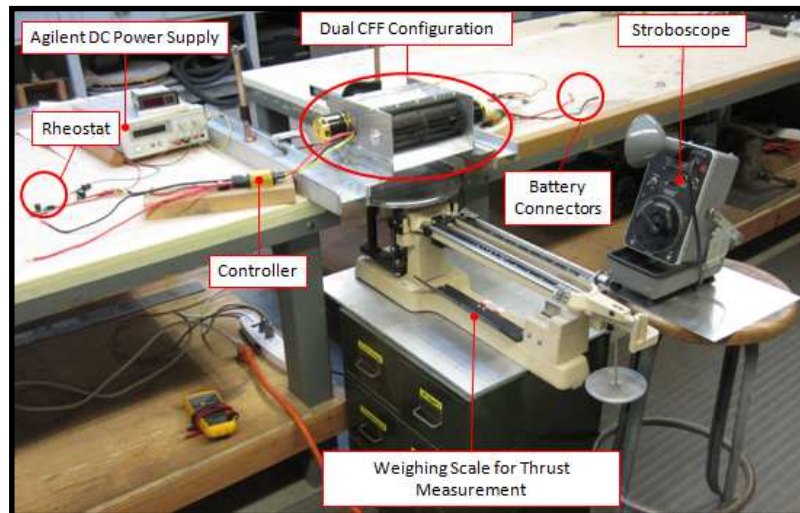


Figure 13. Dual CFF configuration experimental setup

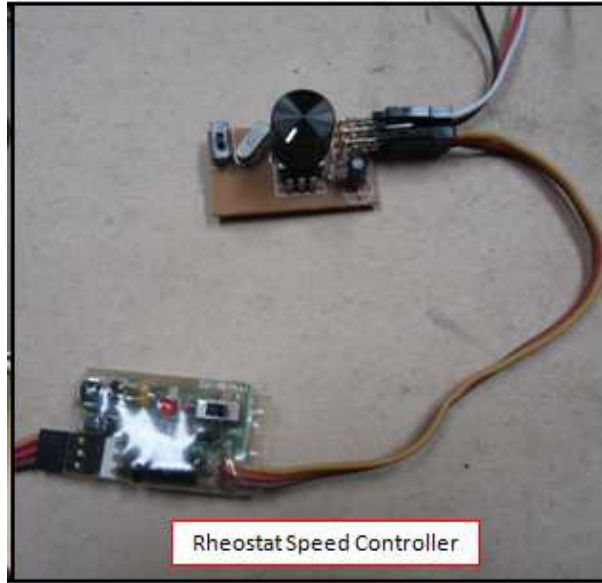


Figure 14. Close-up view of rheostat speed controller

B. DRAGONPLATE CFF TEST SETUP

Figure 13 shows the overall setup of the dual CFF configuration experiment. It consisted of two CFFs (CFF 1 and CFF 2) installed inside Delagrange's housing that were driven by a motor each. The motors were each connected separately to a controller that was in turn connected to a rheostat to control the rotational speed of the CFFs.

The controllers and rheostats were powered by the Agilent DC power supply. A battery was connected to each of the motors to power them up. It should be noted that in order to reach the maximum possible rotational speed of 9,150 rpm, there was a need to use two batteries that were connected in parallel for each motor. Other than that, the system was able to reach up to 8,000 rpm with just the use of a single battery per motor (refer to Appendix C).

A large experimental weighing scale was placed directly under the outlets of the CFFs for the flow to impinge on. A large plate weighing 355 g was placed on the scale and zeroed in order to capture the outlet air flow. This is due to the fact that the flow out does not impinge on the scale vertically downwards but at an angle instead when the two CFFs were operated together. This phenomenon will be further discussed in the next

chapter. White paint was painted on one of the 16 black blades for each CFF. This was required for determining the rotational speed of the CFFs.

A thermocouple was also used in the setup to constantly check on the temperature of the LiPo batteries, motors and controllers. Due to the high power density used in the test rig, the three components mentioned above could easily overheat. Temperature monitoring was essential to avoid overheating of the components that could lead to component failure or possibly start a fire.

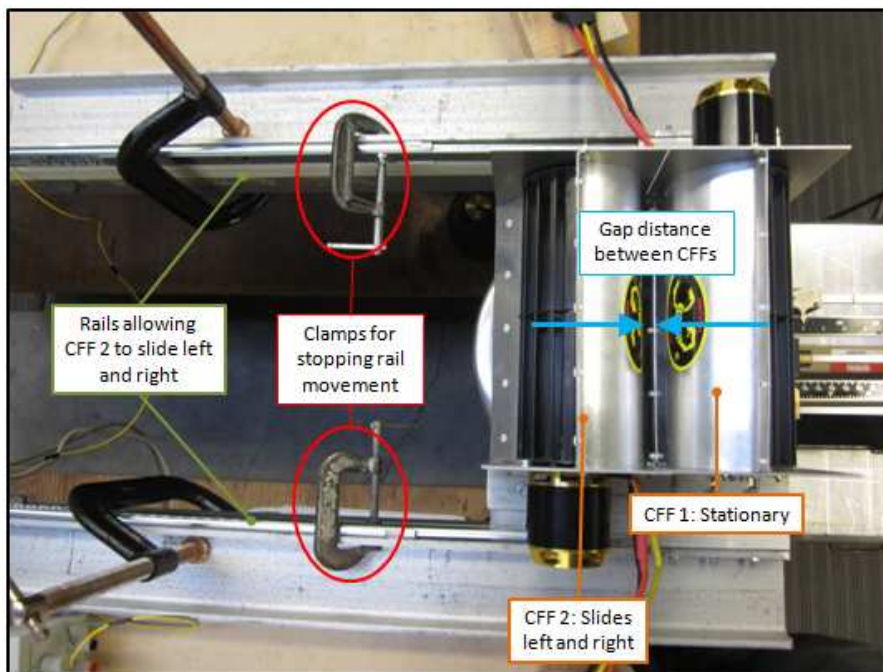


Figure 15. Adjustment of dual CFF gap size

CFF 1 was mounted between two beams and meant to be a stationary reference frame. Two sliding rails were bolted onto each of the two beams, parallel to each other. CFF 2 was mounted between the rails. This was to allow CFF 2 to slide towards and away from CFF 1. When CFF 1 and CFF 2 were both touching each other, the gap size was about 10 mm. Markers were placed on beam to indicate gap sizes of 26 mm, 52 mm, 78 mm and 104 mm. CFF 2 was moved along the beams to adjust the gap size. Once the adjustment was done, the sliding rails were clamped down on both sides to prevent

CFF 2 from accidentally shifting when the two CFFs were in operation. The sliding mechanism to adjust the gap size can be seen in Figure 16.

When the dual CFF configuration test rig was properly setup, CFF 2 was first activated and adjusted to the required rotational speed. This was done by placing the stroboscope in front of the rotating CFF 2 and setting the frequency of the flashing light to the required rotational speed, whilst adjusting the rheostat knob clockwise/counter-clockwise until the white paint on the blade of the CFF is perceived visually to be stationary or almost stationary. CFF 1 was then set to the same rotational speed as described above for CFF 2. The weights on the scale were then shifted until the scale was balanced. The force acting on the scale was recorded as the thrust generated by the CFF. This was repeated for the various rotational speeds and gap sizes.

In the case of the single CFF configuration, CFF 2 was moved away from CFF 1 with only CFF 1 connected to the battery. The rotational speeds and thrust measurements for each of the rotational speed and gap size permutations were done as described above for the dual CFF configuration (least with only one CFF). The thrust measured for CFF 1 was doubled to compare with the thrust measured for the dual CFF configuration.

A minimum of three rotational speeds per gap size were required as data points to plot out a trend. The rotational speeds used are as shown in Table 3:

Table 3. List of nominal rotational speeds for dual CFF configuration experiment

Rotational Speed [RPM]	For Comparison with Simulation Results
3,000	Yes
5,000	Yes
6,000	No
8,000	Yes
8,500	No

IV. RESULTS AND DISCUSSION

A. ANALYTICAL MODEL/SIMULATION

The torque on the CFF blades and the thrust generated from the CFF (outside the outlet) was monitored as it rotated for the six revolutions. This was to assess the type of flow that was occurring. Figures 16 and Figure 17 show the plots of torque versus number of revolutions and thrust versus number of revolutions when the CFF is run at a rotational speed of 3,000 rpm and at the single configuration, the 26 mm gap, 52 mm gap, 78 mm gap and 104 mm gap dual CFF configurations.

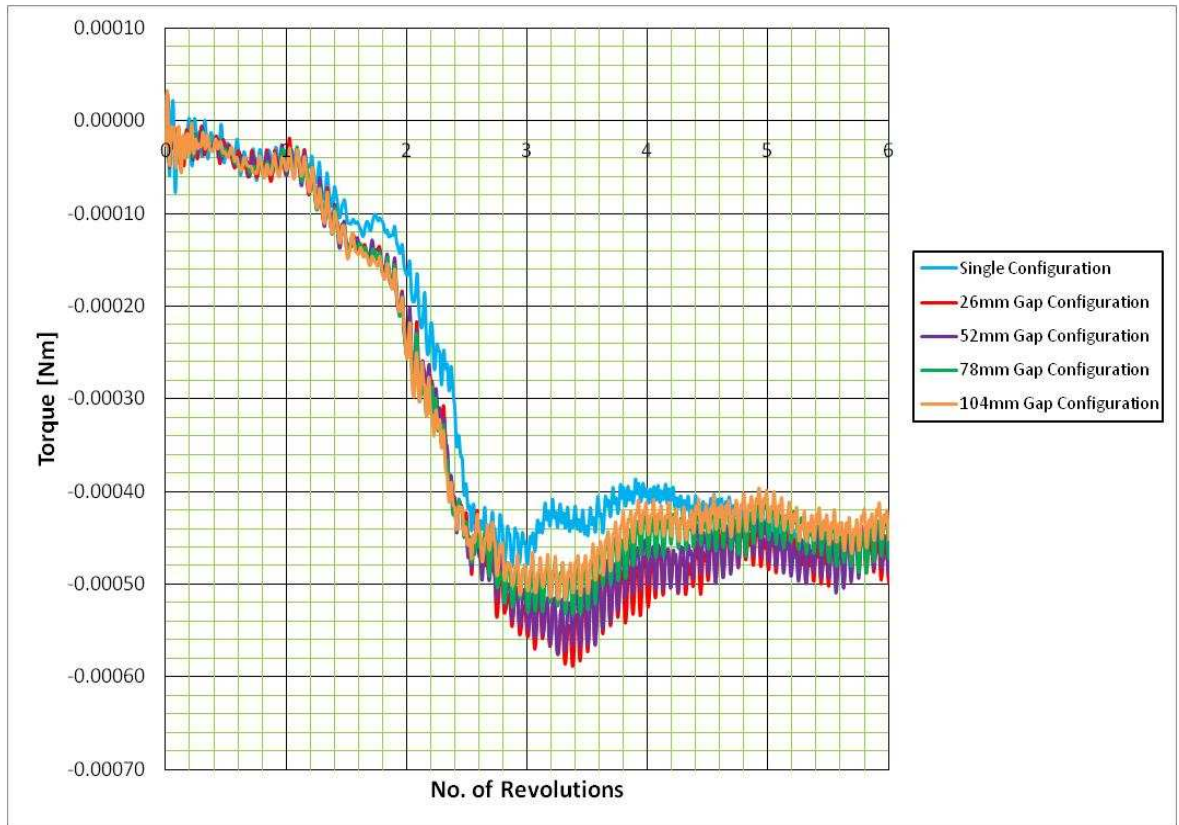


Figure 16. Plot of torque versus no. of revolutions at 3,000 rpm

It can be seen that after the initial start up from 0 to 4 revolutions, the torque on the blades of the CFF are seen to have a relatively constant trend. This shows that the

flow within the CFF is reasonably stable and that there is no stalling. This is similar to what was observed by Delagrange in his simulations [6]. The thrust plot also shows a relatively consistent level of thrust generated outside the CFF outlet. This also means that the flow is stable outside of the CFF.

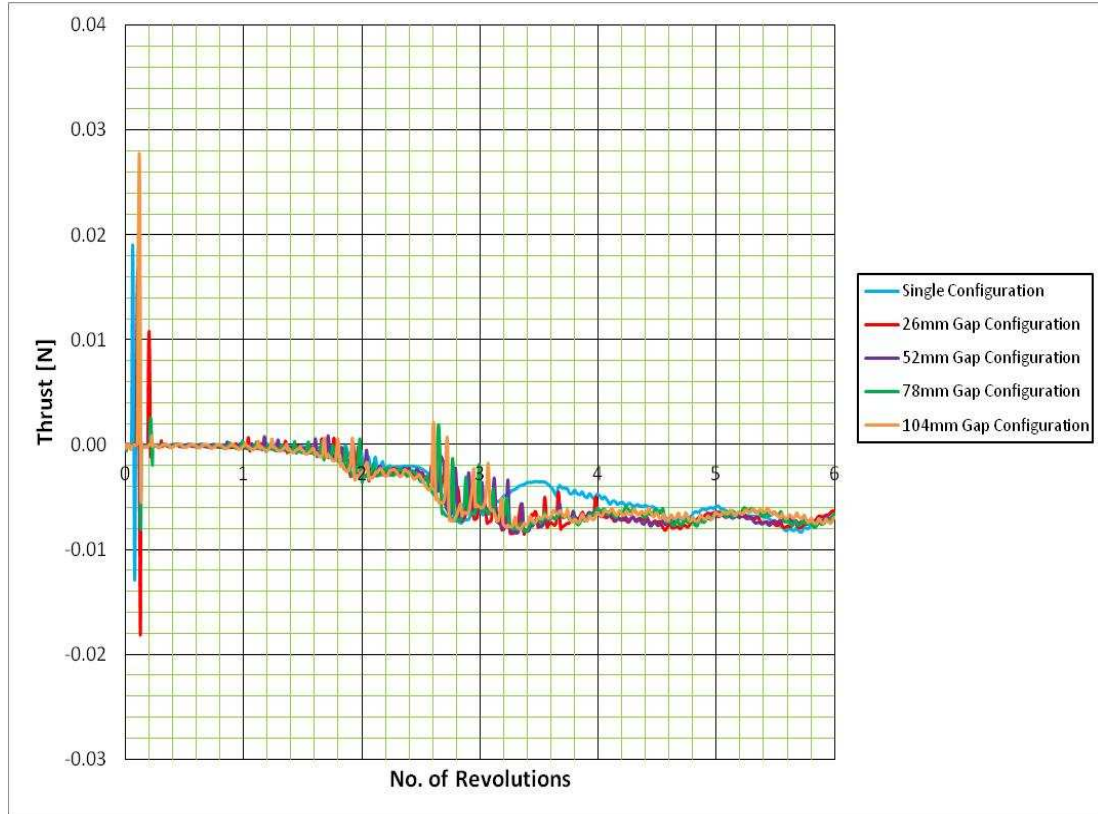


Figure 17. Plot of thrust versus no. of revolutions at 3,000 rpm

As the rotational speed increases, the flow within the CFF based on the torque on the blades remains more or less stable. The flow outside of the CFF although generally stable, has larger fluctuations in the thrust levels as the CFF rotates. This could mean that speed of rotation affects the stability and the time it takes to reach a relatively stable state increases slightly. Figure 18 and Figure 19 show the torque versus number of revolutions and thrust versus number of revolutions for a rotational speed of 8,000 rpm, respectively and the same unstable pattern observed as compared to the run at 3,000 rpm.

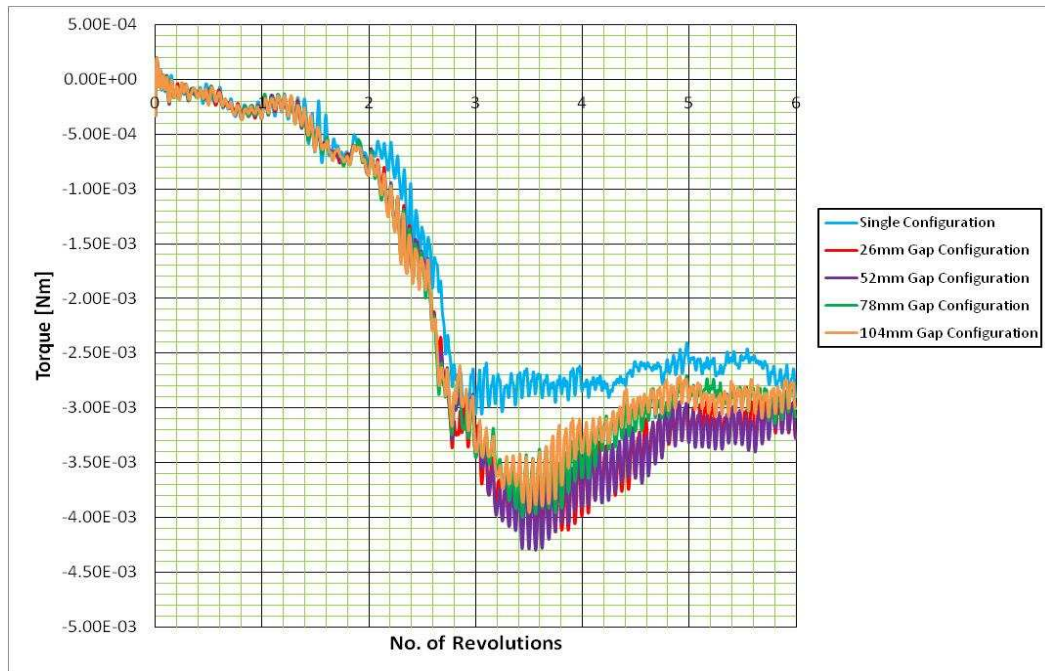


Figure 18. Plot of torque versus no. of revolutions at 8,000 rpm

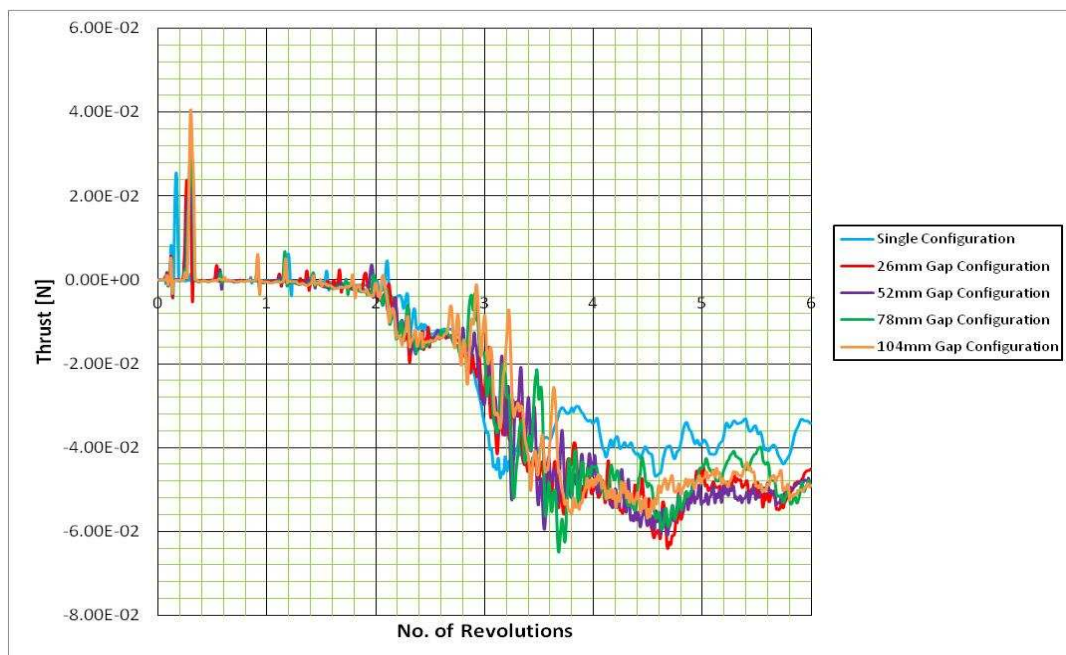


Figure 19. Plot of thrust versus no. of revolutions at 8,000 rpm

The flow visualizations were obtained from CFX-POST and three graphical plots of velocity contour, velocity streamline and velocity vector were extracted. These three plots for each permutation of rotational speed and gap size can be found in Appendix E. It was found that the flow through the CFF did not exit the CFF exhaust vertically downwards. Instead, it was vectored generally about 39° to 45° away from the vertical plane. This could possibly mean that thrust is lost as not all the thrust generated is used to push the CFF off the ground (resolving of forces). Furthermore, it was also observed from the flow visualizations that significant vortices were present within the CFF (especially near the region of the housing with a sharp right angle turn). This could possibly result in a less effective flow generated. It was also seen that for the dual CFF configuration, entrainment was present. Entrainment (significant) was not observed for the single CFF configuration.

From the thrust monitor points described earlier, it was found that the flow took time to develop before it stabilized. The thrust was calculated by averaging the thrust generated for the last two revolutions (5th to 6th revolution of simulation) where the flow became generally stable. Figure 20 shows the plot of simulation thrust versus rotational speed for the single and dual CFF configurations.

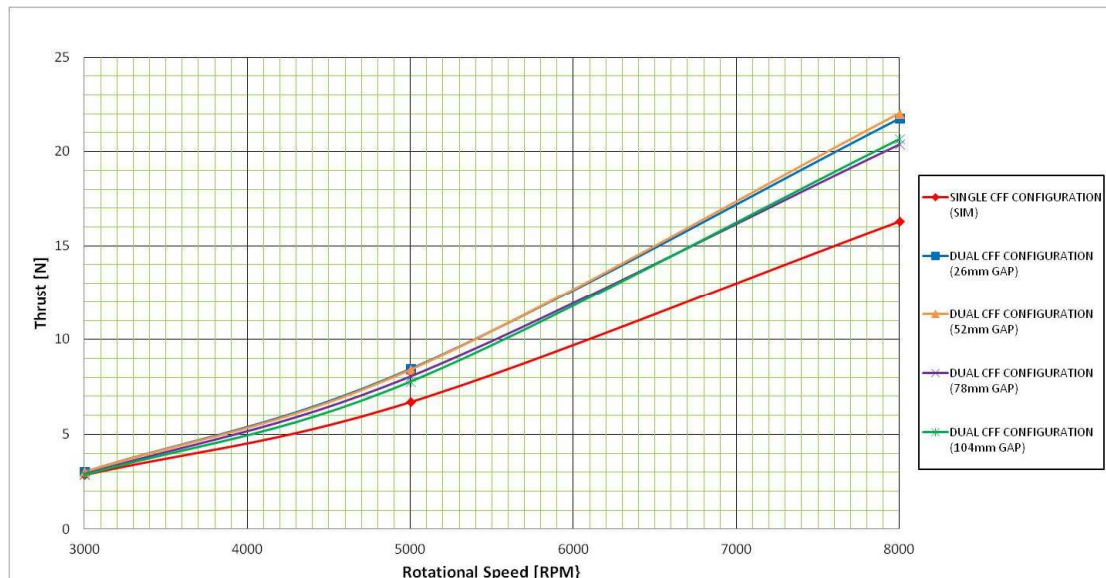


Figure 20. Plot of simulation thrust versus rotational speed

Based on the simulation results, it can be seen that the thrust generated by the dual CFF configuration was higher than the single CFF configuration, meaning that this configuration leads to thrust augmentation. While this is not significant at low rotational speeds, as speed increases, the thrust augmentation increases. The dual CFF configuration with the 52 mm gap showed the highest thrust augmentation.

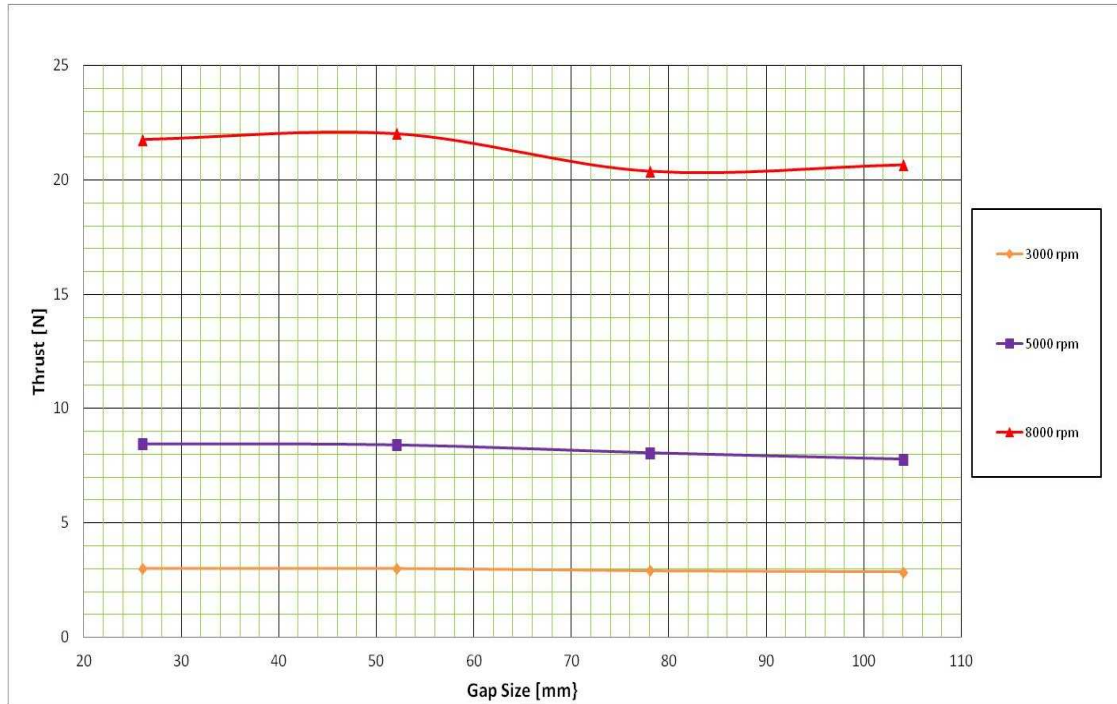


Figure 21. Plot of simulation thrust versus gap size

Plotting the data from another perspective as seen in Figure 21 (thrust versus gap size), it can be seen that there is an optimal gap size especially at high speeds (8,000 rpm). This optimal point is the 52 mm gap, where, as the gap increases, the thrust increases until it reaches the optimal gap before it decreases.

Figure 22 shows the plot of the percentage thrust increase (compared with the single CFF configuration) versus gap size. It can be seen that the thrust increase is not significant with values of around 5% for low speeds. Higher speeds see percentage thrust increases of greater than 20% at near the optimal point. In fact, for a rotational speed of 8,000 rpm at the 52 mm gap, the thrust augmentation is at a high of around 36%.

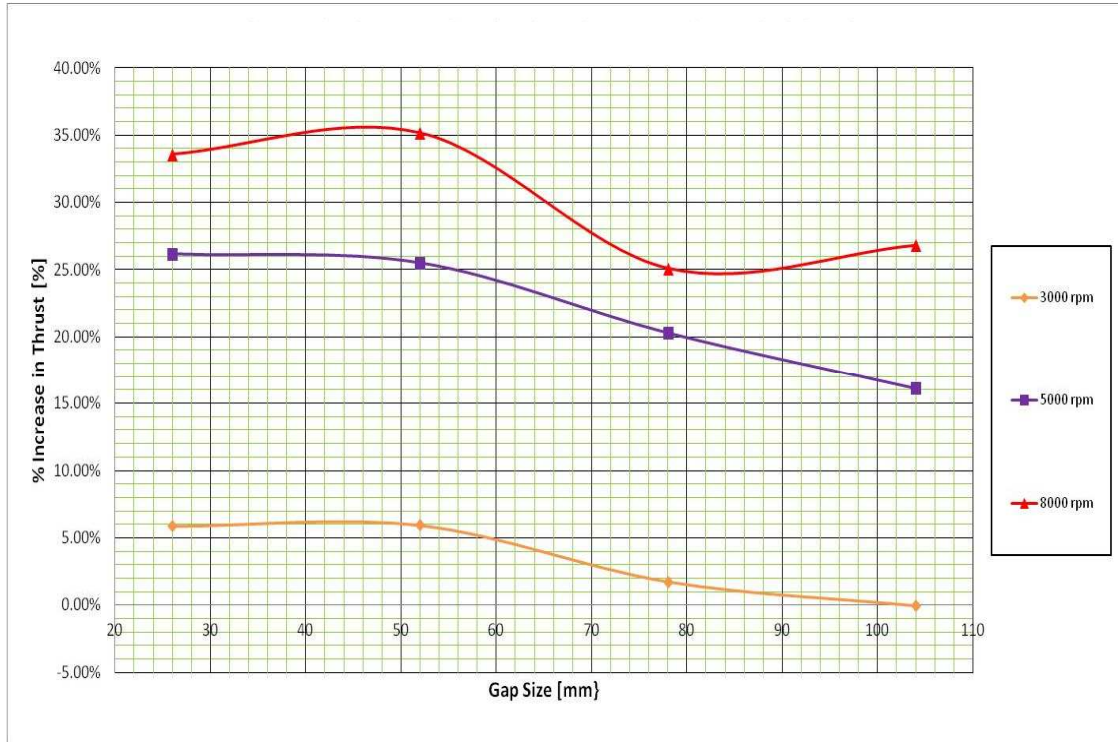


Figure 22. Plot of simulation percentage increase in thrust versus gap size

The simulation results seem to point to successful thrust augmentation when the dual CFF configuration is used. The possible reason for thrust augmentation could likely be due to the entrainment downwards through the gap where entrained flow is significantly higher for the dual CFF configuration as compared to the single CFF configuration. The higher the rotational speed, the greater the entrainment effect and thus thrust increase.

B. EXPERIMENTAL MEASUREMENTS

It was discovered that the air flow going through the gap between the CFFs was upwards. Figure 23 shows the air flow through the gap going upwards when the ground plane (thrust balance) was about 60 mm from the exhaust of the CFFs. The initial hypothesis was that combining two CFFs in a dual CFF configuration would cause the air in the gap region to be entrained downwards together with the CFF outlet air flows, thus increasing the thrust generated. Furthermore, the dual CFF configuration caused the flow to be very unstable, contrary to the stable flow experienced in the single CFF

configuration. This instability was observed from the large oscillations encountered on the weighing scale while measuring the thrust generated. In fact, as the gap became smaller, the flow became more unstable. Lower air flow stability also coincided with lower thrust levels. This was especially pronounced at high rotational speeds (6,000 rpm and above). However, it was also found that low rotational speeds of around 3,000 rpm did not have significant stability problems with reducing gap size.

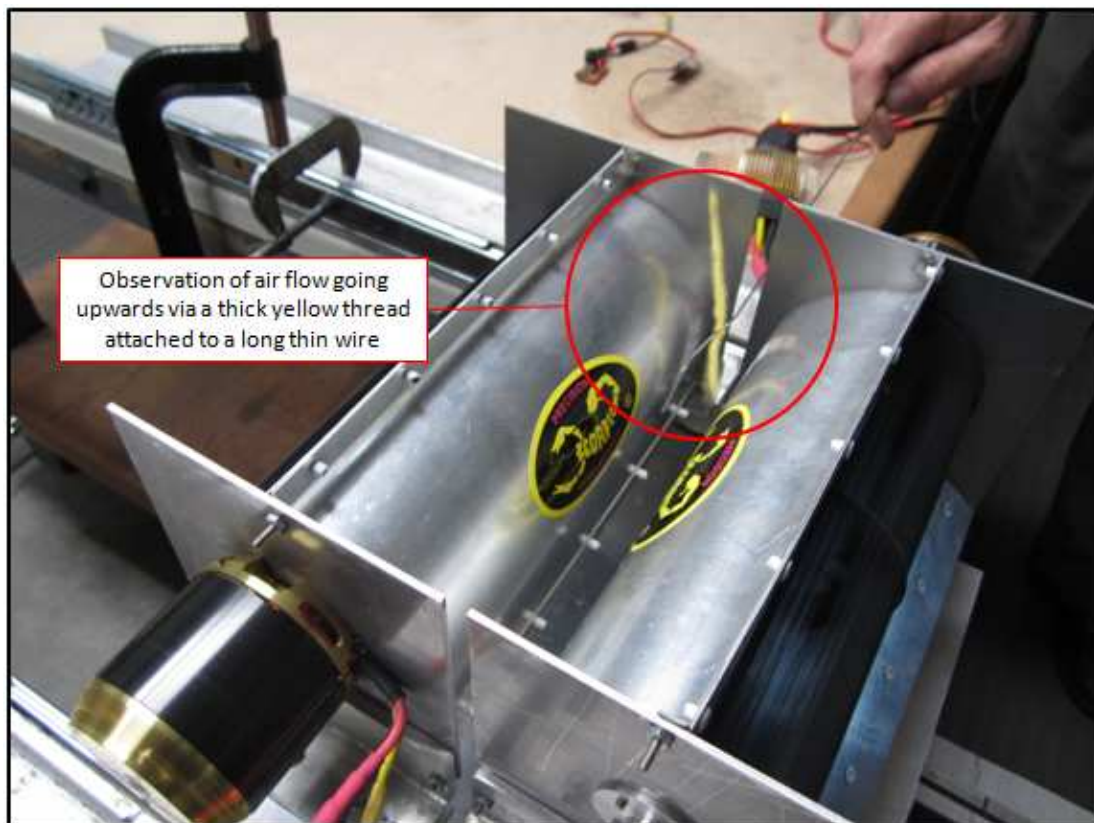


Figure 23. Upward flow through the gap between the two CFFs

A possible explanation for reversed flow was due to the fact that the air flow coming out of the CFFs was immediately re-ingested into the CFFs, leading to unstable flow generated as the CFF rotor rotated. The flow from a single configuration CFF would ingest the relatively still or slow moving air in the surrounding and exit through the outlet. When the air flow impinges vertically down on the weighing scale plate, the flow is split into two, moving parallel to the surface of the weighing scale plate in opposite

directions. There is little or insignificant recirculation of this flow going back into the CFF. However, when the CFFs are placed in a dual CFF configuration, the split flow on the side of the gap (symmetry plane between the two CFFs) from the first CFF encounters the split flow from the second CFF. This means that the high momentum air mass in that region has only one direction it can move to (i.e., upwards). This re-circulated air flow is therefore re-ingested by the CFFs. The illustrations of the above explanation can be found in Figure 24 and Figure 25.

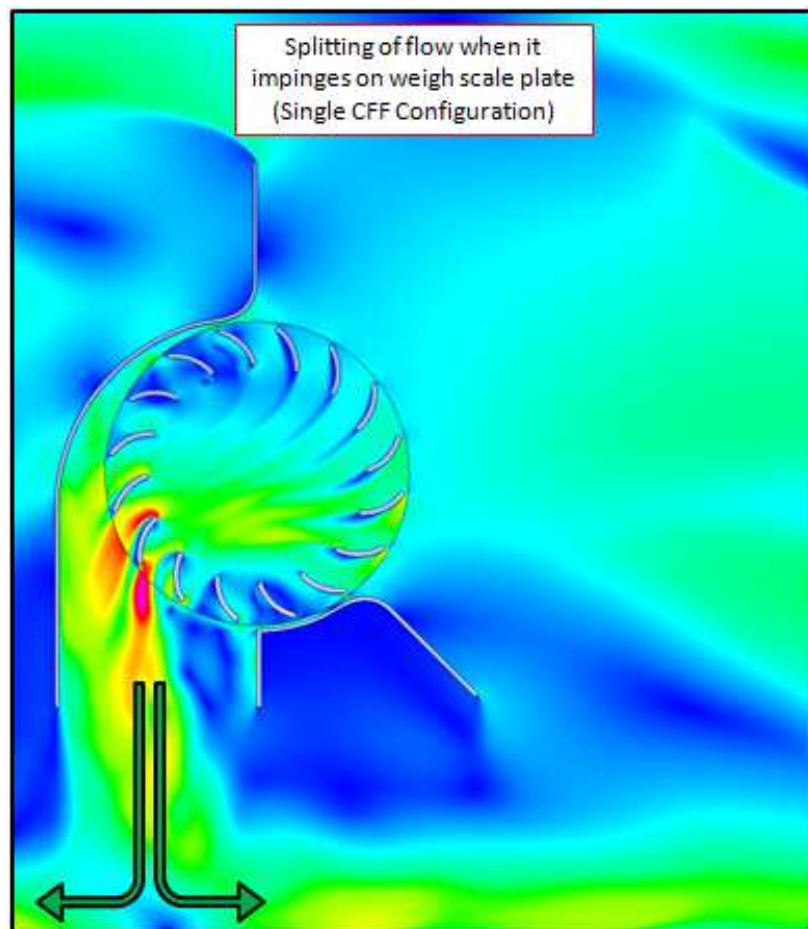


Figure 24. Schematic of splitting of flow in a single CFF configuration

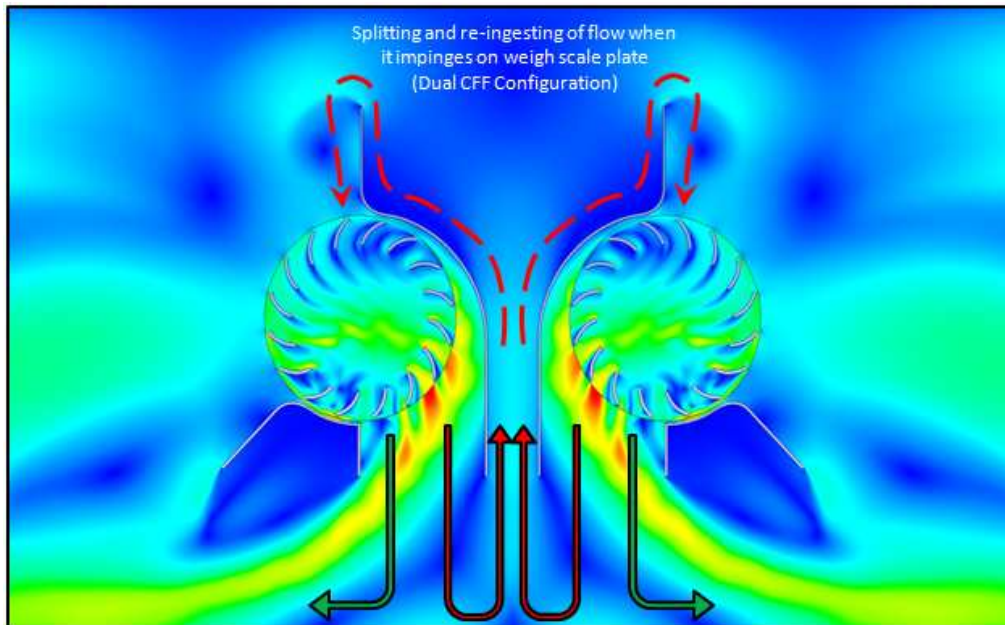


Figure 25. Schematic of splitting and re-ingestion of flow in a dual CFF configuration

The measured thrusts recorded were used to plot the thrust versus rotational speed curve for each of the five configurations (single, 26 mm gap, 52 mm gap, 78 mm gap and 104 mm gap) as shown in Figure 26. The data for the experiment can be found in Appendix F.

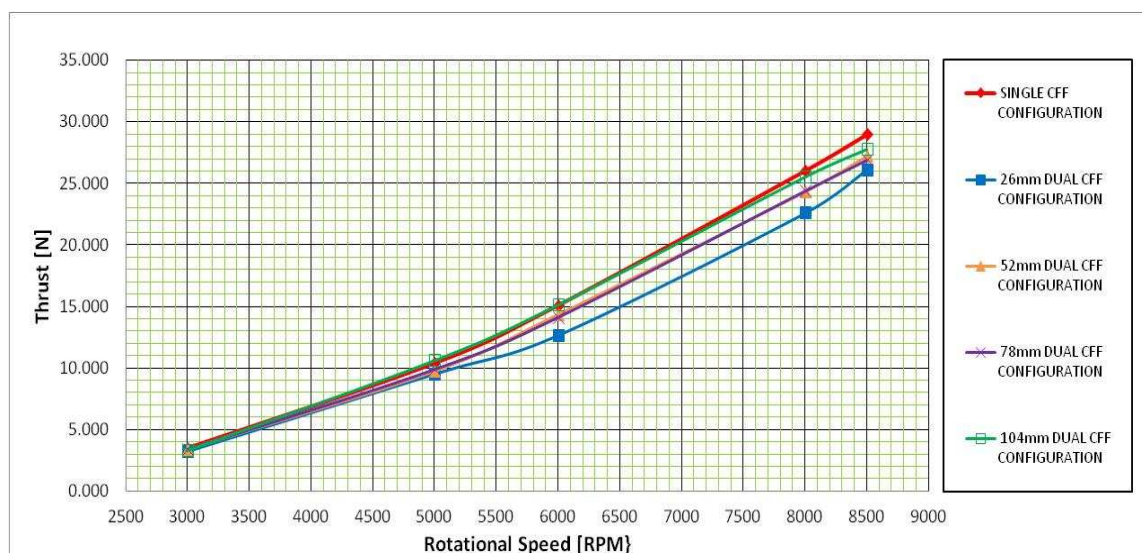


Figure 26. Plot of experimental thrust versus rotational speed

Based on the experimental results, the dual CFF configuration does not lead to thrust augmentation. A loss in thrust was mostly experienced regardless of gap size or rotational speed. However, at low speeds, the configuration seems to have little or no effect on the thrust developed. It is only as the rotational speed increases that the thrust generated starts to drop drastically. The reduction in thrust generated was not as obvious at speeds of 5,000 rpm and less (data in Table 18 to 22). In fact, the smaller the gap size the larger the reduction in thrust generation. This trend was found to be true for all four gap sizes.

A graph of thrust versus gap size at different rotational speeds was also plotted (Figure 27). The dual CFF configuration did not see any noticeable trends for runs at lower rotational speeds such as 3,000 rpm and 5,000 rpm. However, a trend could be seen for the other three higher rotational speeds where the thrust increases as the gap increases. This happens until it reaches a maximum at a gap of 52 mm before the thrust dips to a minimum at 78 mm and then climbing up again. While this seems to show a fluctuation in the thrust with gap size, there is a slight trend whereby the thrust increases as the gap size increases (data in Table 23).

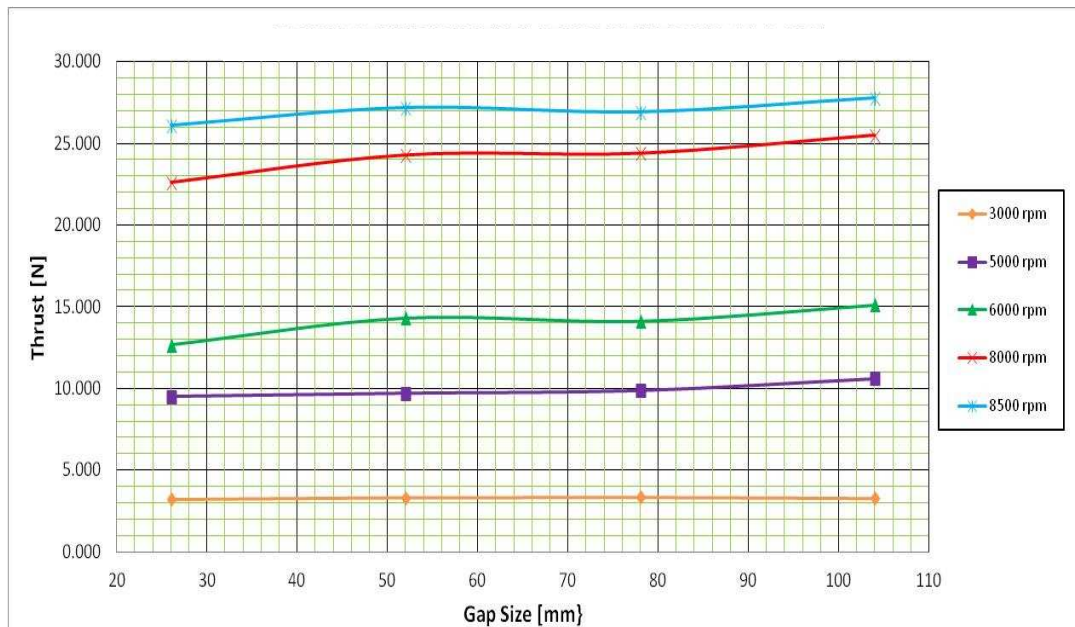


Figure 27. Plot of experimental thrust versus gap size at different rotational speeds



Figure 28. Plot of experimental percentage change in thrust versus gap size

From the plot of percentage change in thrust versus gap size, it has been observed that a speed of 5,000 rpm seems to perform the best out of all the five speeds tested. The general trend was relatively similar for the different speeds (except 3,000 rpm), where the percentage loss in thrust reduced as the gap size increased. The highest loss of about 16% was found to be the run at 6,000 rpm with a 26 mm gap while there were two instances (5,000 rpm and 6,000 rpm) where there were actually increases in thrust of about 2% and 0.2% for the 104 mm gap size. Figure 29 shows the average percentage change in thrust versus gap size and the general trend is similar to that of those at the individual speeds. The percentage loss in thrust ranged from an average of about 2% to 11% (data in Table 23 and 24).

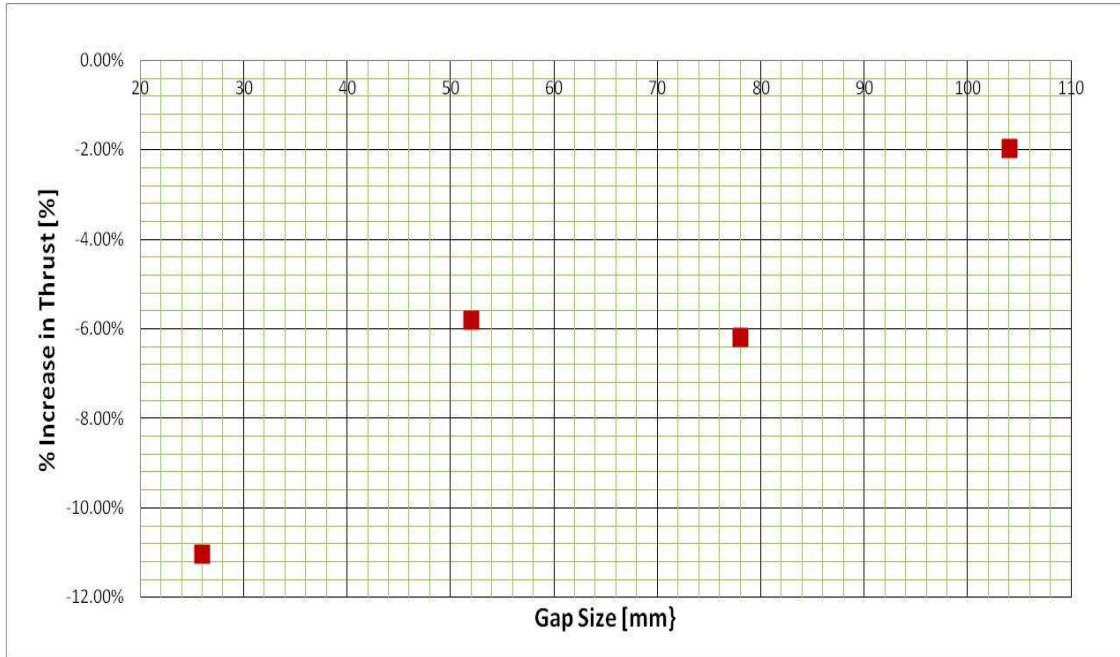


Figure 29. Plot of experimental average percentage change in thrust versus gap size

Based on the physical observations and the experimental data as described above, it can be deduced that combining two CFFs in a dual CFF configuration negates the thrust as compared to a single CFF configuration due to the reverse flow found at the gap and the presence of a solid wall (weighing scale plate) close to the outlets of the CFFs. Entrainment of the air flow which contributes to thrust generation is lost at the gap, which results in overall loss in thrust.

C. ANALYTICAL VERSUS EXPERIMENTAL RESULTS

Comparing the analytical and experimental (based on described experimental setup) results, it seems that the results contradict one another. While the analytical results showed an increase in thrust generated by the dual CFF configuration, the experimental results showed a loss in thrust. Furthermore, instead of the reverse backflow at the gap discovered in the experiment, the simulation showed that entrainment occurred through the gap which contributed to the increase in thrust as compared to the single CFF configuration.

Another simulation on ANSYS-CFX was done on the same model for the case of a single CFF configuration model and a 26 mm gap dual CFF configuration model running at 5,000 rpm. Instead of placing an “outlet” boundary condition at the bottom plane, a “wall” boundary condition was placed. This wall is at a distance of about 60 mm away from the CFF exhaust, simulating exactly where the distance between the weighing scale plate and CFF exhaust in the experiment.

Figures 30 and 31 show the torque and thrust monitor plots, respectively, for such a scenario. From both plots, it can be seen that the flows inside the CFFs and flow outside the CFFs have yet to reach a stable state even after six revolutions. Based on Delagrange’s torque and thrust monitor plots [6] as well as those from section A of this chapter, the torque and thrust stabilizes after the fourth revolution. On top of not reaching a stable state, the fluctuations, especially for the thrust are especially high.

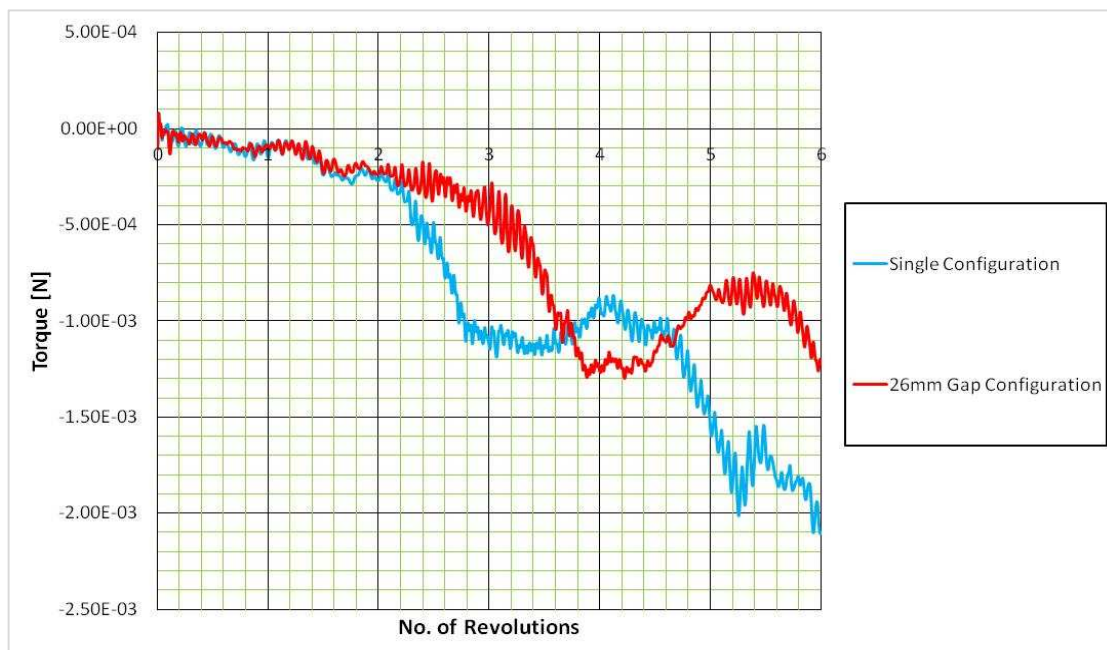


Figure 30. Plot of torque (wall B.C.) versus no. of revolutions at 5,000 rpm

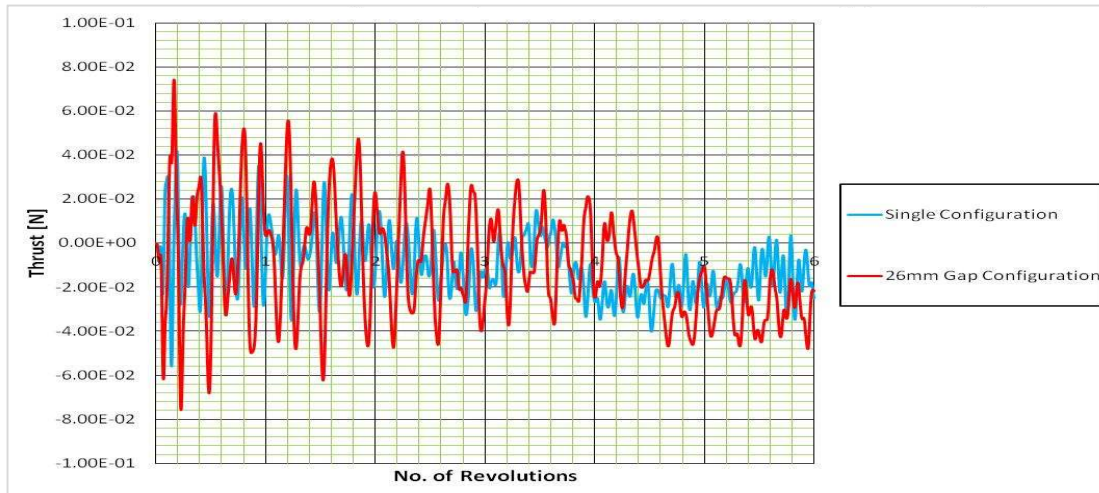


Figure 31. Plot of thrust (wall B.C.) versus no. of revolutions at 5,000 rpm

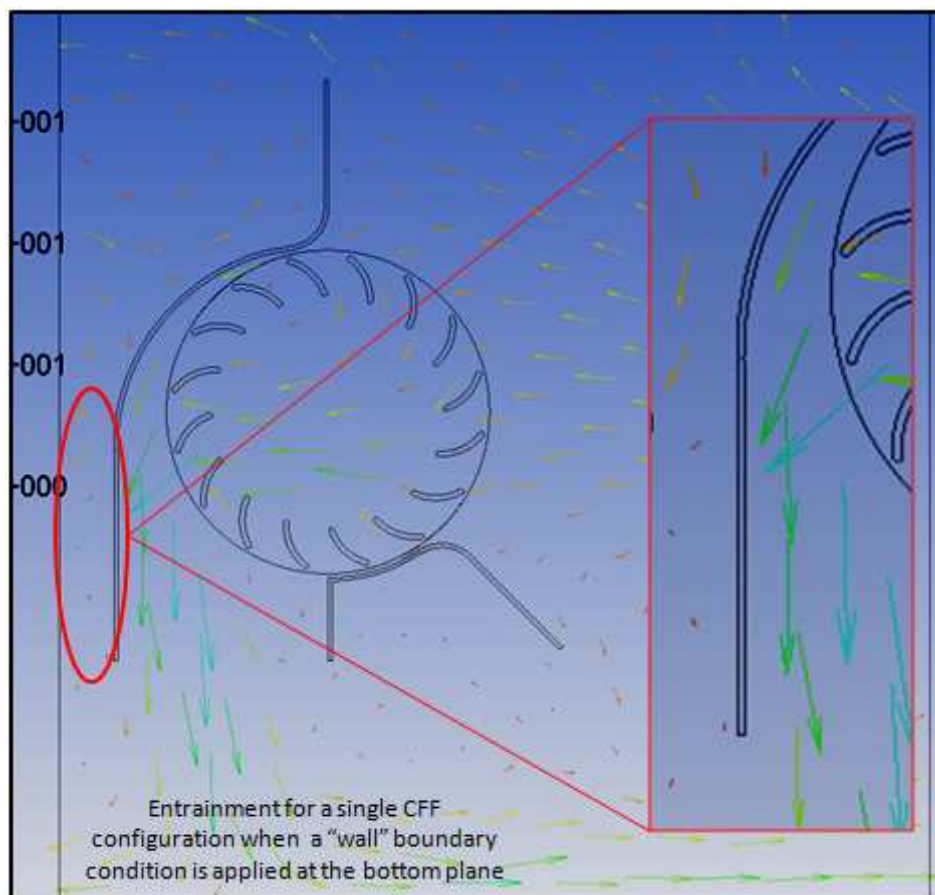


Figure 32. CFX simulation for a single CFF configuration when a “wall” boundary condition is applied at the bottom plane

Figure 32 shows the velocity vector flow for the single CFF configuration. It can be seen that the operation of the single CFF configuration already produces entrainment close to the left outer wall of the housing. The entrainment can be seen to be flowing in the same direction of the CFF exhaust flow.

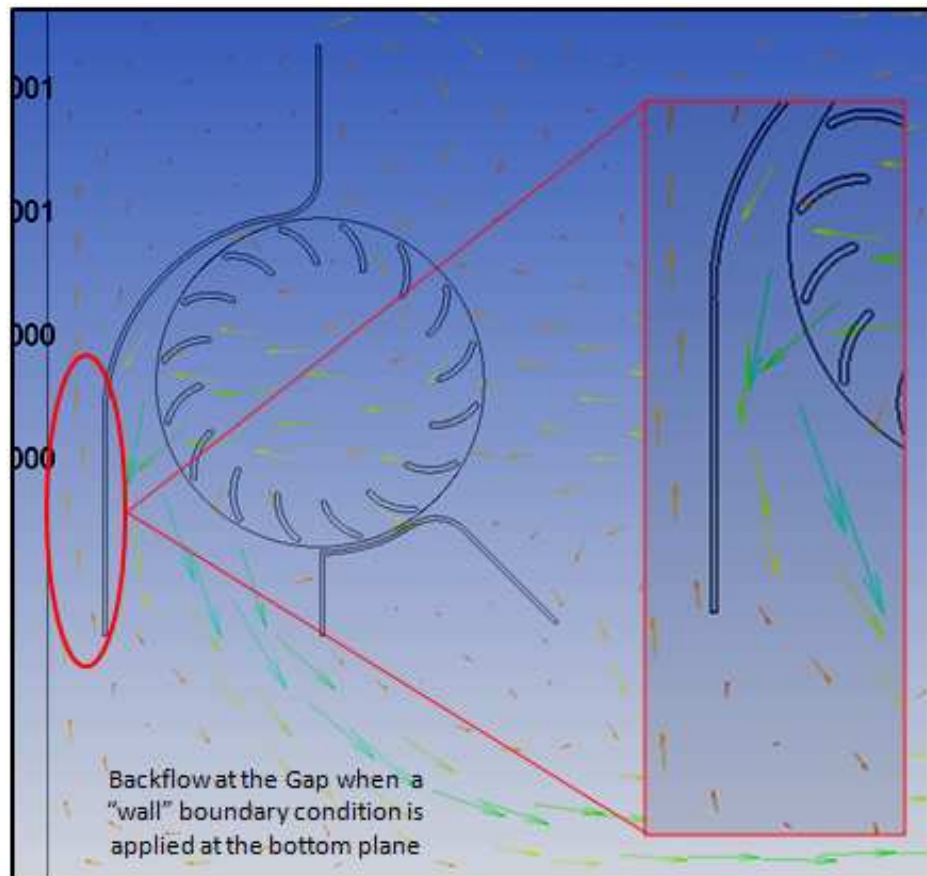


Figure 33. CFX simulation for a dual CFF configuration when a “wall” boundary condition is applied at the bottom plane

However, when the dual CFF configuration was used, backflow up the gap between the two CFFs was found to occur as shown in Figure 33. This matched the physical observation of the air flow in the experiment discussed in section B of this chapter. It can possibly be deduced that while the single CFF configuration experiences no ill effects by being placed near the ground, the opposite can be said to be true for the dual CFF configuration. This means that the dual CFF configuration might not work well

close to the ground and there needs to be a minimum distance between the exhaust and the ground for thrust augmentation to occur. The thrust calculated from the simulation was found to be 10.85 N and 9.19 N for the single CFF configuration and the dual CFF configuration, respectively. This meant that the percentage loss in thrust is about 15%. The experimental results for the former and latter were 10.39 N (about -4% difference) and 9.52 N (about 3.5% difference) giving a percentage loss in thrust of about 9%. This makes the analytical and experimental results very similar to each other, showing that the hypothesis on the closeness of the CFF to the wall affecting measurement of actual thrust augmentation could be true. Therefore, an experiment with larger exhaust to wall distance was necessary for further verification.

D. LARGER EXHAUST-GROUND DISTANCE EXPERIMENTAL RESULT

Another experiment similar to that described in Chapter III was conducted. However, instead of placing the weighing scale where the scale plate was about 60 mm away from the CFF exhaust, the distance between the two was increased to 260 mm. This was done to determine if possible thrust augmentation of the dual CFF configuration was obscured by the backflow created due to the CFF being placed too close to the ground. This experiment was termed as the “Larger Exhaust-Ground Distance Experiment.”

From physical observations, there was no backflow as observed in the previous experiment at the gap. Instead, it was found that the flow was entrained downwards and the overall flow was relatively stable with very little oscillation of the scale. However, it was noticed that the flow out of the CFF exhausts was not flowing vertically downwards. Instead, it was observed that the flow was exiting the exhaust about 45° from the vertical axis. Some of the flow was found flow outside of the plate of the weighing scale. This could possibly mean that not all the flow was captured by the weighing scale and could be recording thrust levels lower than what was actually generated.

The data can be found in Appendix G. On top of the four gap sizes of 26 mm, 52 mm, 78 mm and 104 mm, an additional gap size measuring 18 mm was conducted as well. This was done for the 3,000 rpm, 5,000 rpm, 6,000 rpm, 8,000 rpm and 8,500 rpm. Figure 34 shows the thrust versus rotational speed plot for the mentioned configurations.

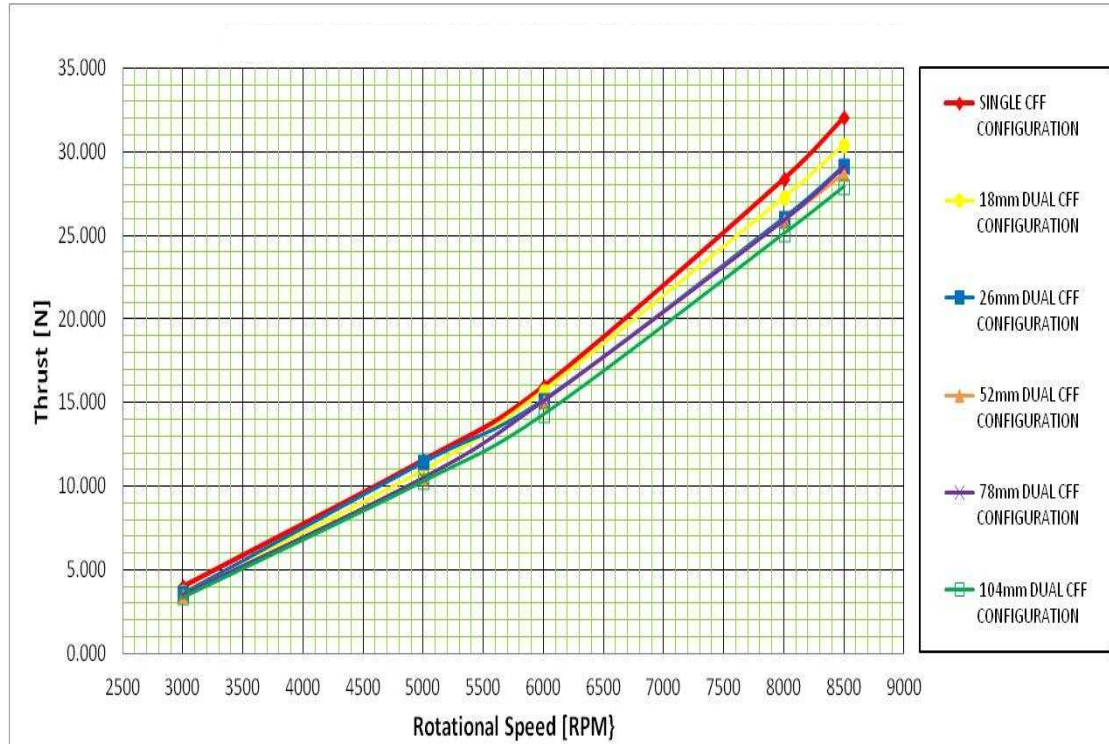


Figure 34. Plot of larger exhaust-ground distance experimental thrust versus rotational speed

It can be seen that the dual CFF configuration does not lead to thrust augmentation contrary to what was observed in the simulation (“outlet” B.C. at the bottom plane). In fact, a loss in thrust was mostly experienced regardless of gap size or rotational speed. The only similarity between the two is that at low speeds, the configuration seems to have no effect in the thrust developed. Also, as the rotational speed increases, the thrust reduction increases even more.

Plotting the experimental thrust versus different rotational speeds, it was found that the thrust reduction was not as pronounced when the gap was small as when the gap was large. There was a general trend of almost steady gradual reduction with increasing gap with loss minimized around 18 mm and 26 mm. Data points for rotational speeds 8,500 rpm, 8,000 rpm and 6,000 rpm were found to behave in this similar trend. For the case of the 3,000 rpm, it can be seen that the change in thrust is almost insignificant based on the graph in Figure 35.

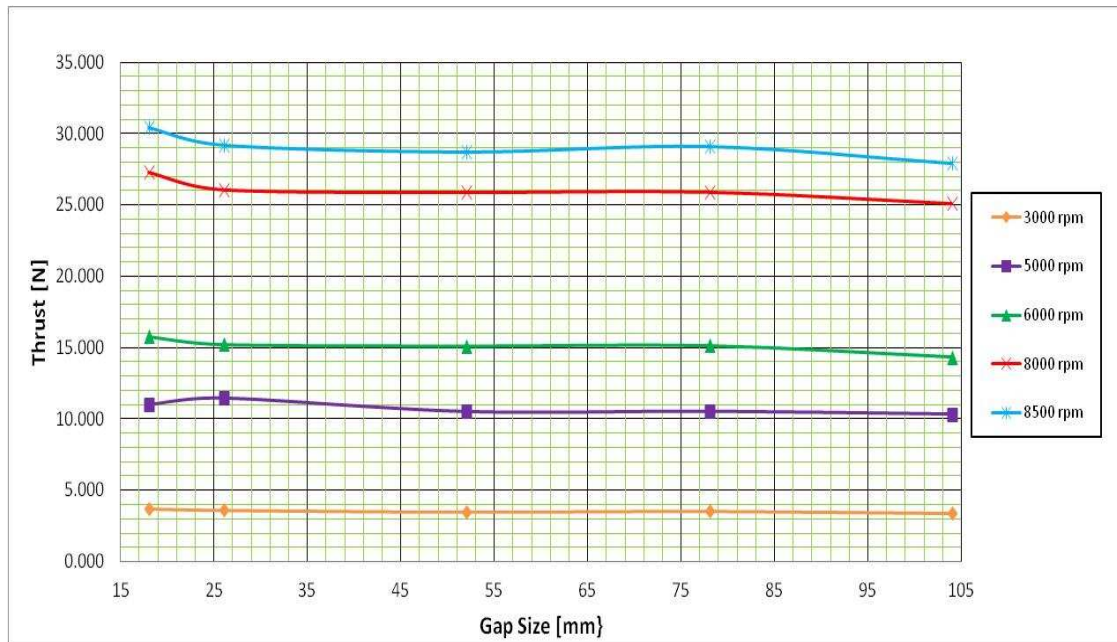


Figure 35. Plot of larger exhaust-ground distance experimental thrust versus gap size at different rotational speeds

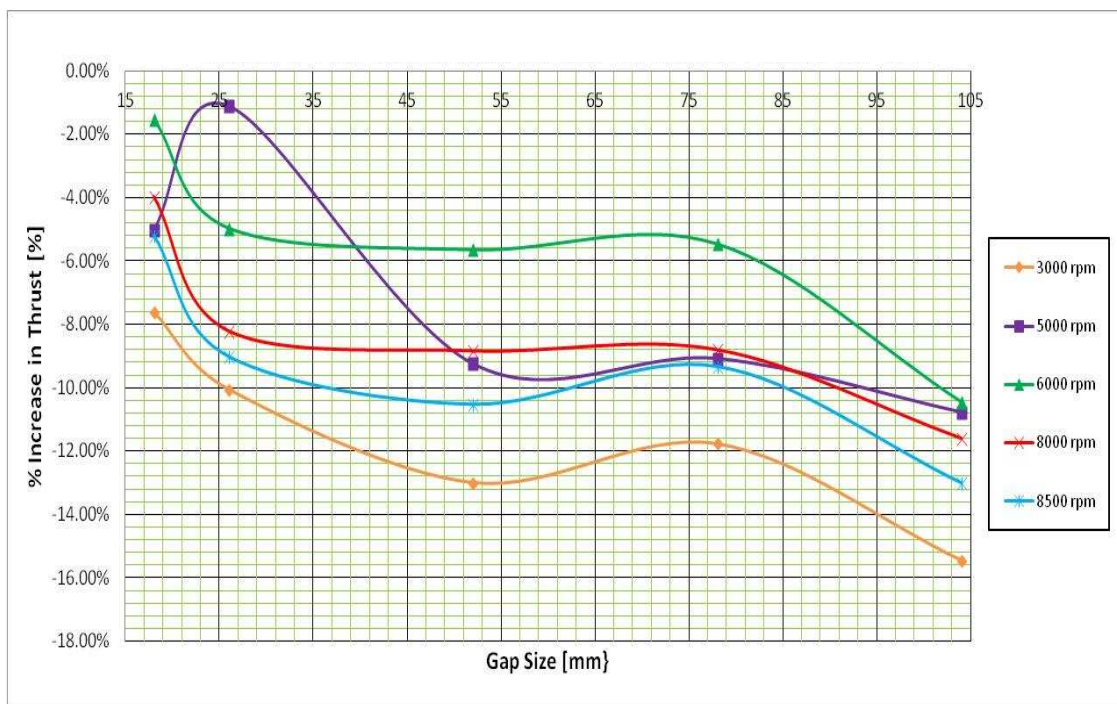


Figure 36. Plot of larger exhaust-ground distance experimental percentage change in thrust versus gap size

To obtain a clearer picture, the percentage change in thrust versus gap size was also plotted (Figure 36). This also subscribed to the general trend where percentage in thrust decreased as gap size increased. However, it was seen that out of all five rotational speeds, the 3,000 rpm run has the worst percentage loss in thrust. This was contrary to what was observed when comparing the actual thrust itself. This was due to the fact that the thrust generated by the 3,000 rpm runs were significantly smaller than the other runs and the true effect of the loss can only be observed by using looking at the percentage change. The 5,000 rpm run was found to suffer the least loss in thrust overall. The average change in thrust versus gap size was plotted in Figure 37 and the general trend is confirmed. The earlier two plots of average percentage change in thrust were also inserted in the graph for comparison.

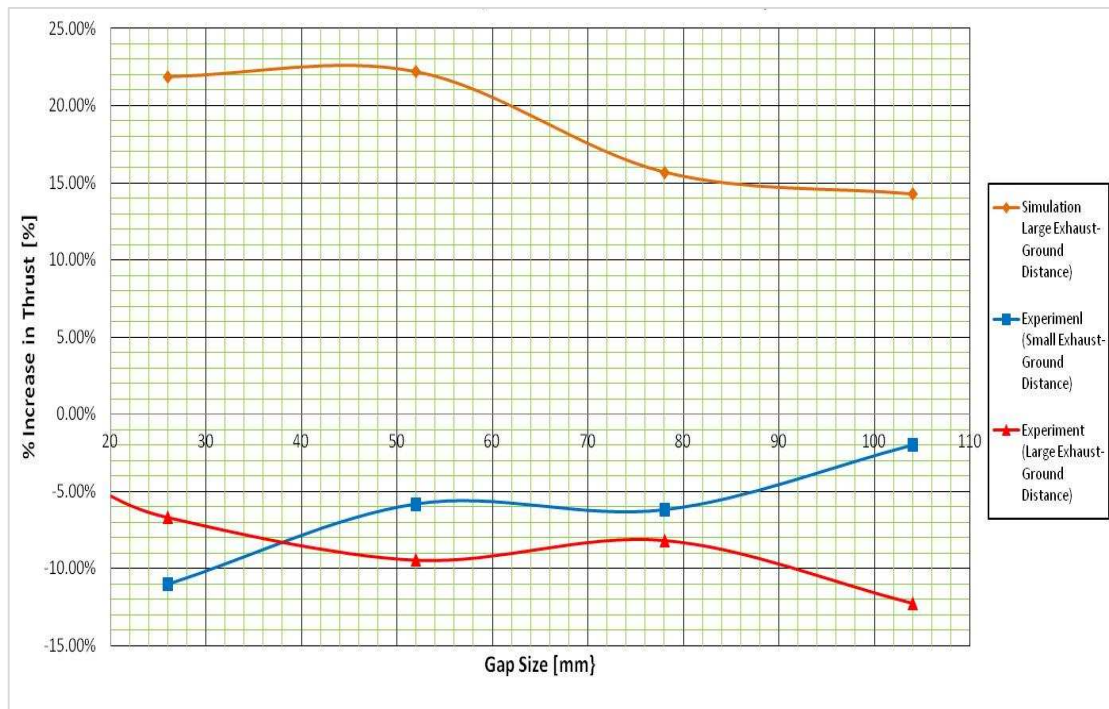


Figure 37. Plot of average percentage change in thrust versus gap size (comparison)

The possible explanation for this loss in thrust experienced as compared to what simulation results (“outlet” B.C. at bottom plane) could be due to a number of reasons. As mentioned earlier, the flow exiting the exhaust was doing so at quite a large angle and

not all the flow was being captured by the weighing scale plate for the dual CFF configuration. This could mean that the thrust measured was not the full thrust generated and a significant amount could have been lost due to insufficient plate size. Another reason could be due to the fact that the dual CFF is able to generate thrust for thrust augmentation when already in flight (off the ground) as seen in the simulation. However, when the CFFs are still on the ground, the flow impinging near the ground is mixed and complex resulting in losses. This would mean that a new simulation will have to be run where the stator domain has to be extended to where the exhaust to bottom plane distance is extended to 260 mm instead of 60 mm and the bottom plane boundary condition changed to a wall instead of an “outlet.” This is because the simulation “outlet” B.C.) could be predicting flow of the dual CFF in flight and far away from the ground. The last possibility could be due to the fact that ANSYS-CFX did not predict the flow well as the stator domain is not large enough. As such, there could be a need to extend the domain so that the top, right and bottom planes can be considered as far-field regions. This would however affect the amount of computational time required and make simulation through ANSYS-CFX uneconomical as compared to just doing the experiment.

E. OVERALL SIMULATION/EXPERIMENT DISCUSSION

Based on all the simulations and experiments conducted, it can possibly be deduced that having a dual CFF configuration might be able to produce thrust augmentation for the air platforms which are already in flight and far off the ground, however, when close to the ground, the adverse effect is felt where there is actually a loss in thrust experienced when comparing with a single CFF configuration. In fact, for a very small exhaust-ground clearance, backflow is experienced through the gap and there is a loss in entrainment effect and a development of unstable flow. Increasing the distance eliminates this backflow and reduces instability. Therefore, there could be a minimum and optimum exhaust-ground distance for the system to work, making it a very sensitive system which is easily affected by minute changes.

V. CONCLUSION AND RECOMMENDATIONS

A. CONCLUSION

The analytical and experimental results were found to be at odds with each other with the simulation showing thrust augmentation with an optimal point of 26 mm gap size for the dual CFF configuration while the experimental results shows not only no thrust augmentation but also a loss in thrust. Possible reasons could be due to unaccounted thrust losses during experimental measurement (insufficient capture area of the weighing scale plate) or poor simulation predictions. Therefore, there might be a need to further refine the experiment and/or simulation to confirm that the dual CFF configuration does not produce the results desired.

However, through this research, a few important observations were learnt. It was noted that the elevation of the CFF exhaust to the ground plays an important part as to whether adverse thrust effects such as backflow are experienced. As seen in the experimental cases where the weighing scale plate was placed very close to the CFF (about 60 mm from the CFF exhaust), the plate created a wall which caused flow to circulate back up through the gap between the two CFFs. The loss of any flow there meant a higher loss of thrust in the configuration. It also led to a creation of unstable flow. The higher the rotational speed and smaller the gap, the lower the thrust generated and more unsteady the flow becomes.

In conclusion, this could possibly mean that the use of the dual CFF configuration for VTOL might not be a viable option and that alternative methods need to be looked at for thrust augmentation for CFF propulsion.

B. RECOMMENDATIONS

The dual CFF configuration by itself does not seem to perform any better than the single CFF configuration for VTOL. Other forms of thrust augmentations might have to be looked into to further increase the thrust generated. One possible area to look at is the

use of an ejector together with the dual CFF configuration. The design of an ejector that could further optimize thrust would be a good step into the direction of a safe, efficient and high thrust VTOL for air platform.

Based on the velocity contour plots of the dual CFF configuration, it was found that unlike a single CFF configuration, the air flow does not thrust vertically downwards, but instead flows out in a jet at an angle of about 45° . This means that there is actually loss of thrust due to this vectoring. In order to minimize this loss, a possible consideration would be to rotate the CFF housings such that the thrust is vectored vertically downwards. This change could possibly see a higher thrust than what was measured in the experiments conducted for this thesis.

Another recommendation is to study if there is an optimal elevation of the CFF exhaust to the ground for the dual CFF configuration. As previously observed in the experiments, placing a wall (in this case the weighing scale plate) close to the CFF causes loss of thrust due to loss of entrainment of air flow downwards. However, increasing the distance between the two saw no backflow through the gap between the two CFFs and could even increase thrust levels to the point that thrust augmentation is actually experienced.

In terms of simulation, there is a possibility of poor prediction of the actual dual CFF configuration scenario. A new stator domain could be created to extend the flow field such that the CFF and housing is small as compared to the surrounding air.

APPENDIX A. ANSYS CFX SETTINGS FOR DUAL CFF (8,000 RPM)

Analysis Type	<p>Basic Settings</p> <ul style="list-style-type: none"> • External Solver Coupling <ul style="list-style-type: none"> ◦ Option: None • Analysis Type <ul style="list-style-type: none"> ◦ Option: Transient • Time Duration <ul style="list-style-type: none"> ◦ Option: Total Time ◦ Total Time: 0.045 [s] • Time Steps <ul style="list-style-type: none"> ◦ Option: Timesteps ◦ Timesteps: 2.0833e-005 [s] • Initial Time <ul style="list-style-type: none"> ◦ Option: Automatic with Value ◦ Time: 0 [s]
Rotor	<p>Basic Settings</p> <ul style="list-style-type: none"> • Location & Type <ul style="list-style-type: none"> ◦ Location: B40 ◦ Domain Type: Fluid Domain ◦ Coordinate Frame: Coord 0 • Fluid and Particle Definitions <ul style="list-style-type: none"> ◦ Fluid 1 <ul style="list-style-type: none"> ▪ Option: Material Library ▪ Material: Air Ideal Gas ▪ Morphology <ul style="list-style-type: none"> • Option: Continuous Fluid ▪ Minimum Volume Fraction: unchecked • Domain Models <ul style="list-style-type: none"> ◦ Pressure <ul style="list-style-type: none"> ▪ Reference Pressure: 1 [atm] ◦ Buoyancy Model <ul style="list-style-type: none"> ▪ Option: Non Buoyant ◦ Domain Motion <ul style="list-style-type: none"> ▪ Option: Rotating ▪ Angular Velocity: 8,000 [rev min⁻¹] ◦ Axis Definition <ul style="list-style-type: none"> ▪ Option: Coordinate Axis ▪ Rotation Axis: Global Z ◦ Mesh Deformation <ul style="list-style-type: none"> ▪ Option: None <p>Fluid Models</p> <ul style="list-style-type: none"> • Heat Transfer <ul style="list-style-type: none"> ◦ Option: Total Energy ◦ Incl. Viscous Work Term: Checked • Turbulence <ul style="list-style-type: none"> ◦ Option: k-Epsilon ◦ Wall Function: Scalable ◦ High Speed (compressible): Unchecked ◦ Turbulent Flux Closure for HT: Unchecked • Combustion <ul style="list-style-type: none"> ◦ Option: None

	<ul style="list-style-type: none"> Thermal Radiation <ul style="list-style-type: none"> Option: None Electromagnetic Model: Unchecked Initialization <ul style="list-style-type: none"> Domain Initialization <ul style="list-style-type: none"> Frame Type: Rotating Coord Frame: Unchecked Initial Conditions <ul style="list-style-type: none"> Velocity Type: Cartesian Cartesian Velocity Components <ul style="list-style-type: none"> Option: Automatic Axial Component: 0 [m s⁻¹] Radial Component: 0 [m s⁻¹] Theta Component: 0 [m s⁻¹] Static Pressure <ul style="list-style-type: none"> Option: Automatic with Value Relative Pressure: 0 [atm] Temperature <ul style="list-style-type: none"> Option: Automatic with Value Temperature: 300 [K] Turbulence <ul style="list-style-type: none"> Option: Medium (Intensity = 5%) 	
Rotor	Blades	Basic Settings <ul style="list-style-type: none"> Boundary Type: Wall <ul style="list-style-type: none"> Location: (automatically fills out) Coord Frame: Unchecked Frame Type: Rotating Boundary Details <ul style="list-style-type: none"> Mass and Momentum <ul style="list-style-type: none"> Option: No Slip Wall Wall Velocity: Unchecked Wall Roughness <ul style="list-style-type: none"> Option: Smooth Wall Heat Transfer <ul style="list-style-type: none"> Option: Adiabatic Sources <ul style="list-style-type: none"> Boundary Source: Unchecked
Rotor	Symmetry	Basic Settings <ul style="list-style-type: none"> Boundary Type: Symmetry Location: Rotor1 Rotor2
Stator	Basic Settings <ul style="list-style-type: none"> Location & Type <ul style="list-style-type: none"> Location: B122 Domain Type: Fluid Domain Coordinate Frame: Coord 0 Fluid and Particle Definitions... <ul style="list-style-type: none"> Fluid 1 <ul style="list-style-type: none"> Option: Material Library Material: Air Ideal Gas 	

		<ul style="list-style-type: none"> ▪ Morphology <ul style="list-style-type: none"> • Option: Continuous Fluid ▪ Minimum Volume Fraction: Unchecked <ul style="list-style-type: none"> • Domain Models <ul style="list-style-type: none"> ○ Pressure <ul style="list-style-type: none"> ▪ Reference Pressure: 1 [atm] ○ Buoyancy Model <ul style="list-style-type: none"> ▪ Option: Non Buoyant ○ Domain Motion <ul style="list-style-type: none"> ▪ Option: Stationary ○ Mesh Deformation <ul style="list-style-type: none"> ▪ Option: None <p>Fluid Models</p> <ul style="list-style-type: none"> • Heat Transfer <ul style="list-style-type: none"> ○ Option: Total Energy ○ Incl. Viscous Work Term: Checked • Turbulence <ul style="list-style-type: none"> ○ Option: k-Epsilon ○ Wall Function: Scalable ○ High Speed (compressible): Unchecked ○ Turbulent Flux Closure for HT: Unchecked • Combustion <ul style="list-style-type: none"> ○ Option: None • Thermal Radiation <ul style="list-style-type: none"> ○ Option: None • Electromagnetic Model: Unchecked <p>Initialization</p> <ul style="list-style-type: none"> • Domain Initialization: Checked <ul style="list-style-type: none"> ○ Coord Frame: Unchecked • Initial Conditions <ul style="list-style-type: none"> ○ Velocity Type: Cartesian ○ Cylindrical Velocity Components <ul style="list-style-type: none"> ▪ Option: Automatic with Value ▪ Axial Component: 0 [m s⁻¹] ▪ Radial Component: 0 [m s⁻¹] ▪ Theta Component: 0 [m s⁻¹] ○ Velocity Scale: Unchecked • Static Pressure <ul style="list-style-type: none"> ○ Option: Automatic with Value ○ Relative Pressure: 0 [atm] • Temperature <ul style="list-style-type: none"> ○ Option: Automatic with Value ○ Temperature: 300 [K] • Turbulence <ul style="list-style-type: none"> ○ Option: Medium (Intensity = 5%)
Stator	Housing	<p>Basic Settings</p> <ul style="list-style-type: none"> • Boundary Type: Wall <ul style="list-style-type: none"> ○ Location: Housing Bottom ○ Coord Frame: Unchecked <p>Boundary Details</p> <ul style="list-style-type: none"> • Mass and Momentum <ul style="list-style-type: none"> ○ Option: No Slip Wall ○ Wall Velocity: Unchecked

		<ul style="list-style-type: none"> Wall Roughness <ul style="list-style-type: none"> Option: Unchecked Heat Transfer <ul style="list-style-type: none"> Option: Adiabatic <p>Sources</p> <ul style="list-style-type: none"> Boundary Source: Unchecked
Housing	Top	<p>Basic Settings</p> <ul style="list-style-type: none"> Boundary Type: Inlet Location: Top Coord Frame: Unchecked <p>Boundary Details</p> <ul style="list-style-type: none"> Flow Regime <ul style="list-style-type: none"> Option: Subsonic Mass and Momentum <ul style="list-style-type: none"> Option: Normal Speed Normal Speed: 1 [ms⁻¹] Turbulence <ul style="list-style-type: none"> Option: Medium Heat Transfer <ul style="list-style-type: none"> Option: Static Temperature Static Temperature: 300 [K] <p>Sources</p> <ul style="list-style-type: none"> Boundary Source: Unchecked
Housing	Right	<p>Basic Settings</p> <ul style="list-style-type: none"> Boundary Type: Opening Location: Right Coord Frame: Unchecked <p>Boundary Details</p> <ul style="list-style-type: none"> Flow Regime <ul style="list-style-type: none"> Option: Subsonic Mass And Momentum <ul style="list-style-type: none"> Option: Entrainment Relative Pressure: 0[atm] Pressure Option: Unchecked Turbulence <ul style="list-style-type: none"> Option: Medium <p>Heat Transfer</p> <ul style="list-style-type: none"> Option: Static Temperature Static Temperature: 300[K] <p>Sources</p> <ul style="list-style-type: none"> Boundary Source: unchecked
Housing	Symmetry	<p>Basic Settings</p> <ul style="list-style-type: none"> Boundary Type: Symmetry Location: Sym1 Sym2 Left
Housing	Bottom	<p>Basic Settings</p> <ul style="list-style-type: none"> Boundary Type: Outlet Location: Bottom Coord Frame: Unchecked <p>Boundary Details</p> <ul style="list-style-type: none"> Flow Regime <ul style="list-style-type: none"> Option: Subsonic

		<ul style="list-style-type: none"> Mass and Momentum <ul style="list-style-type: none"> Option: Static Pressure Relative Pressure: 0 [atm] <p>Sources</p> <p>Boundary Source: Unchecked</p>
Interfaces	Housing to Rotor	<p>Basic Settings</p> <ul style="list-style-type: none"> Interface Type: Fluid Flow Interface Side 1 <ul style="list-style-type: none"> Domain: Housing Region List: HousingInterface Interface Side 2 <ul style="list-style-type: none"> Domain: Rotor Region List: RotorInterface Interface Models <ul style="list-style-type: none"> Option General Connection Frame Change/ Mixing Model <ul style="list-style-type: none"> Option Trans Rotor Stator Pitch Change <ul style="list-style-type: none"> Automatic <p>Additional Interface Models</p> <ul style="list-style-type: none"> Mass and Momentum <ul style="list-style-type: none"> Option Conservative Interface Flux Interface Model <ul style="list-style-type: none"> Option None Conditional Connection Contrl Unchecked <p>Mesh Connection</p> <ul style="list-style-type: none"> Mesh Connection <ul style="list-style-type: none"> Option GGI Intersection Control Unchecked
Solver	Solution Units	<p>Basic Settings</p> <ul style="list-style-type: none"> Mass Units: [kg] Length Units: [m] Time Units: [s] Temperature Units: [K] Angle Units: CHECKED <ul style="list-style-type: none"> Angle Units: [rad] Solid Angle Units: CHECKED <ul style="list-style-type: none"> Solid Angle Units: [sr]
Solver	Solver Control	<p>Basic Settings</p> <ul style="list-style-type: none"> Advection Scheme <ul style="list-style-type: none"> Option: High Resolution Transient Scheme <ul style="list-style-type: none"> Option: 2nd OrderBE Timestep Initialization <ul style="list-style-type: none"> Option: Automatic Lower Courant Number: Unchecked Upper Courant Number: Unchecked Turbulence Numerics <ul style="list-style-type: none"> Option: First Order Convergence Control <ul style="list-style-type: none"> Min. Coeff. Loops 1

		<ul style="list-style-type: none"> ○ Max. Coeff. Loops 4 ○ Fluid Timescale Control <ul style="list-style-type: none"> ▪ Timescale Control: Coefficient Loops • Convergence Criteria <ul style="list-style-type: none"> ○ Residual Type: RMS ○ Residual Target: 1e-4 ○ Conservation Target: Unchecked • Elapsed Wall Clock Time Control: Unchecked • Interrupt Control: Unchecked <p>Equation Class Settings</p> <ul style="list-style-type: none"> • Equation Class: Continuity, • Continuity: Unchecked <p>Advanced Options</p> <ul style="list-style-type: none"> • Pressure Level Information: Unchecked • Body Forces: Unchecked • Interpolation Scheme: Unchecked • Temperature Damping: Unchecked • Velocity Pressure Coupling: Unchecked • Compressibility Control: Checked • High Speed Numerics: Checked • Total Pressure Option: Unchecked • Clip Pressure for Properties: Unchecked • Minimum Pressure for Properties: Unchecked • Intersection Control: Unchecked
Solver	Output Control	<p>Results</p> <ul style="list-style-type: none"> • Option: Standard • File Compression: Default • Output Equation Residuals: Unchecked • Extra Output Variable List: Unchecked <p>Backup Results: Blank</p> <p>Monitor</p> <ul style="list-style-type: none"> • Monitor Objects: Rotor Torque* Bottom Force* <p>*All objects are defined in expressions</p>

APPENDIX B. SOFASCO CFF EXPERIMENT

A. PRELIMINARY TEST

The idea was to make use of a standard off-the-shelf CFF in housing for a preliminary study of the dual CFF configuration while the housing for the DragonPlate CFF was being designed by Delagrange for his research. Manufactured by SOFASCO, a company producing fans for HVAC, a 1.25-inch diameter, 12-inch span aluminum rotor from the DFA32 series DC CFF was selected for the initial study. Figure 38 shows the fan rotor without the housing. This CFF was to be used to measure the thrust generated for both the dual CFF configuration as well as the single CFF configuration. The thrust measurement for the dual CFF configuration would be conducted at six gap sizes of 7 mm, 11 mm, 9 mm, 14 mm, 18 mm and 25 mm for a range of speeds.



Figure 38. SOFASCO CFF rotor (ruler large divisions in inches)

Two such CFFs were placed in a dual CFF configuration for the test as shown in Figure 39. The SOFASCO CFFs were screwed on to the fabricated brackets and the gap size was adjusted by inserting spacers in the form of metal washers of thickness 1 mm (Figure 40). When clamped together without any spacers, the CFFs were 7 mm apart. The CFFs were powered by an Agilent DC power supply and the rotational speeds changed by adjusting the voltage output.

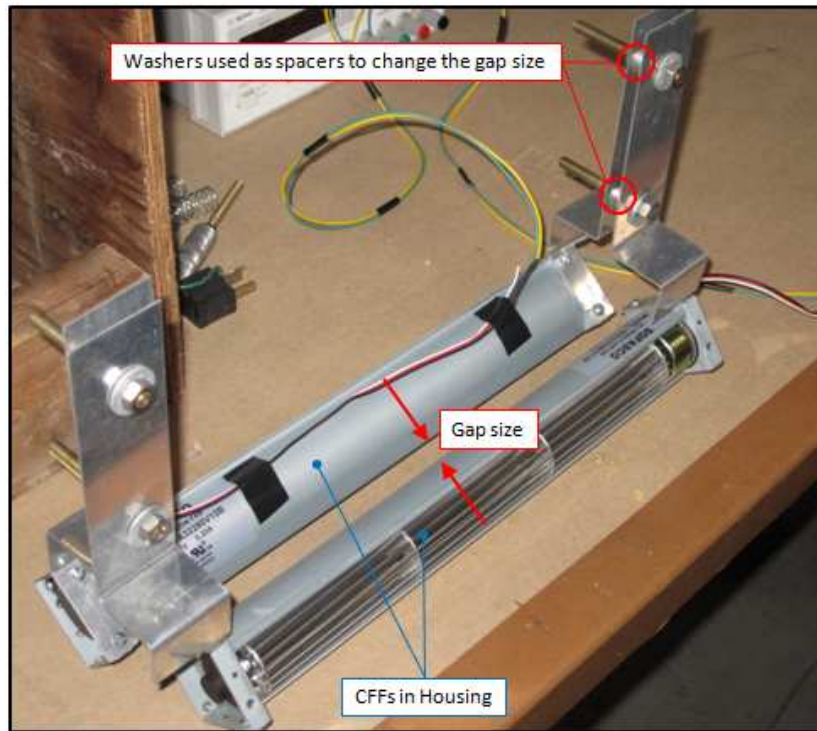


Figure 39. SOFASCO dual CFF configuration

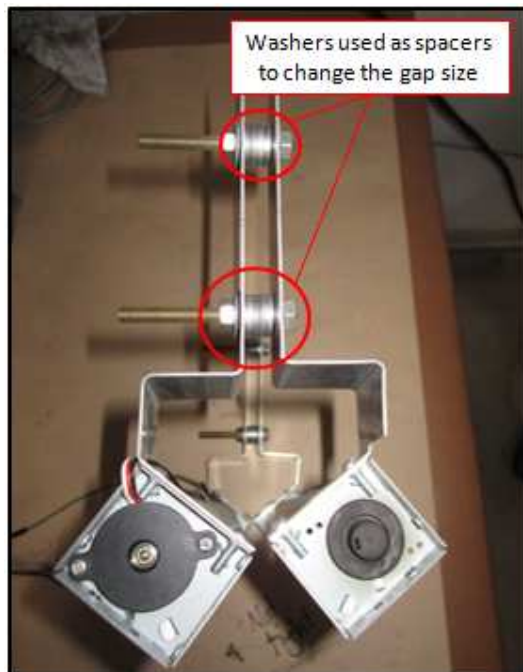


Figure 40. Side view of SOFASCO dual CFF configuration

The whole experimental setup is as seen in Figure 41 below. The Weighing Scale was placed in the center of the Supporting Structure. An Extension Plate was placed on top of the Weighing Scale to increase the surface area that the CFF outlet air flow impinges onto. The CFFs were connected to the DC Power Supply where the rotational speeds were adjusted by changing the voltages. They were each called CFF-A and CFF-B. The rotational speed of each CFF was individually controlled with two voltage setting knobs. The cut-off voltage for the CFF was 11.00V. Increments of 0.50V to 1.00V were done until a maximum of 16.00V for a variation of rotational speeds.

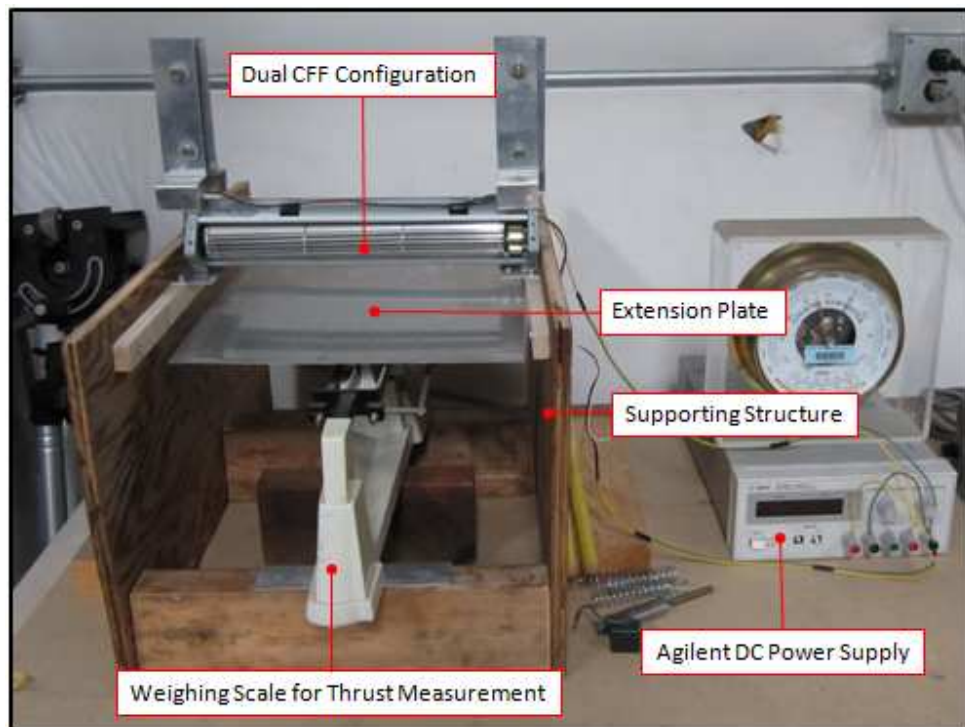


Figure 41. SOFASCO dual CFF configuration experimental setup

The thrust measurement for each individual CFF (single CFF configuration) was recorded at speeds based on eight voltages between 11.00V and 16.00V. The thrust was then added together for comparison with the dual CFF configuration (when both CFFs were turned on). The tables below show the thrust measurements for a single CFF configuration, and the six gap sizes.

Table 4. Experimental data for single CFF

Nominal Voltage [V]	*Estimated Rotational Speed [RPM]	Single CFF							
		CFF-A			CFF-B			Total Thrust [g-f]	Total Thrust [N]
		Voltage [V]	Current [A]	Thrust [g-f]	Voltage [V]	Current [A]	Thrust [g-f]		
11.00	2818.75	11.00	0.203	15.40	10.90	0.197	15.40	30.80	0.3021
12.00	3075.00	12.00	0.229	18.00	11.95	0.223	18.00	36.00	0.3532
13.00	3331.25	13.00	0.254	19.80	12.85	0.244	19.80	39.60	0.3885
14.00	3587.50	14.00	0.278	22.20	13.90	0.270	22.20	44.40	0.4356
14.50	3715.63	14.50	0.289	23.40	14.32	0.282	23.40	46.80	0.4591
15.00	3843.75	15.00	0.304	24.60	14.89	0.290	24.60	49.20	0.4827
15.50	3971.88	15.50	0.314	25.70	15.40	0.310	25.70	51.40	0.5042
16.00	4100.00	16.00	0.325	27.30	15.95	0.319	27.30	54.60	0.5356

Table 5. Experimental data for dual CFF with 7 mm

Nominal Voltage [V]	*Estimated Rotational Speed [RPM]	Dual CFF (7 mm Gap)		
		Thrust [g-f]	Thrust [N]	Percentage Increase In Thrust [%]
11.00	2818.75	31.80	0.3120	3.25%
12.00	3075.00	36.80	0.3610	2.22%
13.00	3331.25	40.90	0.4012	3.28%
14.00	3587.50	45.50	0.4464	2.48%
14.50	3715.63	47.40	0.4650	1.28%
15.00	3843.75	50.20	0.4925	2.03%
15.50	3971.88	52.80	0.5180	2.72%
16.00	4100.00	55.70	0.5464	2.01%
Average				2.41%

Table 6. Experimental data for dual CFF with 9 mm

Nominal Voltage [V]	*Estimated Rotational Speed [RPM]	Dual CFF (9 mm Gap)		
		Thrust [g-f]	Thrust [N]	Percentage Increase In Thrust [%]
11.00	2818.75	32.40	0.3178	5.19%
12.00	3075.00	37.50	0.3679	4.17%
13.00	3331.25	41.90	0.4110	5.81%
14.00	3587.50	46.20	0.4532	4.05%
14.50	3715.63	48.50	0.4758	3.63%
15.00	3843.75	51.00	0.5003	3.66%
15.50	3971.88	53.40	0.5239	3.89%
16.00	4100.00	56.40	0.5533	3.30%
Average				4.21%

Table 7. Experimental data for dual CFF with 11 mm

Nominal Voltage [V]	*Estimated Rotational Speed [RPM]	Dual CFF (11 mm Gap)		
		Thrust [g-f]	Thrust [N]	Percentage Increase In Thrust [%]
11.00	2818.75	32.00	0.3139	3.90%
12.00	3075.00	37.10	0.3640	3.06%
13.00	3331.25	41.10	0.4032	3.79%
14.00	3587.50	45.90	0.4503	3.38%
14.50	3715.63	47.60	0.4670	1.71%
15.00	3843.75	50.40	0.4944	2.44%
15.50	3971.88	53.00	0.5199	3.11%
16.00	4100.00	56.20	0.5513	2.93%
Average				3.04%

Table 8. Experimental data for dual CFF with 14 mm

Nominal Voltage [V]	*Estimated Rotational Speed [RPM]	Dual CFF (14 mm Gap)		
		Thrust [g-f]	Thrust [N]	Percentage Increase In Thrust [%]
11.00	2818.75	32.00	0.3139	3.90%
12.00	3075.00	37.10	0.3640	3.06%
13.00	3331.25	41.20	0.4042	4.04%
14.00	3587.50	45.90	0.4503	3.38%
14.50	3715.63	47.70	0.4679	1.92%
15.00	3843.75	50.40	0.4944	2.44%
15.50	3971.88	52.60	0.5160	2.33%
16.00	4100.00	55.50	0.5445	1.65%
Average				2.84%

Table 9. Experimental data for dual CFF with 18 mm

Nominal Voltage [V]	*Estimated Rotational Speed [RPM]	Dual CFF (18 mm Gap)		
		Thrust [g-f]	Thrust [N]	Percentage Increase In Thrust [%]
11.00	2818.75	31.30	0.3071	1.62%
12.00	3075.00	36.20	0.3551	0.56%
13.00	3331.25	40.50	0.3973	2.27%
14.00	3587.50	45.60	0.4473	2.70%
14.50	3715.63	47.40	0.4650	1.28%
15.00	3843.75	49.50	0.4856	0.61%
15.50	3971.88	52.20	0.5121	1.56%
16.00	4100.00	55.10	0.5405	0.92%
Average				1.44%

Table 10. Experimental data for dual CFF with 25 mm

Nominal Voltage [V]	*Estimated Rotational Speed [RPM]	Dual CFF (25 mm Gap)		
		Thrust [g-f]	Thrust [N]	Percentage Increase In Thrust [%]
11.00	2818.75	31.40	0.3080	1.95%
12.00	3075.00	36.60	0.3590	1.67%
13.00	3331.25	40.50	0.3973	2.27%
14.00	3587.50	45.40	0.4454	2.25%
14.50	3715.63	47.30	0.4640	1.07%
15.00	3843.75	49.50	0.4856	0.61%
15.50	3971.88	52.10	0.5111	1.36%
16.00	4100.00	55.00	0.5396	0.73%
Average				1.49%

Table 11. Consolidated table of % thrust increase at different gap sizes and speeds

Dual CFF GAP [mm]	Estimated Rotational Speeds [RPM]								Ave. % Thrust Increase
	2819	3075	3331	3588	3716	3844	3972	4100	
7	3.25%	2.22%	3.28%	2.48%	1.28%	2.03%	2.72%	2.01%	2.41%
9	5.19%	4.17%	5.81%	4.05%	3.63%	3.66%	3.89%	3.30%	4.21%
11	3.90%	3.06%	3.79%	3.38%	1.71%	2.44%	3.11%	2.93%	3.04%
14	3.90%	3.06%	4.04%	3.38%	1.92%	2.44%	2.33%	1.65%	2.84%
18	1.62%	0.56%	2.27%	2.70%	1.28%	0.61%	1.56%	0.92%	1.44%
25	1.95%	1.67%	2.27%	2.25%	1.07%	0.61%	1.36%	0.73%	1.49%

B. RESULTS ANALYSIS

The results showed that the average percentage increase in thrust for a 7 mm, 9 mm, 11 mm, 14 mm, 18 mm and 25 mm gap are 2.41%, 4.21%, 3.04%, 2.84%, 1.44% and 1.49%, respectively. The 9 mm gap showed the highest percentage thrust increase.

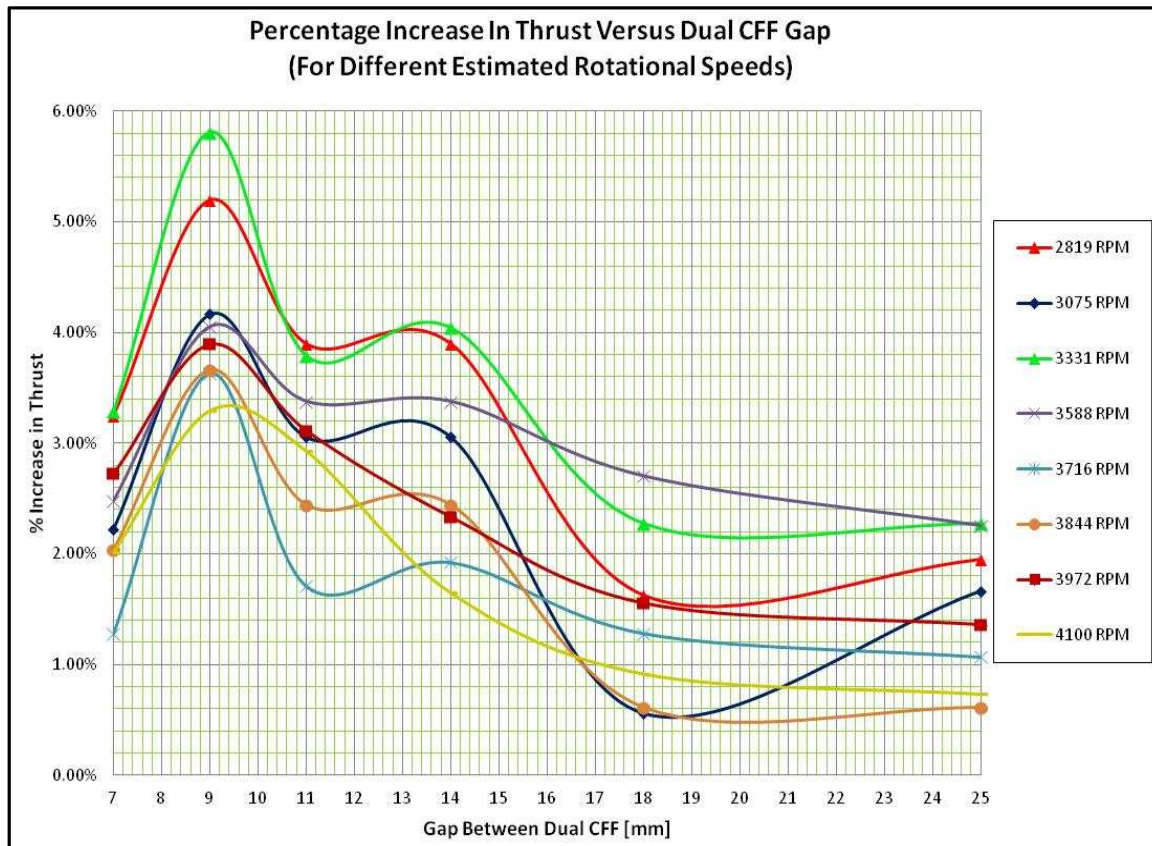


Figure 42. Graph of % thrust increase versus gap size

The percentage thrust increase was plotted against the gap size at different rotational speeds. The graph is as shown in Figure 42. The trend found was that as the gap size increased, the percentage thrust increase increased to a maximum at 9 mm before decreasing. It is also found that there is another secondary local maxima between gaps of 13 mm and 14 mm. This pattern is seen in almost all the eight speeds that the test was conducted at. In fact, when the dual CFF was run at 3,331 rpm, it was found that it had the highest percentage thrust increase of 5.81%. There seemed to be a shift downwards in the percentage thrust increase curve as the rotational speed increased. This could mean that there is possibly a higher thrust augmentation at lower speeds as compared to higher speeds.

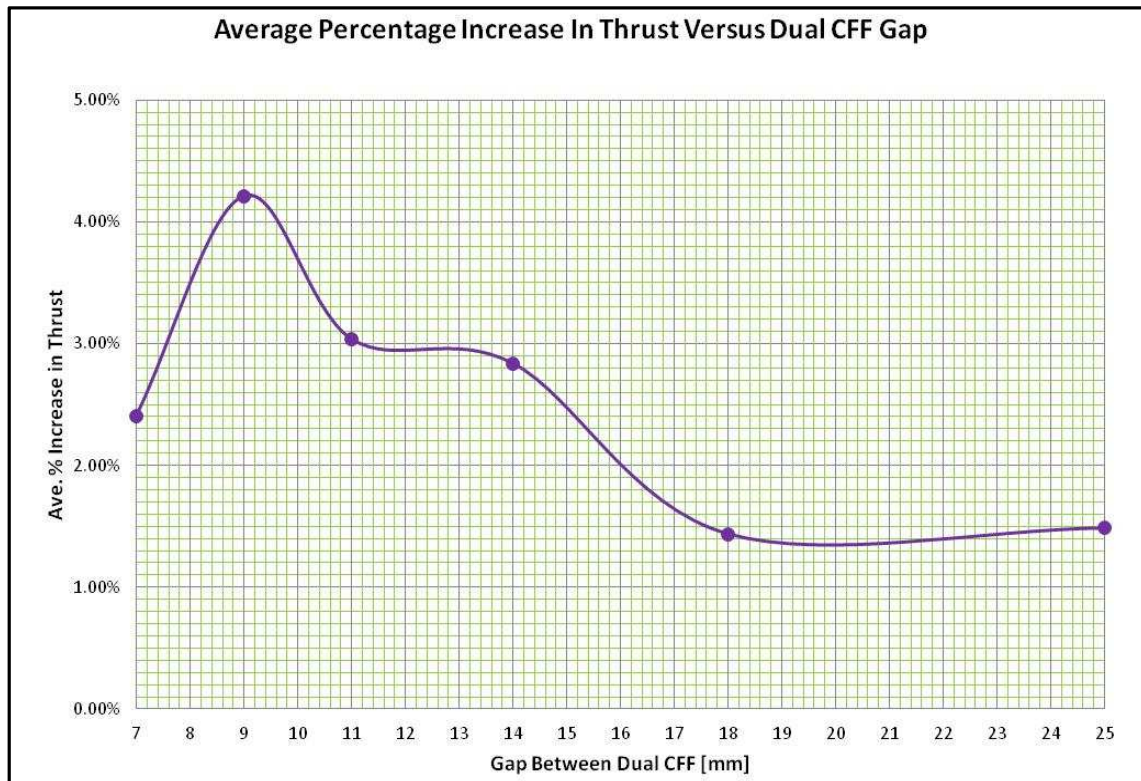


Figure 43. Graph of average % increase in thrust versus gap size

The average percentage increase in thrust was plotted against the gap size and it was found to have a similar shape as that of the curves at each individual rotational speeds. Based on this experiment, it can be seen that there is an optimum gap where the largest thrust augmentation is generated and that as the gap size increases over a certain level, thrust augmentation of the dual CFF configuration will start to deteriorate until there is no longer any significant augmentation effect.

THIS PAGE INTENTIONALLY LEFT BLANK

APPENDIX C. SINGLE CFF EXPERIMENT REPEATABILITY TEST & VALIDATION

A. PURPOSE OF VALIDATION

As a result of a lack of a proper test procedure, the CFF experiment conducted by Delagrange in his thesis [6] was run again to validate the procedure and the repeatability of the results obtained. The experimental procedure was re-constructed and described below. Certain changes were refined and adjusted due to problems encountered reaching higher speeds.

B. EQUIPMENT LIST

- 1x 78 mm Diameter DragonPlate Cross-Flow Fan (in aluminum housing)
- 1x Wooden Fixture
- 2x Giant Clamps
- 1x Controller
- 1x Agilent DC Power Supply
- 1x WaveTek Pulse Generator
- 1x Thermostat
- 1x Giant Weighing Scale
- 1x Laptop installed with “Scorpion ECS Programmer v1.2”
- 1x Stroboscope
- 1x Voltmeter
- 2x ThunderPower (TP) 65C, 6-Cell LiPo Battery (G6 Pro Power) – Battery **A & B**
- 1x ThunderPower (TP) 1340C Balancer
- 1x All State Battery Charger
- Electrical Wires

C. EXPERIMENTAL SETUP

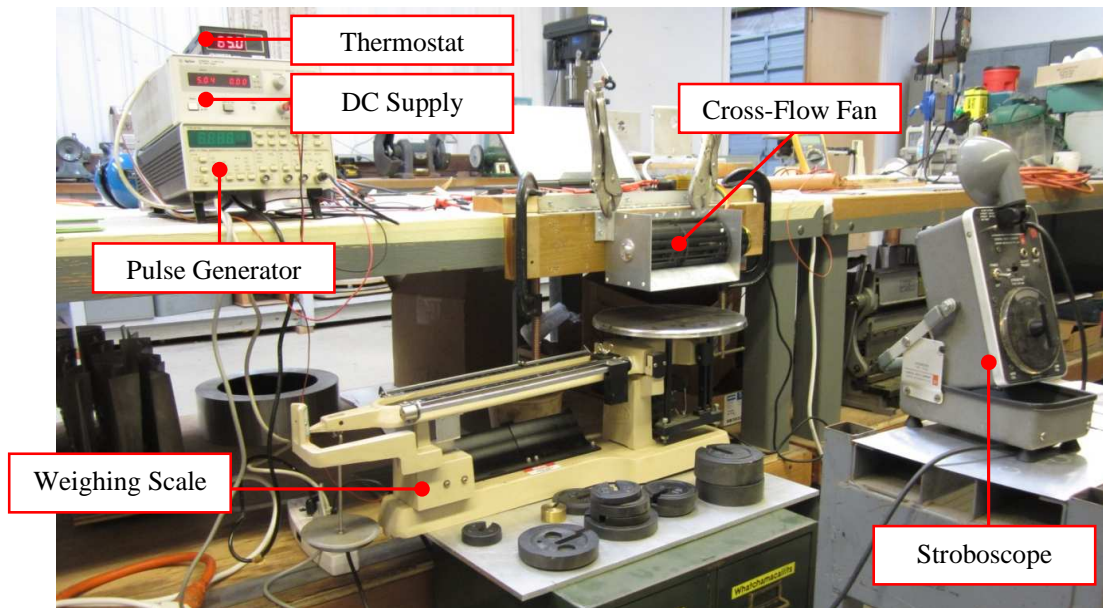


Figure 44. Overall experimental setup and major components

D. PROCEDURE

1. Battery Charging

- a. Connect TP1340C Balancer to ALL STATE Battery Charger.



Figure 45. TP1340C balancer and ALL STATE battery charger

- b. Plug Battery Charger into power socket. Turn the 'Rate' knob (left) clockwise to '3' and the 'Time' knob (right) clockwise to 30min. Balancer will automatically turn on.
- c. Charge batteries one at a time Connect extensions to the leads of 1x TP Battery (called Battery A). Connect Battery A connectors to the Balancer's circuit board as shown in Figure 47. **[WARNING: NEVER short the battery leads as this is dangerous and could lead to bodily harm or damage. Keep positive and negative leads insulated from each other with electrical tape.]**



Figure 46. TP batteries and extension leads

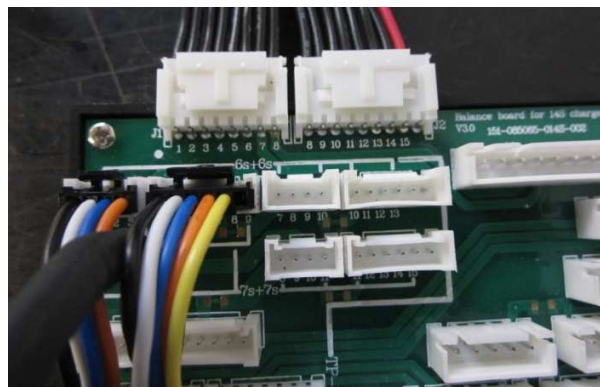


Figure 47. TP battery connection to balancer circuit board

- d. Plug in electrical leads of Battery A into Balancer as shown in Figure 48. Do not be alarmed by slight spark at positive lead. Charging configuration has already been programmed and stored (Configuration 01). Press and hold on to 'Enter' button on Balancer and charging will start automatically. Charge for 30–

40min until voltage for each cell of the Battery is 4.20V. [NOTE: Avoid leaving the battery to charge unattended for long periods of time. **WARNING:** NEVER overcharge the Battery as it is dangerous and could lead to bodily harm or damage.]



Figure 48. battery connected to balancer and charging

- e. Once battery has been fully charged, press 'Enter' to stop charging process and disconnect the battery leads followed by the Circuit Board Connectors.
- f. Repeat steps (2) to (5) for Battery **B**.
- g. Once charging is complete, turn the 'Rate' and 'Time' knobs counter clockwise to '0' to turn off the Battery Charger as well as the Balancer. [NOTE: Let Batteries cool down to room temperature before commencing experiment]

**Refer to TP manuals [8] for more information on battery charging or view the charging demonstration from link:*

<http://www.youtube.com/watch?v=5rL4vXjEtKc> [9]

2. Programming of Controller

- a. Connect Battery A and Battery B together in series as shown in the setup in Figure 49 below. Connect ONLY the negative lead of the combined batteries, leaving the lead slightly exposed. **WARNING:** NEVER short the battery leads

as this is dangerous and could lead to bodily harm or damage. Keep positive and negative leads insulated from each other with electrical tape.]



Figure 49. battery and controller connection

b. Turn on Laptop installed with “Scorpion ESC Programmer v1.2” and connect the Cable Link to the Laptop and Controller (Take note of the wire coloring when connecting the cable link to the Controller).

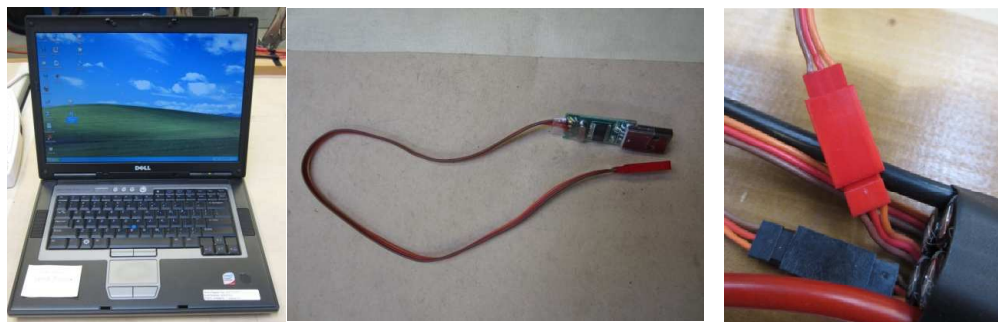


Figure 50. Laptop, cable link to controller and connection to connector

c. Turn on the Pulse Generator and make sure the pulse width is set to $1.20 \times 10^{-3}\text{s}$. This is below the start-up threshold of $1.27 \times 10^{-3}\text{s}$. Always make adjustments of the pulse width using the right two buttons circled in red in Figure 50. Also check that the A/TP and frequency settings are 2.5V and 48.64Hz, respectively.

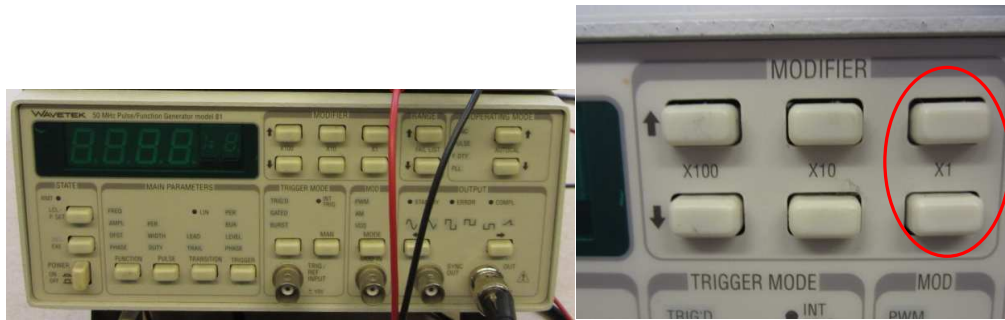


Figure 51. Pulse generator and pulse width adjustment buttons



Figure 52. Selection of waveform on pulse generator

- d. Open “Scorpion ESC Programmer v1.2” on the Laptop (from folder on desktop) and application will open as shown in Figure 53.

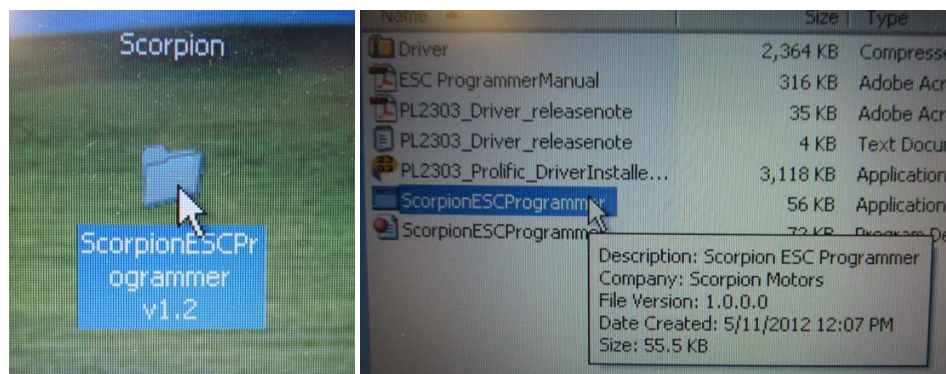


Figure 53. Location of “Scorpion ESC Programmer v1.2”

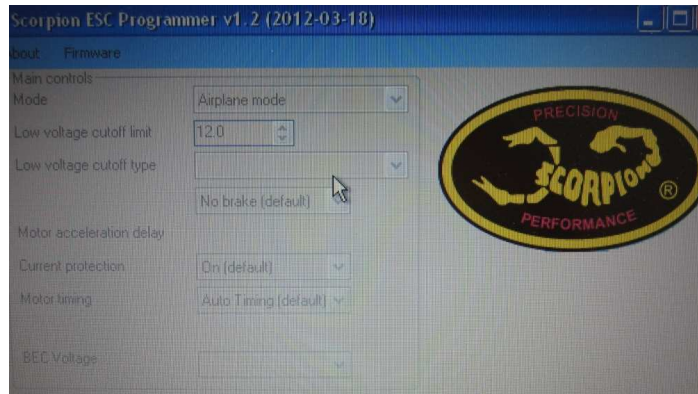


Figure 54. Opened “Scorpion ESC Programmer v1.2” application

- e. Select ‘Autodetect’ from ‘Select COM Port’ at the bottom-left corner of the program window.

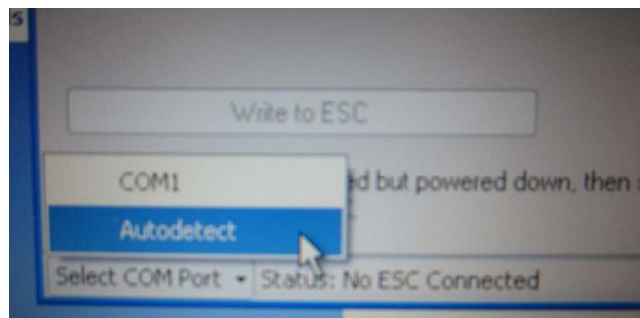


Figure 55. Location of COM port selection

- f. Connect the positive lead of the Battery to the Controller (watch out for spark) and the ‘Write to ESC’ button in the programmer will be selectable. Ensure that the settings are as shown in Figure 56. Click on ‘Write to ESC’ and programmer will start writing control algorithm into Controller.

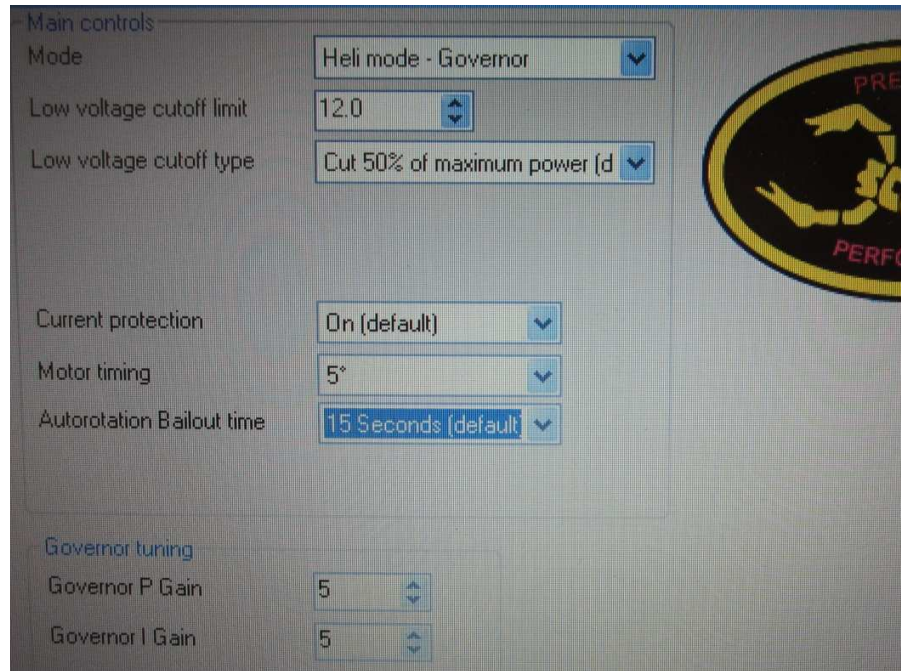


Figure 56. Control setting for controller

- g. Disconnect the positive lead of the Battery and then the Cable Link from Laptop and Controller.

3. CFF Test Operation

- a. Turn on the DC Power Supply and make sure voltage is around 5.00V.



Figure 57. DC power supply

- b. Select the waveform on the Pulse Generator as shown in Figure 58.

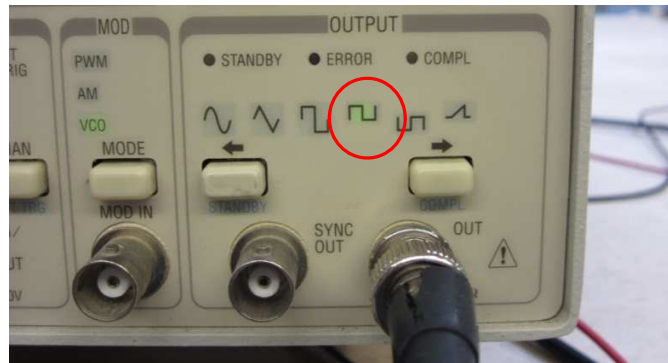


Figure 58. Selection of waveform on pulse generator

- c. Connect the positive lead of the Battery to the Controller, exposing part of the lead (for doing voltage measurements during the experiment). Do not be alarmed by the spark. The LED connected in the setup will beep once and then flash. This indicates that detection is successful. If a continuous “BEEP” is heard, disconnect the battery and connect again. **[WARNING: NEVER short the battery leads as this is dangerous and could lead to bodily harm or damage. Keep positive and negative leads insulated from each other with electrical tape.]**
- d. Increase the pulse width to $1.27 \times 10^{-3}\text{s}$ and the CFF will start rotating at the minimum speed. Make sure the Weighing scale is directly under the outlet of the CFF. Adjust the weights and record the thrust of the CFF in grams.

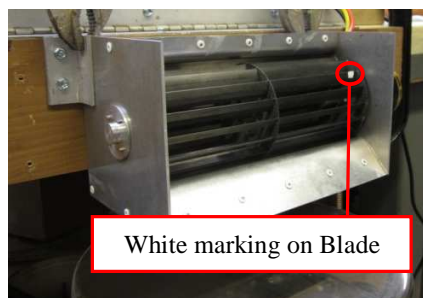


Figure 59. CFF in housing and white marking on blade

- e. Turn on the Stroboscope and face the flickering light towards the blades of the CFF. Adjust the central knob until the white marking on one of the blades of

the CFF is seen to be almost stationary. Read and record the rotational speed in RPM.



Figure 60. Stroboscope

- f. Repeat Steps (d) and (e) for different pulse widths. Do not conduct experiment continuously for more than 6min.
- g. Once 6min is up, stop the experiment and disconnect the Batteries. Measure the temperature of the Batteries, Controller and Motor and record using a thermostat.

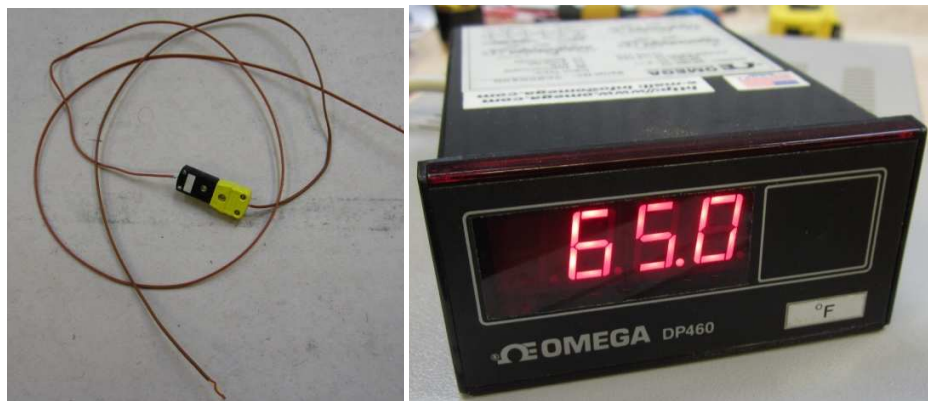


Figure 61. Thermostat

- h. Let the Batteries, Controller and Motor cool down to room temperature before continuing with test.

E. RESULTS OF VALIDATION

The results of the repeatability test using the exact setup as Delagrange and as described in section C showed that the thrust measurements were relatively close with an average variation of about 8.4%. However, the CFF lost control at speeds higher than 8,000 rpm.

Table 12. Thrust measurement comparison with Delagrange's records

DELAGRANGE'S TEST		REPEATABILITY TEST	
Rotational Speed Measurement	Thrust Measurement	Rotational Speed Measurement	Thrust Measurement
5,100 rpm	458g	5,150 rpm	503g (+9.8%)
5,600 rpm	548g	5,600 rpm	590g (+7.7%)
6,120 rpm	645g	6,300 rpm	723g (+12.1%)
7,120 rpm	861g	7,100 rpm	920g (+6.9%)
7,640 rpm	976g	7,600 rpm	1,060g (+8.6%)
7,980 rpm	1,065g	7,900 rpm	1,120g (+5.2)
8,380 rpm	1,161g	8,400 rpm	1,260g (+8.5%)
-	-	8,800 rpm	1,400g

Attempts to troubleshoot and rectify the loss of control failed with the above mentioned setup. However, upon changing the Controller from a programmed chip to one adjusted via a rheostat as well as making use of one single battery (instead of two), the CFF was able to run at rotational speeds up to 8,800 rpm without any trouble.

THIS PAGE INTENTIONALLY LEFT BLANK

APPENDIX D. DRAGONPLATE CFF EXPERIMENT PROCEDURE

A. PURPOSE OF EXPERIMENTAL PROCEDURE

The purpose of this section is to document the exact procedures to operate the DragonPlate CFF experiment in order to facilitate future continuations of this research. The high power density batteries used in the setup also play a part as it affects safety when conducting the experiment. Therefore, it is important for proper documentation to minimize any potential safety hazards.

B. EQUIPMENT LIST

- 2x 78 mm Diameter DragonPlate Cross-Flow Fan (in aluminum housing)
- 1x Metal Sliding Fixture
- 2x Clamps
- 2x Controller
- 2x Rheostat
- 1x Agilent DC Power Supply
- 1x Thermostat
- 1x Giant Weighing Scale with Zeroed Plate
- 1x Stroboscope
- 1x Voltmeter
- 4x ThunderPower (TP) 65C, 6-Cell LiPo Battery (G6 Pro Power) – Battery **A**, **B**, **C** and **D**
- 1x ThunderPower (TP) 1340C Balancer
- 1x All State Battery Charger
- Electrical Wires

C. EXPERIMENTAL SETUP

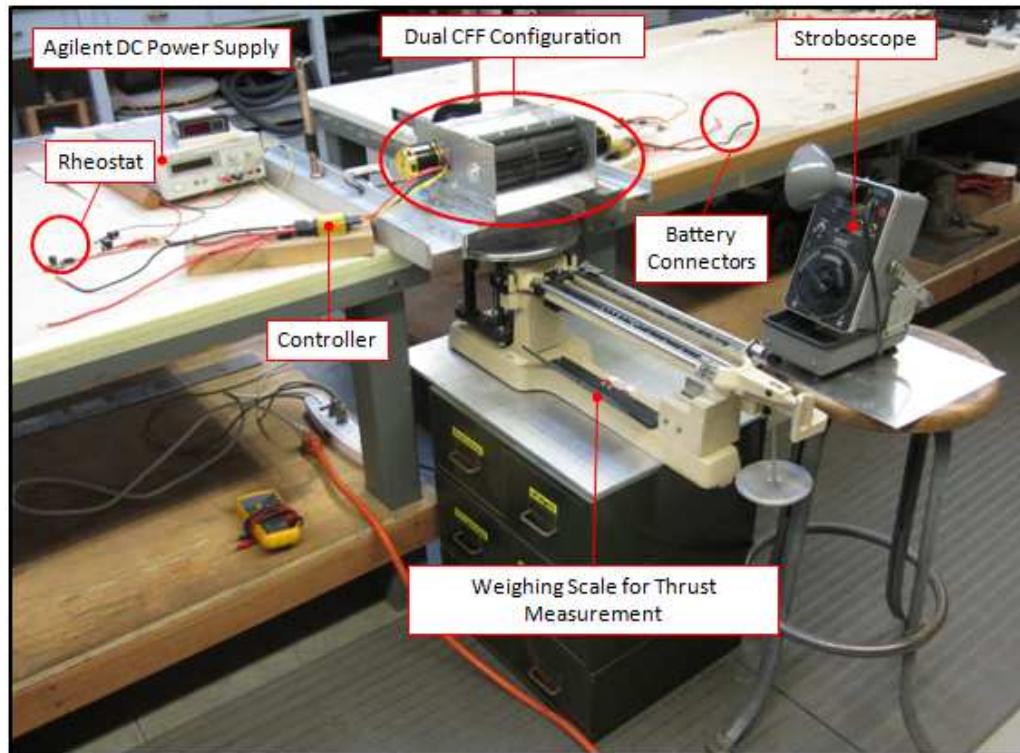


Figure 62. Overall DragonPlate CFF experimental setup and major components

D. PROCEDURE

1. Battery Charging

- a. Connect TP1340C Balancer to ALL STATE Battery Charger.



Figure 63. TP1340C balancer and ALL STATE battery charger

- b. Plug Battery Charger into power socket. Turn the 'Rate' knob (left) clockwise to '3' and the 'Time' knob (right) clockwise to 30min. Balancer will automatically turn on.
- c. Charge batteries one at a time Connect extensions to the leads of 1x TP Battery (called Battery A). Connect Battery A connectors to the Balancer's circuit board as shown in Figure 65. **[WARNING: NEVER short the battery leads as this is dangerous and could lead to bodily harm or damage. Keep positive and negative leads insulated from each other with electrical tape.]**



Figure 64. TP batteries and extension leads

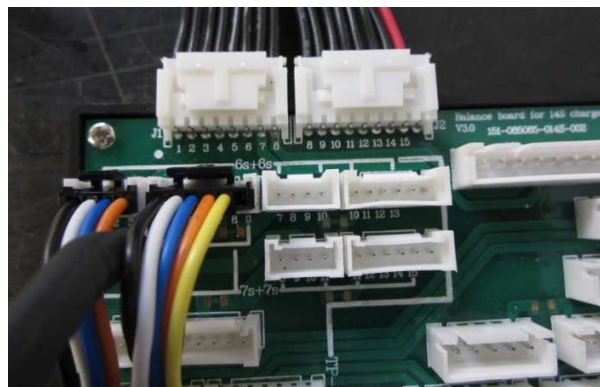


Figure 65. TP battery connection to balancer circuit board

- d. Plug in electrical leads of Battery A into Balancer as shown in Figure 66. Do not be alarmed by slight spark at positive lead. Charging configuration has already been programmed and stored (Configuration 01). Press and hold on to 'Enter' button on Balancer and charging will start automatically. Charge for 30–

40min until voltage for each cell of the Battery is 4.20V. [NOTE: Avoid leaving the battery to charge unattended for long periods of time. **WARNING:** NEVER overcharge the Battery as it is dangerous and could lead to bodily harm or damage. Also be careful not to plug the leads into the wrong ports. Positive leads must only be connected to positive ports and negative leads to negative ports. Failure to do so could lead to bodily harm or damage.]



Figure 66. battery connected to balancer and charging

- e. Once battery has been fully charged, press 'Enter' to stop charging process and disconnect the battery leads followed by the Circuit Board Connectors.
- f. Repeat steps (2) to (5) for Battery **B**, **C** and **D**.
- g. Once charging is complete, turn the 'Rate' and 'Time' knobs counter clockwise to '0' to turn off the Battery Charger as well as the Balancer. [NOTE: Let Batteries cool down to room temperature before commencing experiment]

**Refer to TP manuals [8] for more information on battery charging or view the charging demonstration from link:*

<http://www.youtube.com/watch?v=5rL4vXjEtKc> [9]

2. CFF Test Operation

- a. Turn on the DC Power Supply and make sure voltage is around 5.00V.



Figure 67. DC power supply

- b. Place the flat plate on the weighing scale and ensure that the scale has been zeroed for accurate thrust measurement.
- c. Turn the knobs on the rheostats clockwise until they reach the end on the right. An example can be seen from Figure 68 as shown below.

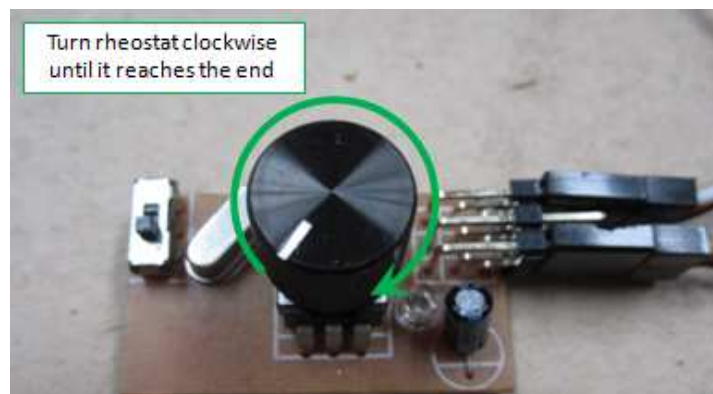


Figure 68. Pre-setting rheostat before connecting battery

- d. Connect Battery A and Battery B to CFF 1 and CFF 2, respectively. Connect **ONLY** the negative leads of the batteries first, leaving the leads slightly exposed (for doing voltage measurements during the experiment). Thereafter, connect the positive leads, also leaving the leads slightly exposed (for doing voltage measurements during the experiment). Do not be alarmed by the spark. A single beep will sound from the LED. [**WARNING:** NEVER short the battery leads as this is dangerous and could lead to bodily harm or damage. Keep positive and negative leads insulated from each other with electrical tape.]

CFF 2 Subsystem Connection

3. LED will beep once

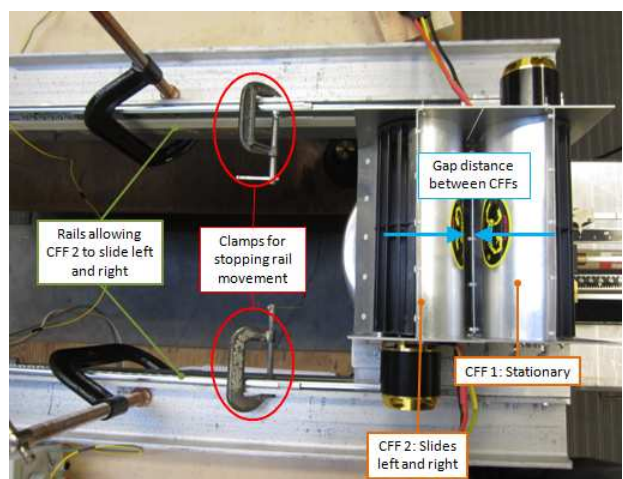
4. Turn rheostat knob counter-clockwise until it reaches the end

5. LED will beep twice

1. Connect negative lead of battery A to negative lead of controller

2. Connect positive lead of battery A to positive lead of controller

- f. Using the voltmeter, record the voltage of the batteries.
- g. Adjust the gap size between CFF 1 and CFF 2 by unclamping the rails and sliding CFF 2 away/towards CFF 1. Measure the gap between the two CFFs to ensure it is the correct gap size. Clamp the rails to prevent unwanted movement.



78

- h. Turn on the Stroboscope, with the frequency preset at the required rotational speed (e.g., 3,000 rpm). Face the flickering light towards the blades of the CFF 2 first.



Figure 71. Stroboscope

- i. Adjust the rheostat knob until the pre-painted white marking on one of the blades of the CFF is seen to be stationary or almost stationary. This indicates that the CFF is rotating at the required rotational speed.

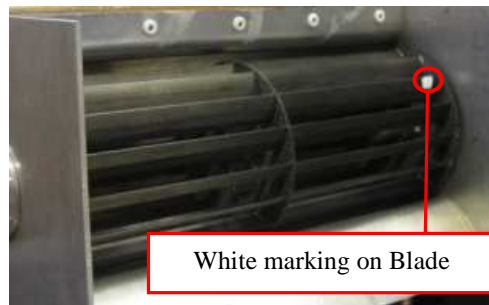


Figure 72. CFF in housing and white marking on blade

- j. Repeat Steps (h) and (i) for CFF 1.
- k. Adjust the weights on the weighing scale to determine the combined thrust output of CFF 1 and CFF 2. Record the thrust measured.

- l. Turn the rheostat knobs counter-clockwise until the end to stop the CFF rotations.
- m. Use a voltmeter and thermostat to check the voltage of the batteries and temperature of the motors/batteries/controllers, respectively. Stop the experiment if the temperatures measured exceed 150°F and allow experimental setup to cool down before continuing.

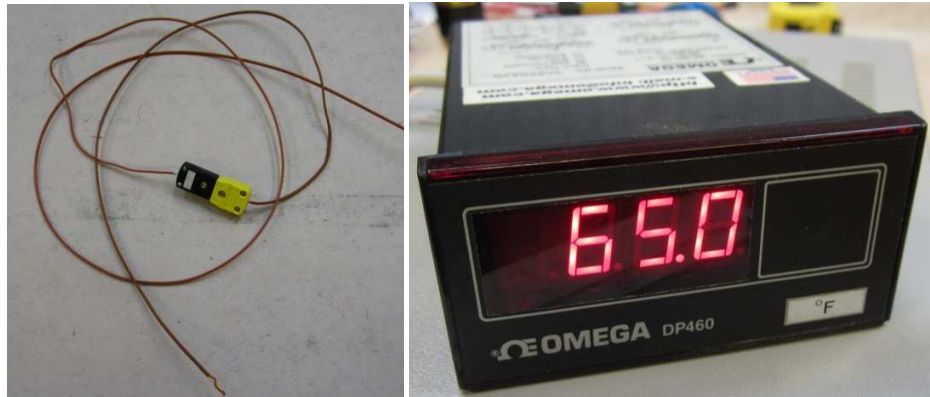


Figure 73. Thermostat

- n. Repeat Steps (f) to (m) for different rotational speeds and gap sizes. Stop the experiment once the voltage of the batteries drop to 21.00V or below as the batteries will have insufficient charge to power the CFFs.
- o. Recharge the batteries or use spare batteries (already fully charged) before continuing the experiment. Charging time per battery takes approximately 1hr 30min to 2hr to charge from 21.00V to 25.20V (full charge).

APPENDIX E. DRAGONPLATE CFF SIMULATION RESULTS

A. TORQUE MONITOR AND THRUST PLOTS

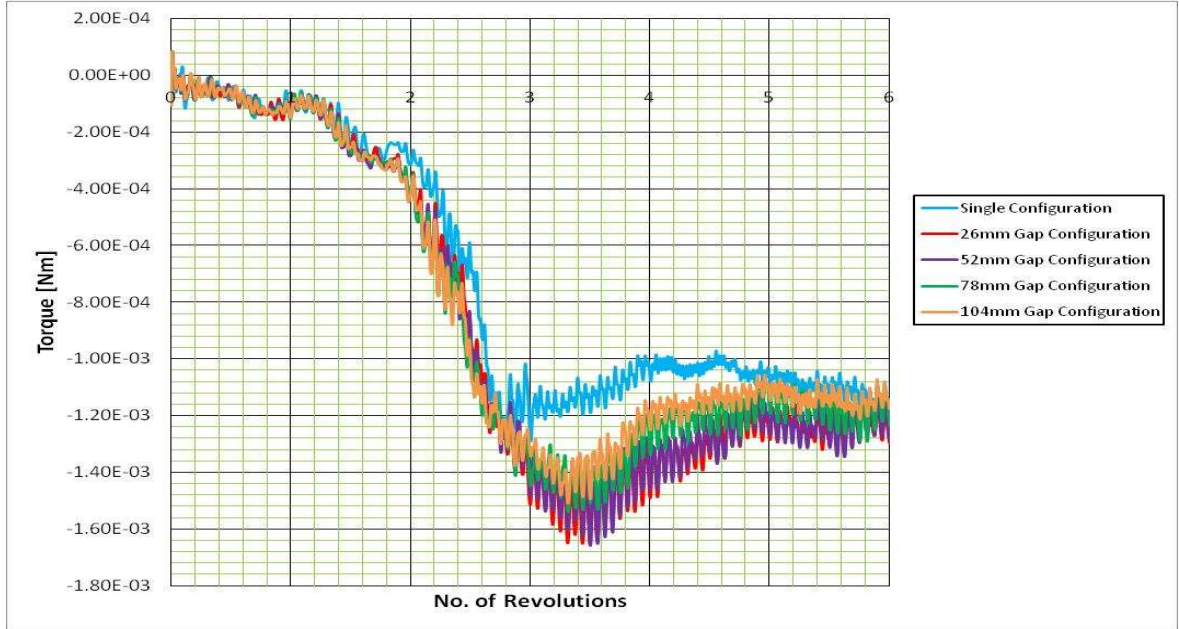


Figure 74. Plot of torque versus no. of revolutions at 5,000 rpm

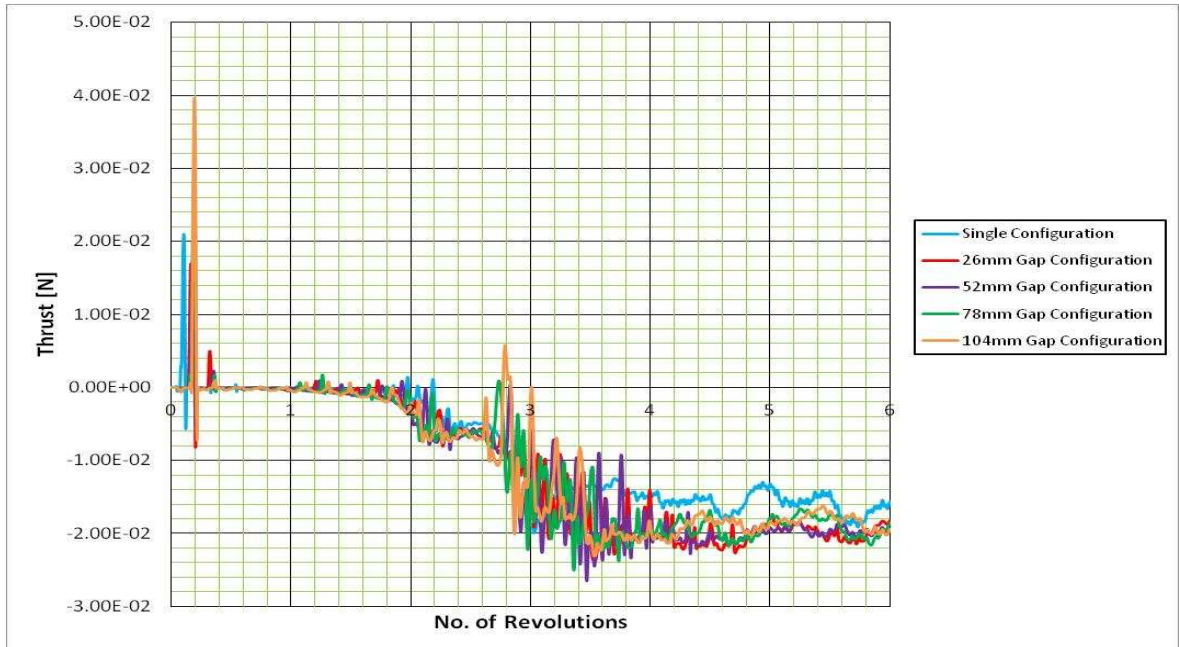


Figure 75. Plot of thrust versus no. of revolutions at 5,000 rpm

B. VELOCITY CONTOUR, STREAMLINE AND VECTOR PLOTS

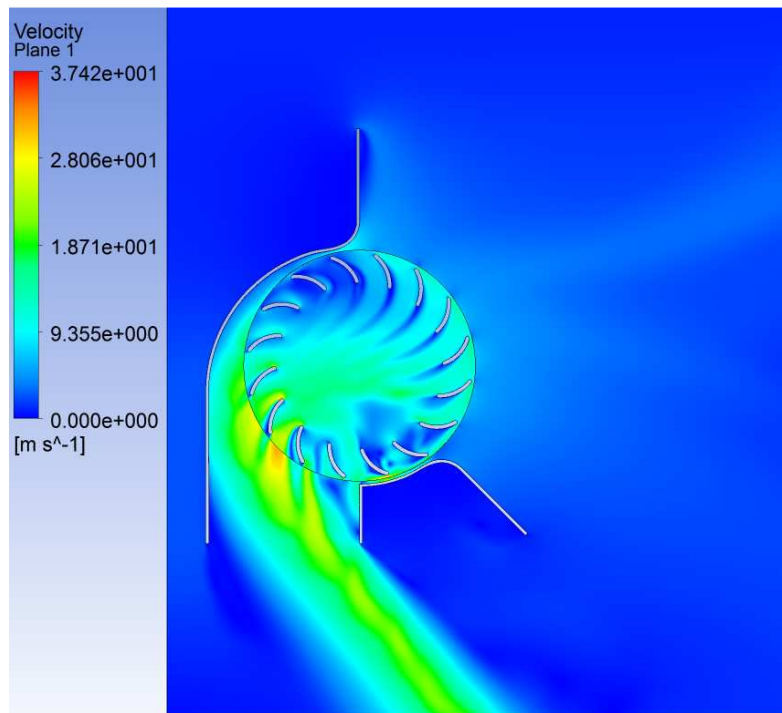


Figure 76. Velocity contour for single CFF configuration at 3,000 rpm

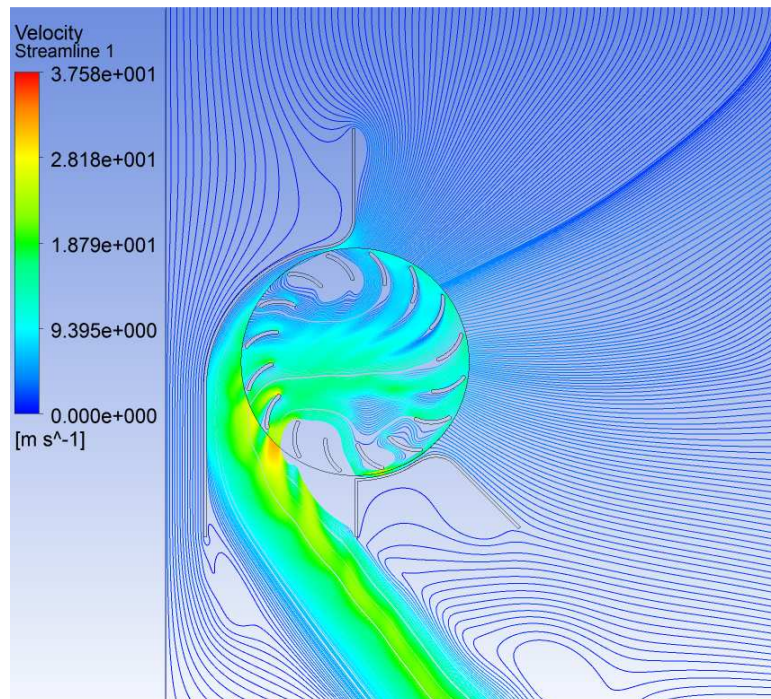


Figure 77. Velocity streamline for single CFF configuration at 3,000 rpm

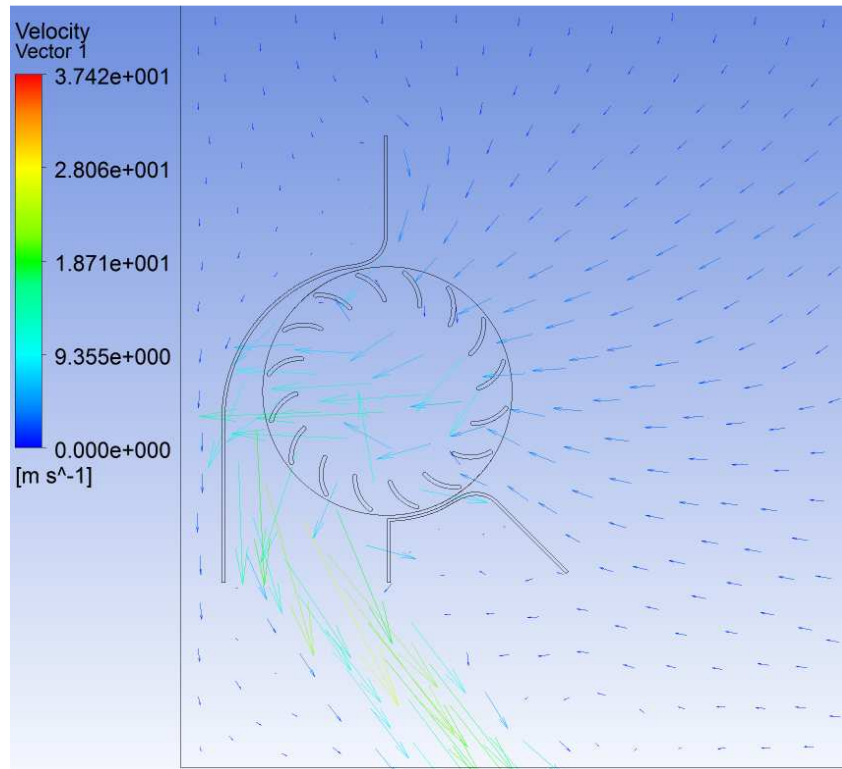


Figure 78. Velocity vector for single CFF configuration at 3,000 rpm

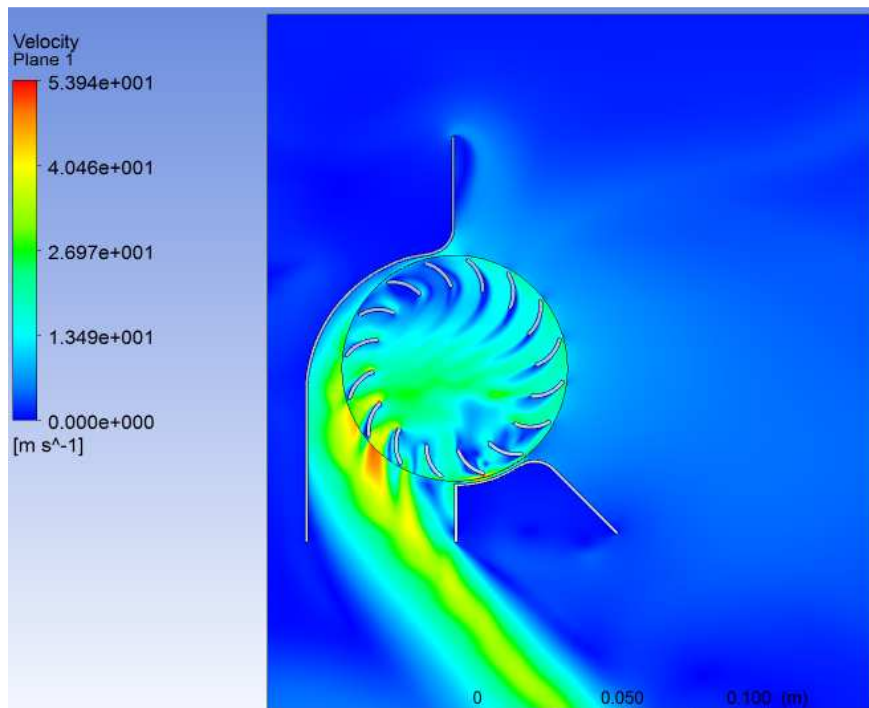


Figure 79. Velocity contour for single CFF configuration at 5,000 rpm

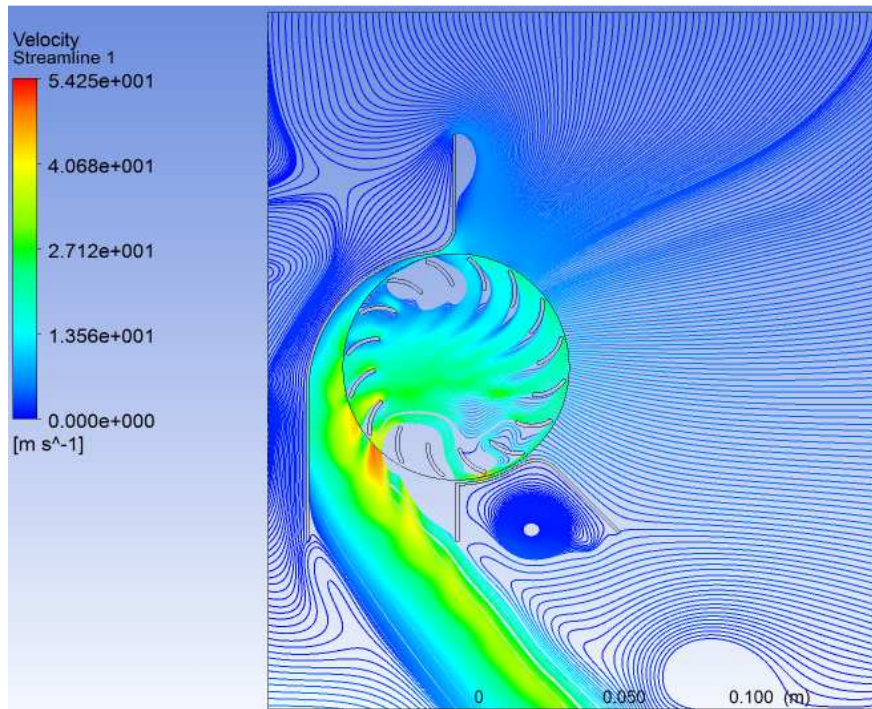


Figure 80. Velocity streamline for single CFF configuration at 5,000 rpm

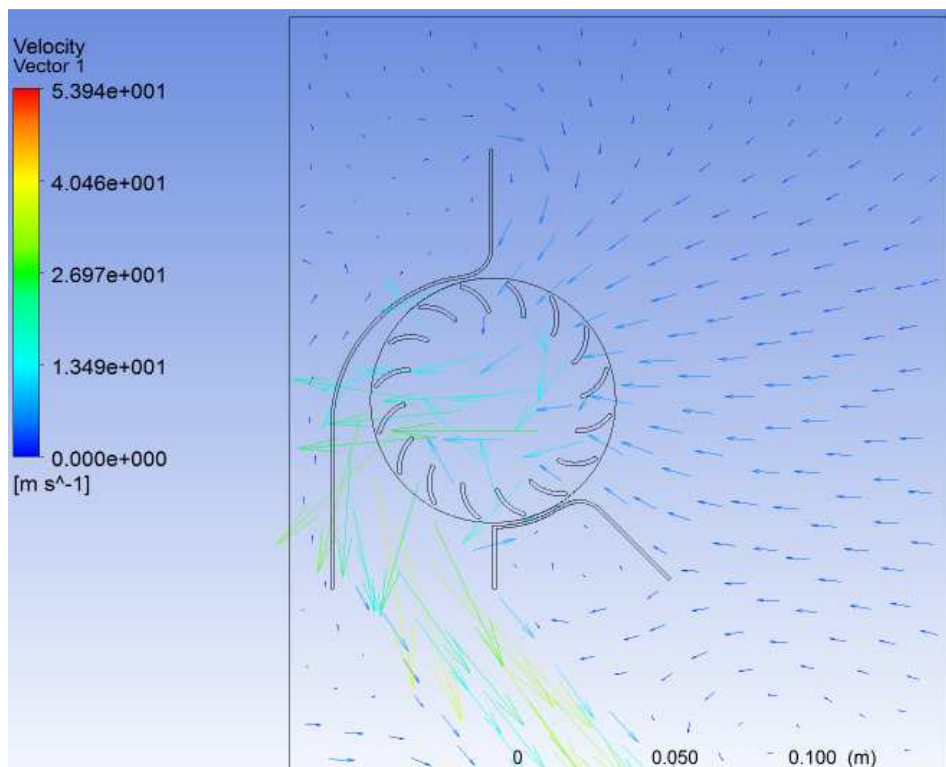


Figure 81. Velocity vector for single CFF configuration at 5,000 rpm

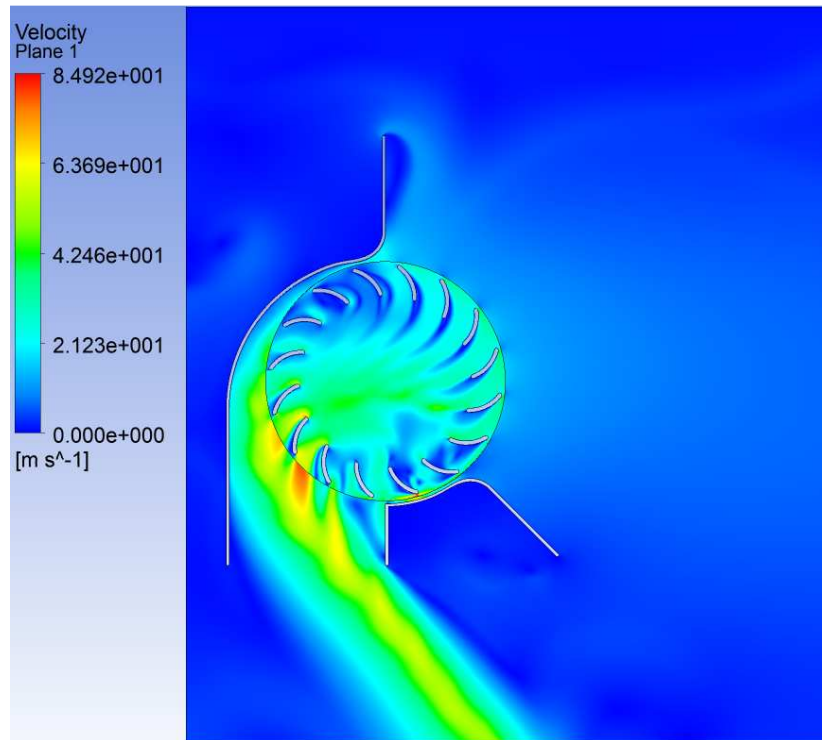


Figure 82. Velocity contour for single CFF configuration at 8,000 rpm

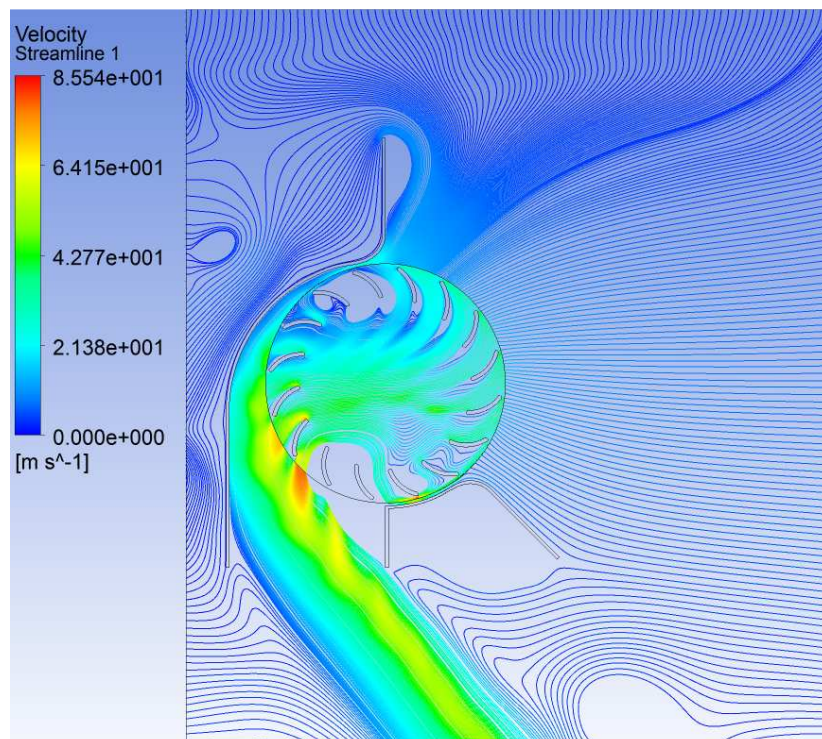


Figure 83. Velocity streamline for single CFF configuration at 8,000 rpm

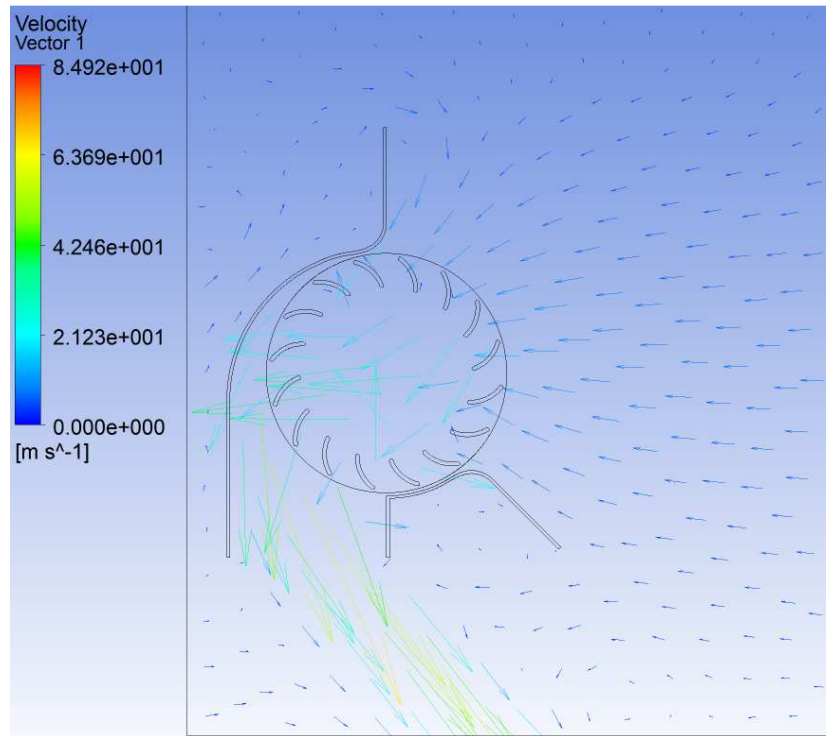


Figure 84. Velocity vector for single CFF configuration at 8,000 rpm

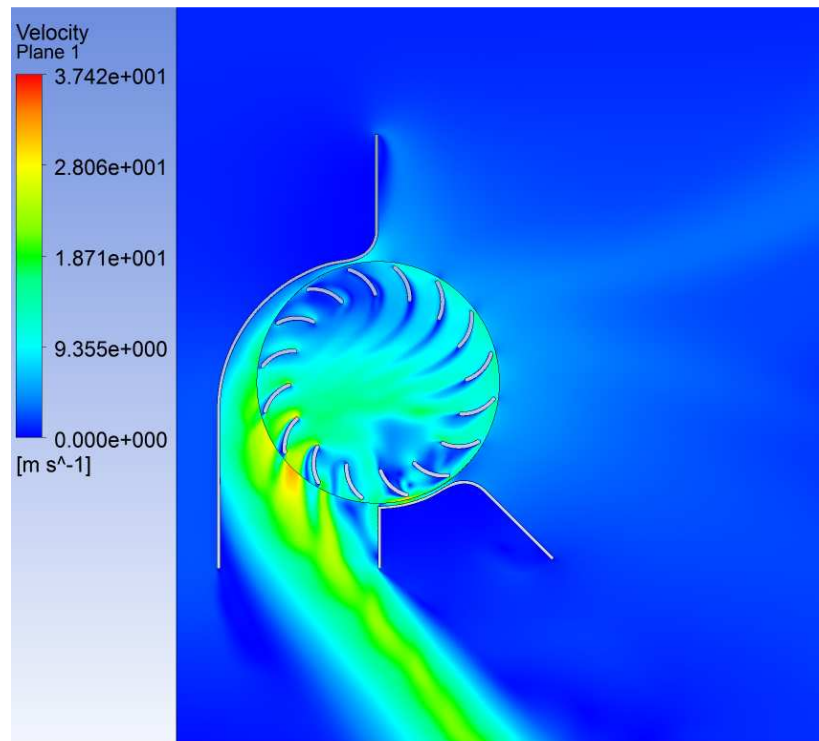


Figure 85. Velocity contour for 26 mm gap CFF configuration at 3,000 rpm

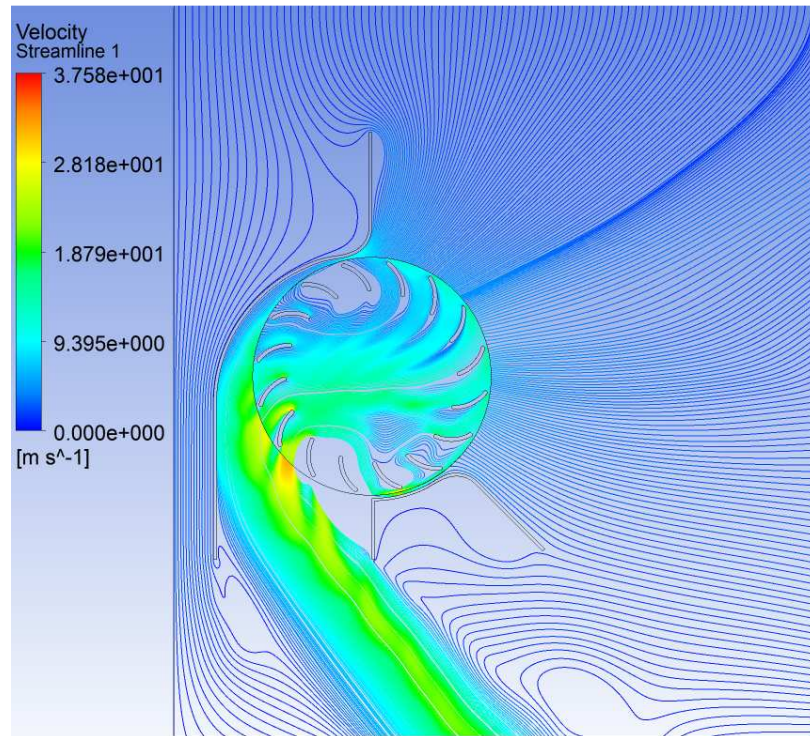


Figure 86. Velocity streamline for 26 mm gap CFF configuration at 3,000 rpm

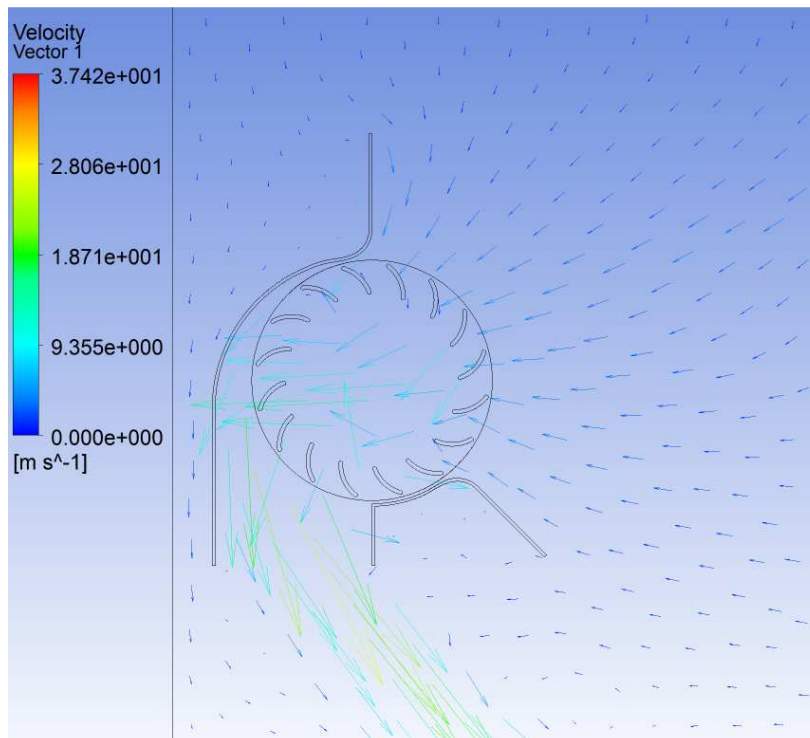


Figure 87. Velocity vector for 26 mm gap CFF configuration at 3,000 rpm

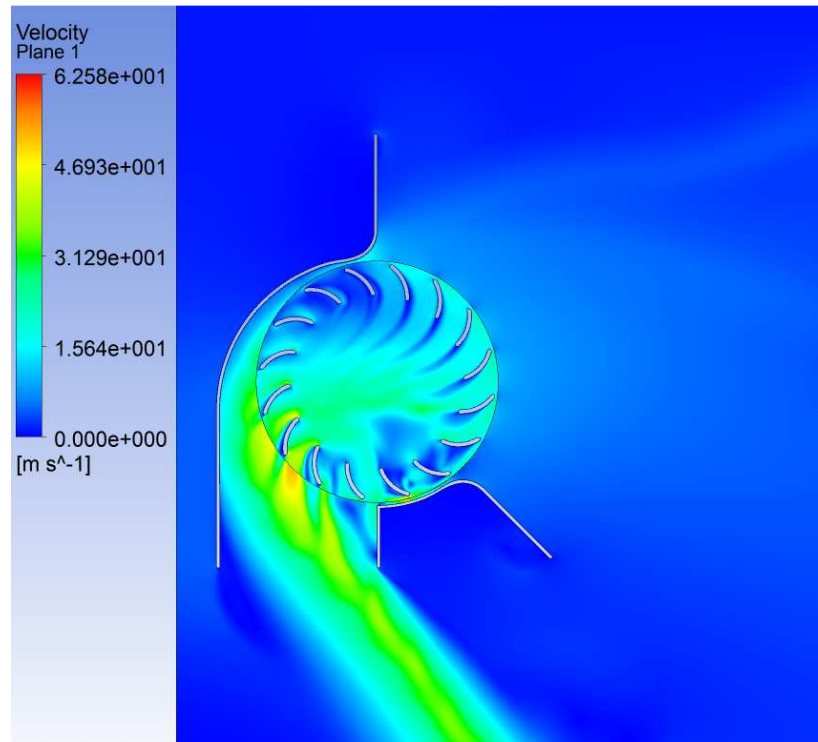


Figure 88. Velocity contour for 26 mm gap CFF configuration at 5,000 rpm

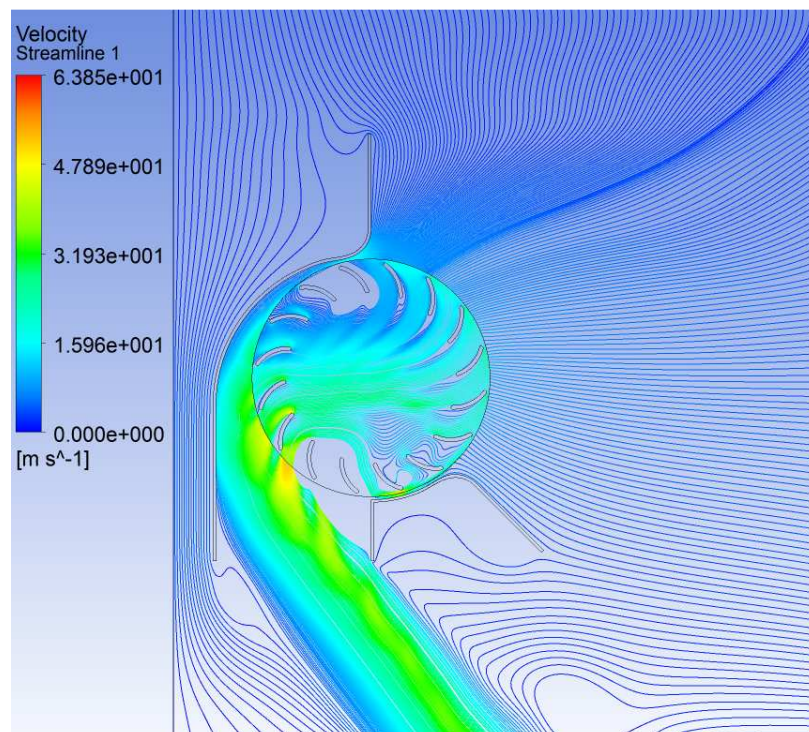


Figure 89. Velocity streamline for 26 mm gap CFF configuration at 5,000 rpm

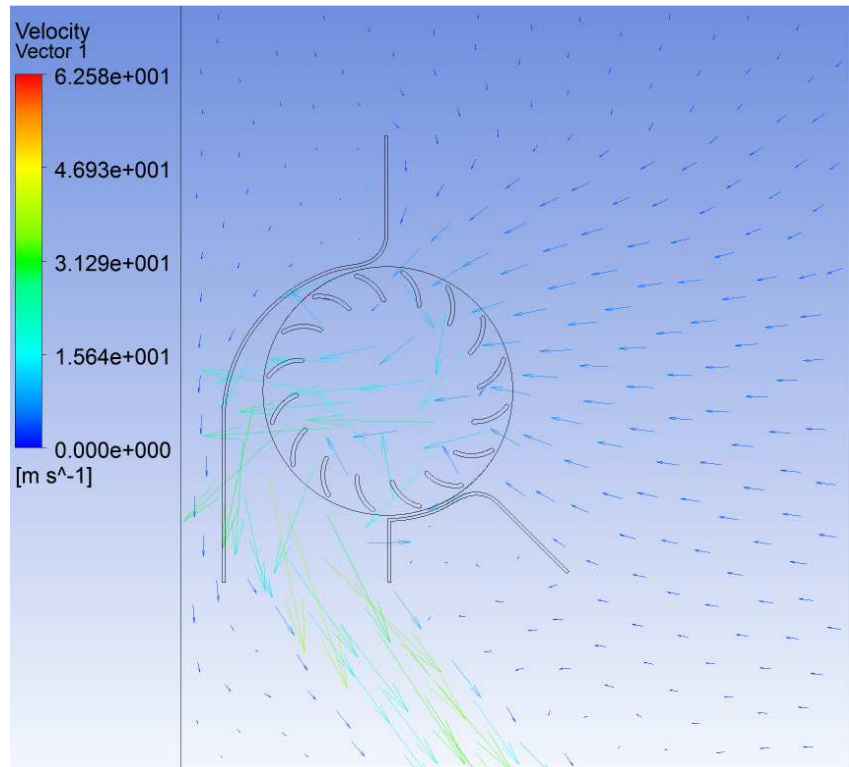


Figure 90. Velocity vector for 26 mm gap CFF configuration at 5,000 rpm

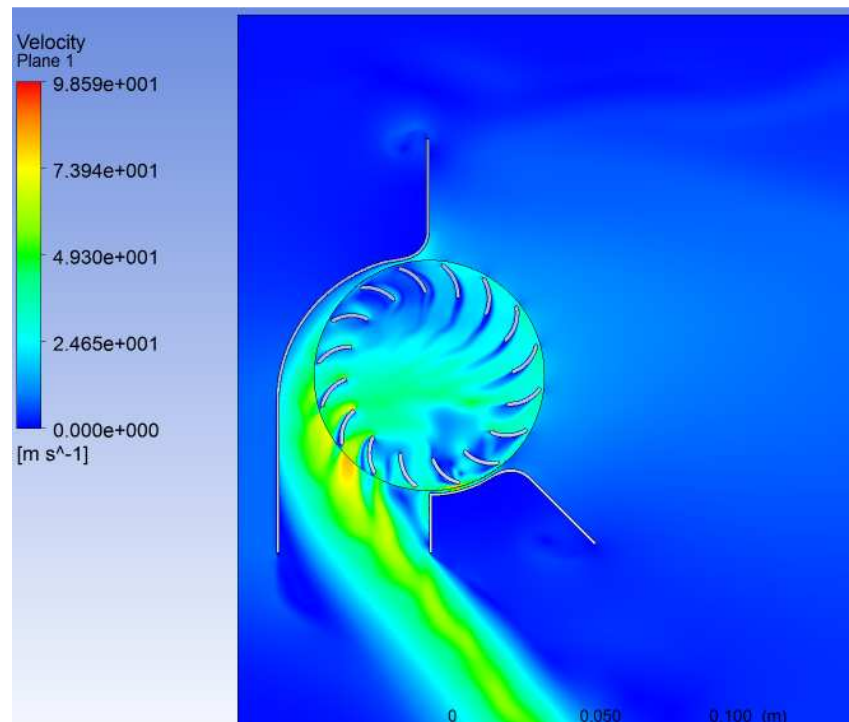


Figure 91. Velocity contour for 26 mm gap CFF configuration at 8,000 rpm

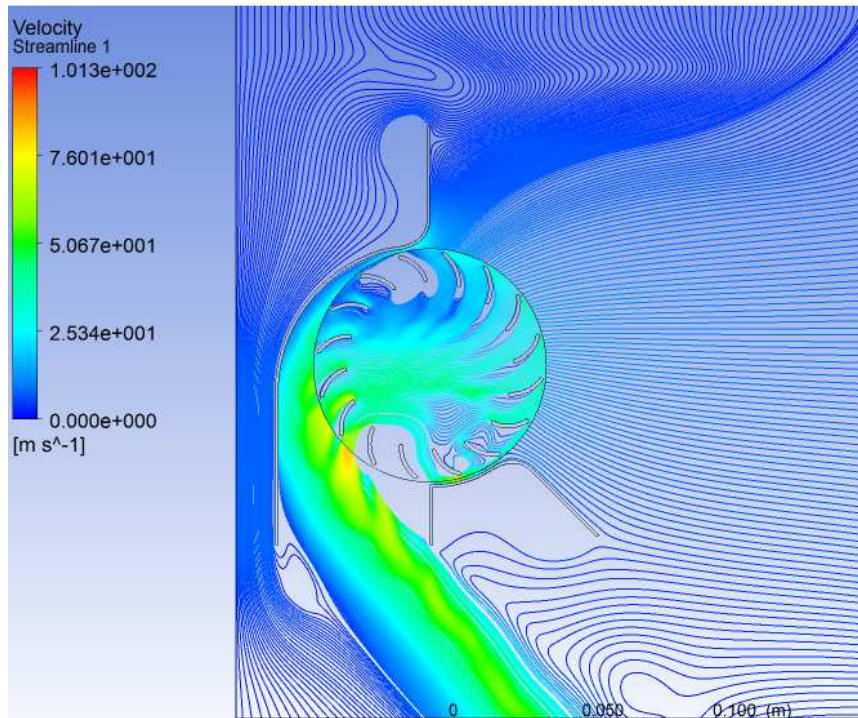


Figure 92. Velocity streamline for 26 mm gap CFF configuration at 8,000 rpm

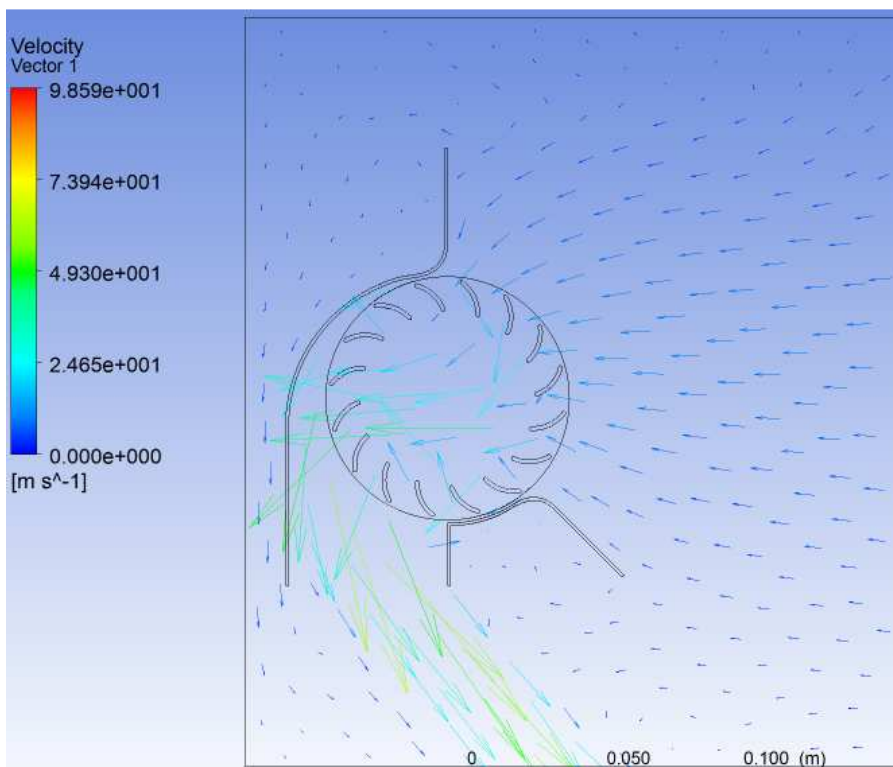


Figure 93. Velocity vector for 26 mm gap CFF configuration at 8,000 rpm

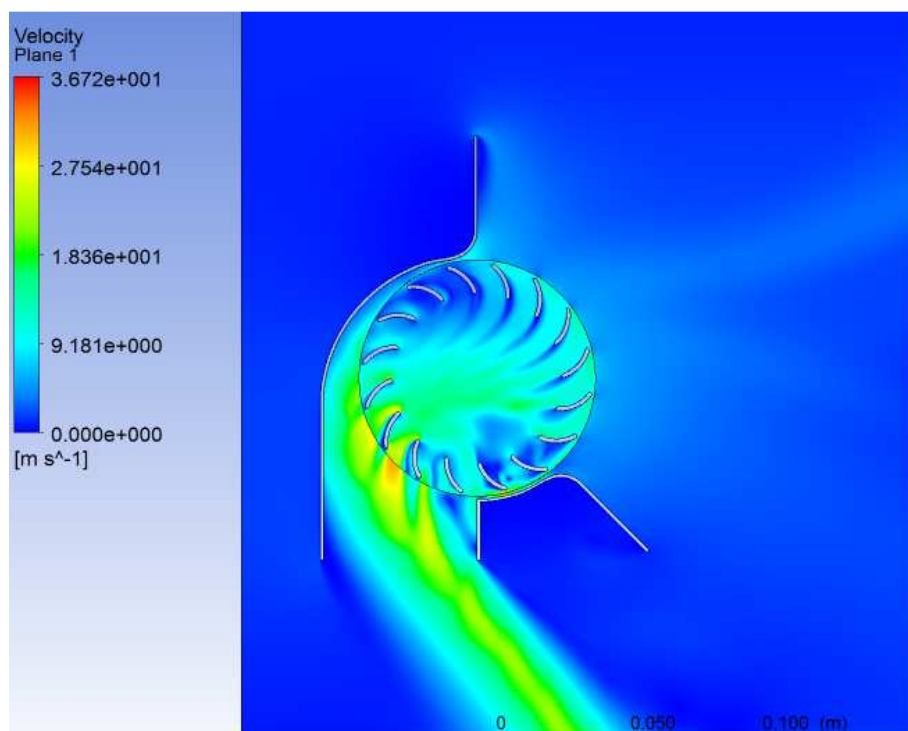


Figure 94. Velocity contour for 52 mm gap CFF configuration at 3,000 rpm

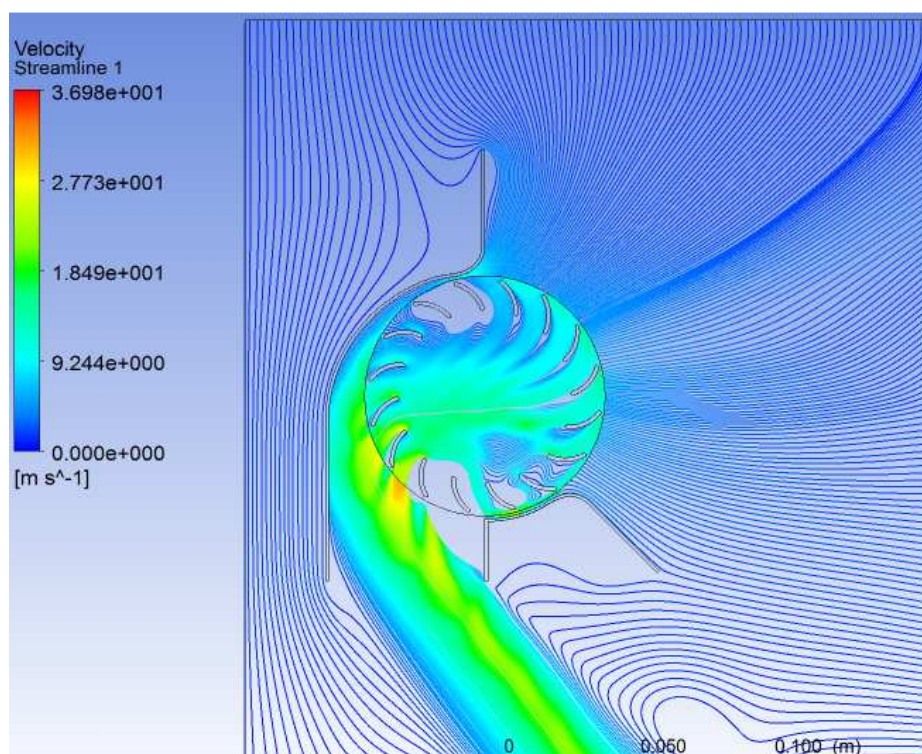


Figure 95. Velocity streamline for 52 mm gap CFF configuration at 3,000 rpm

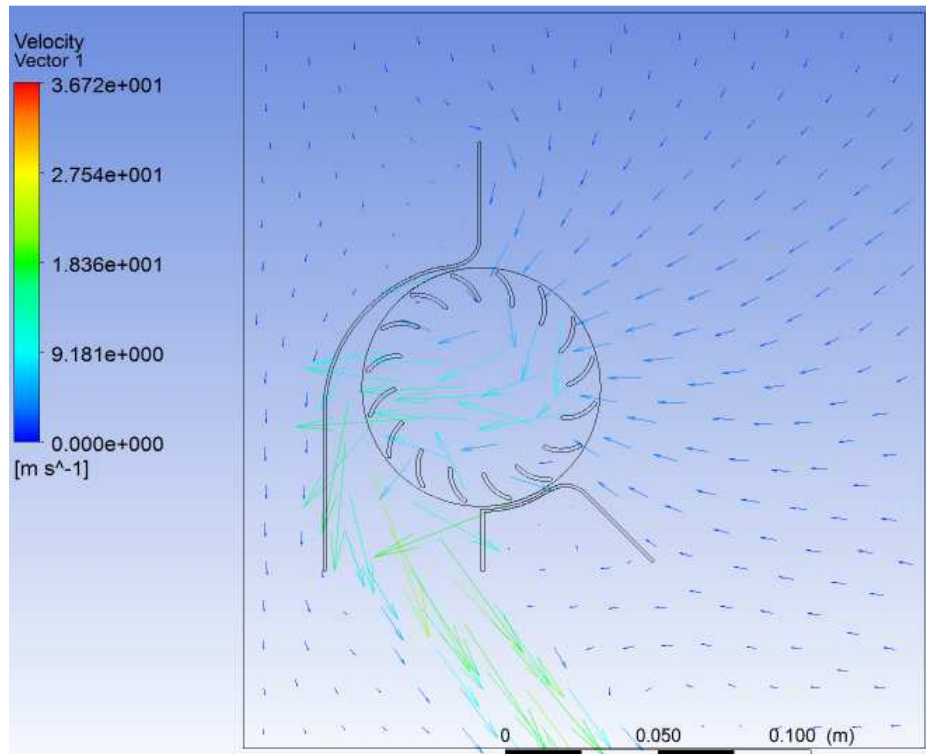


Figure 96. Velocity vector for 52 mm gap CFF configuration at 3,000 rpm

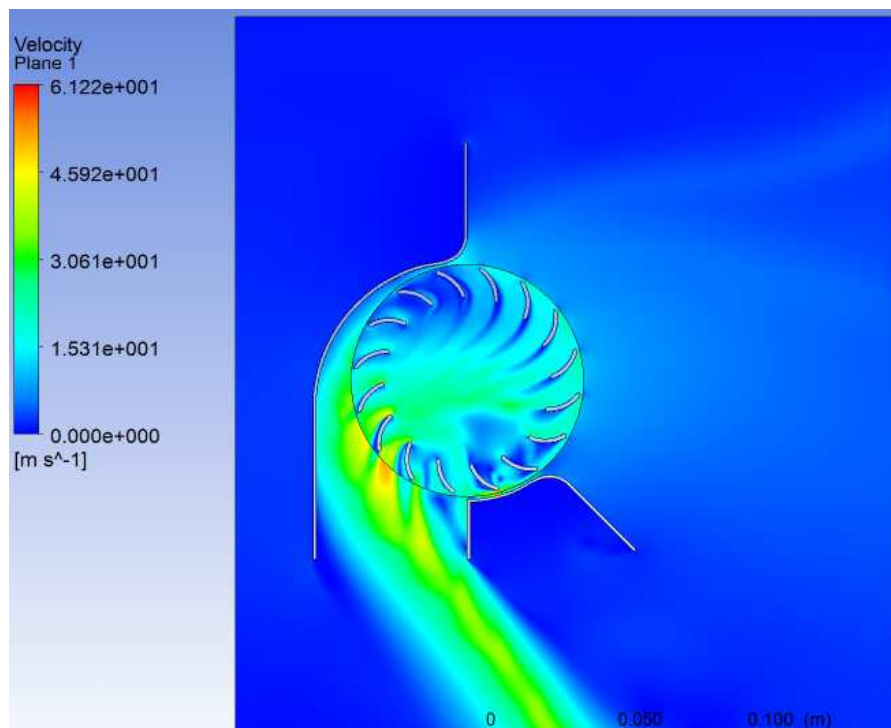


Figure 97. Velocity contour for 52 mm gap CFF configuration at 5,000 rpm

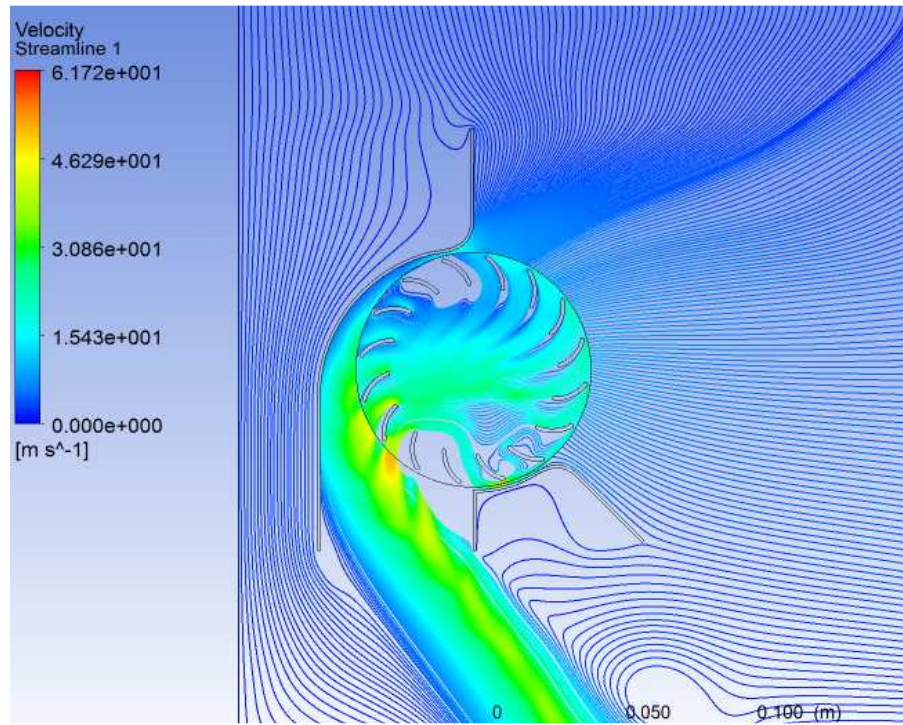


Figure 98. Velocity streamline for 52 mm gap CFF configuration at 5,000 rpm

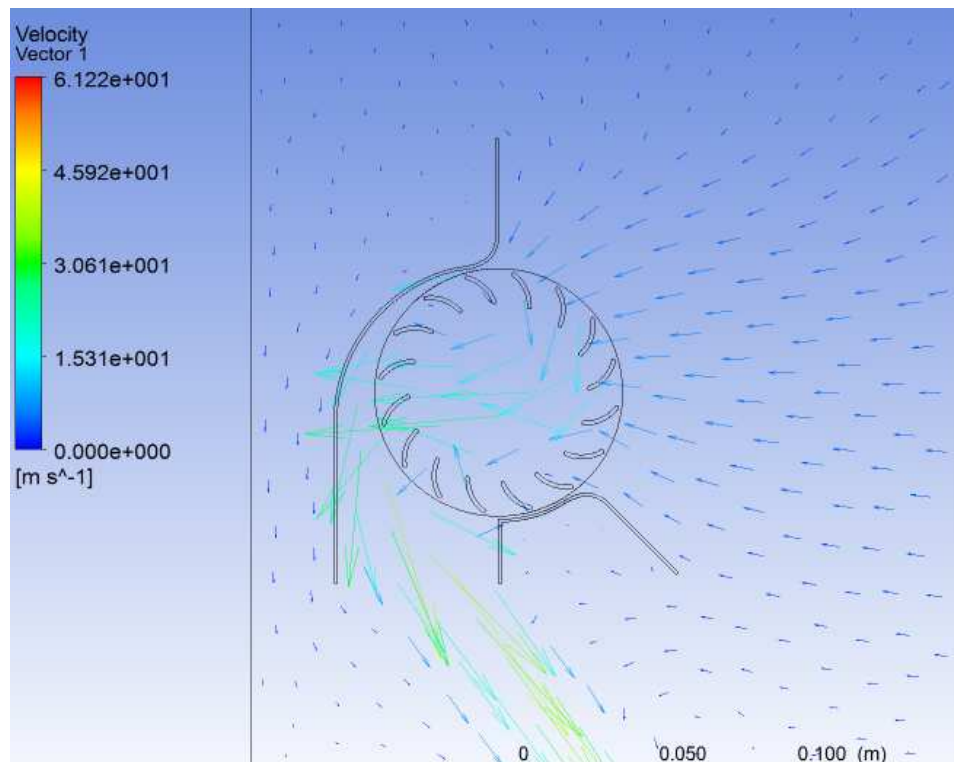


Figure 99. Velocity vector for 52 mm gap CFF configuration at 5,000 rpm

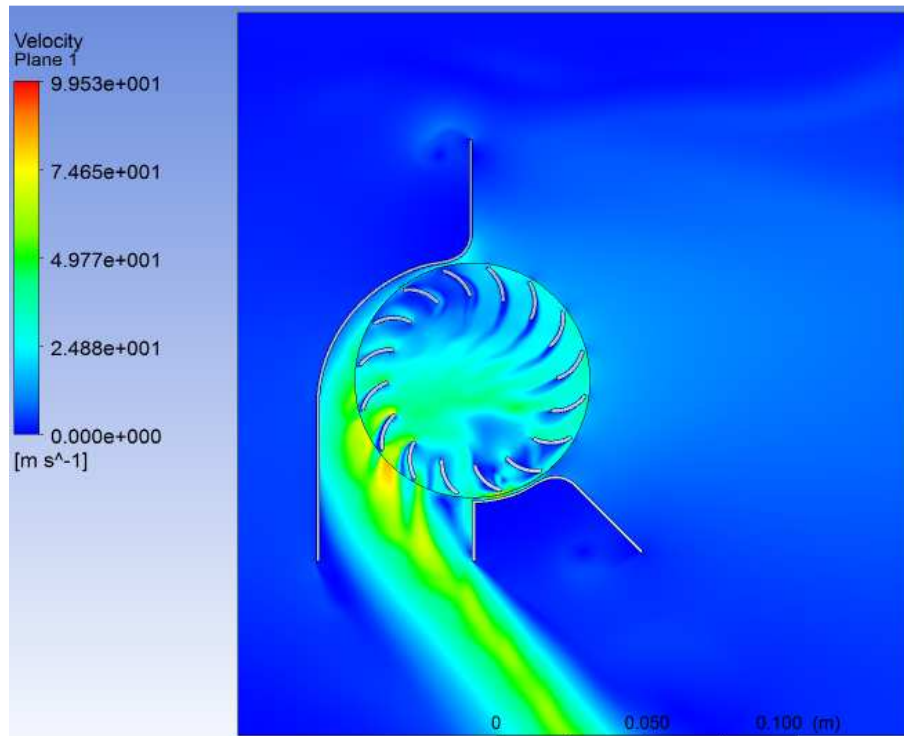


Figure 100. Velocity contour for 52 mm gap CFF configuration at 8,000 rpm

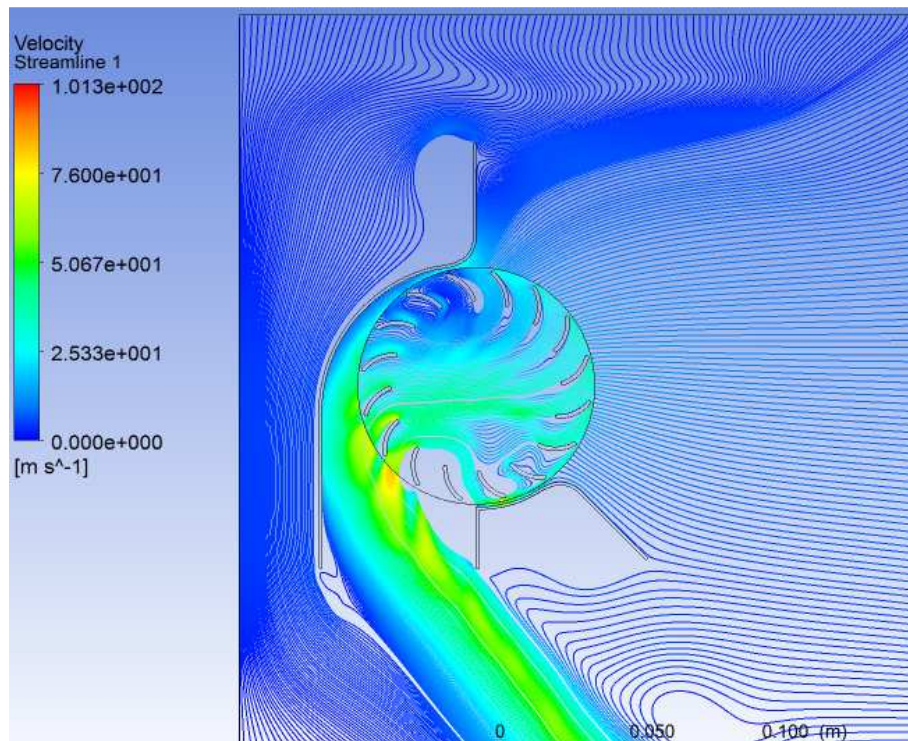


Figure 101. Velocity streamline for 52 mm gap CFF configuration at 8,000 rpm

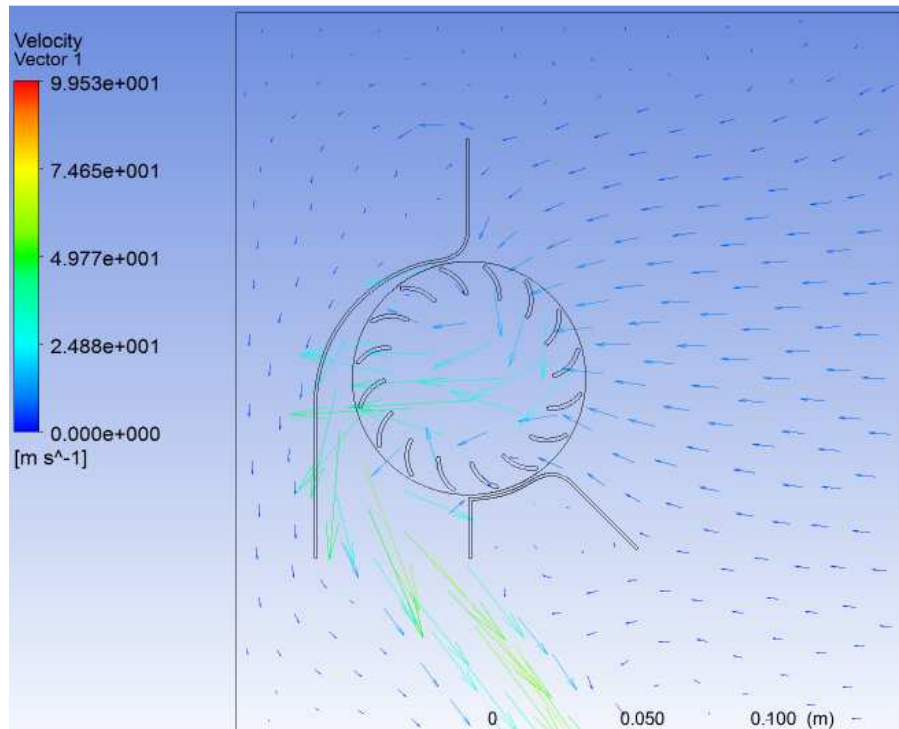


Figure 102. Velocity vector for 52 mm gap CFF configuration at 8,000 rpm

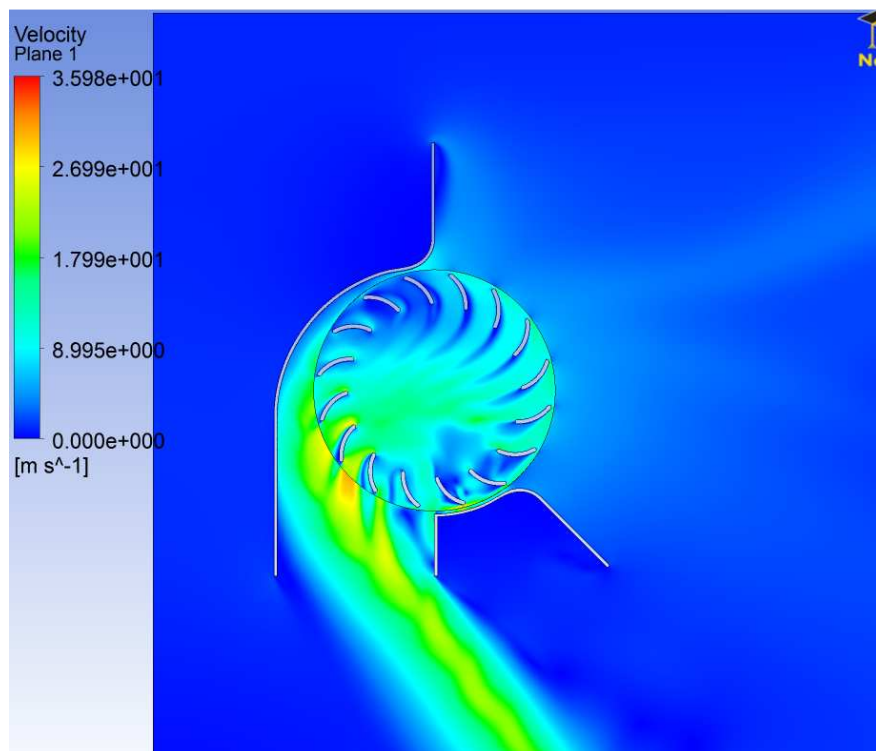


Figure 103. Velocity contour for 78 mm gap CFF configuration at 3,000 rpm

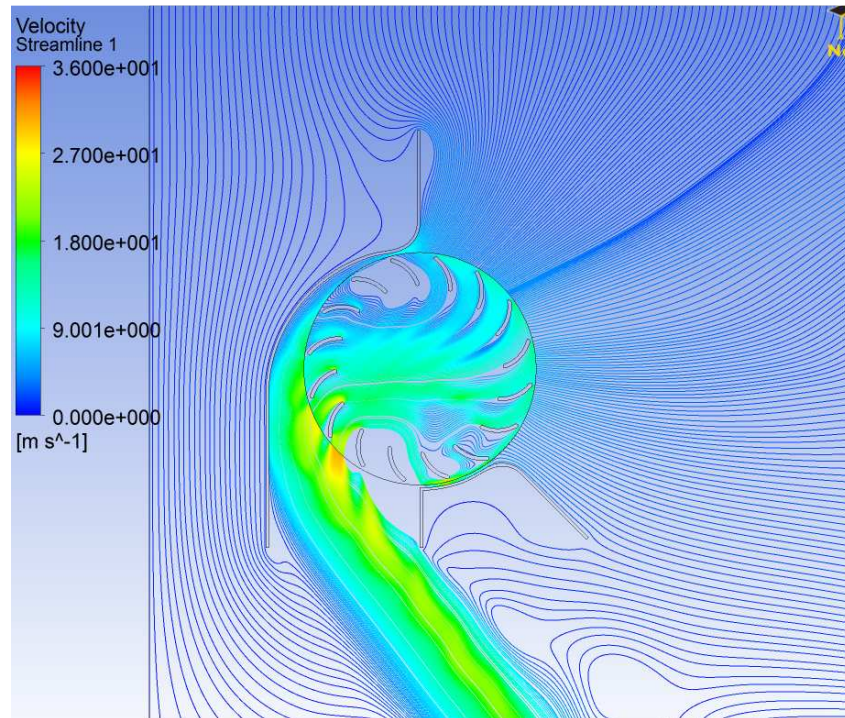


Figure 104. Velocity streamline for 78 mm gap CFF configuration at 3,000 rpm

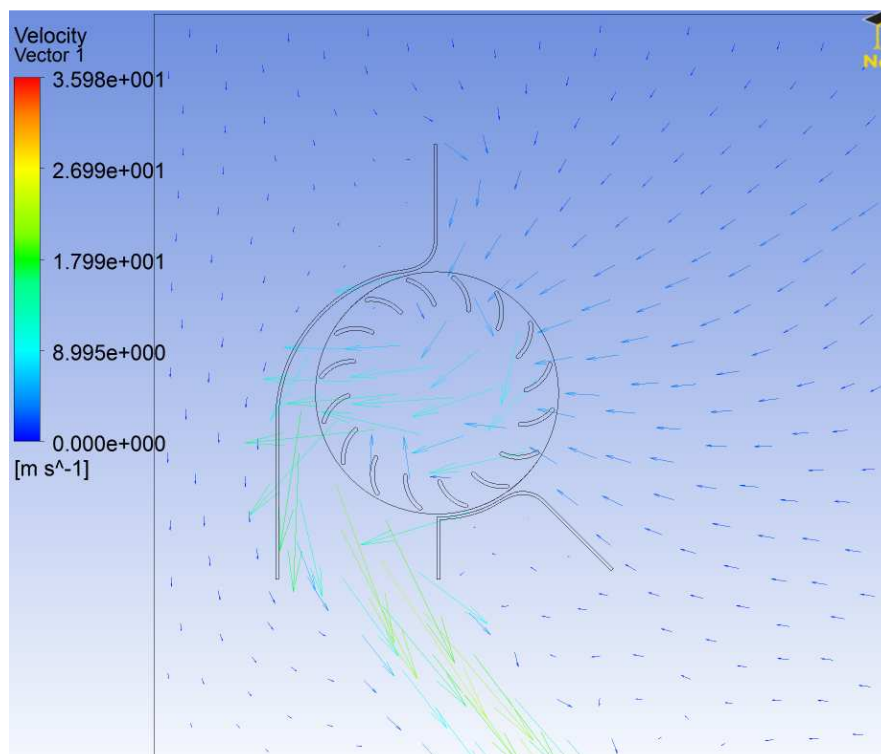


Figure 105. Velocity vector for 78 mm gap CFF configuration at 3,000 rpm

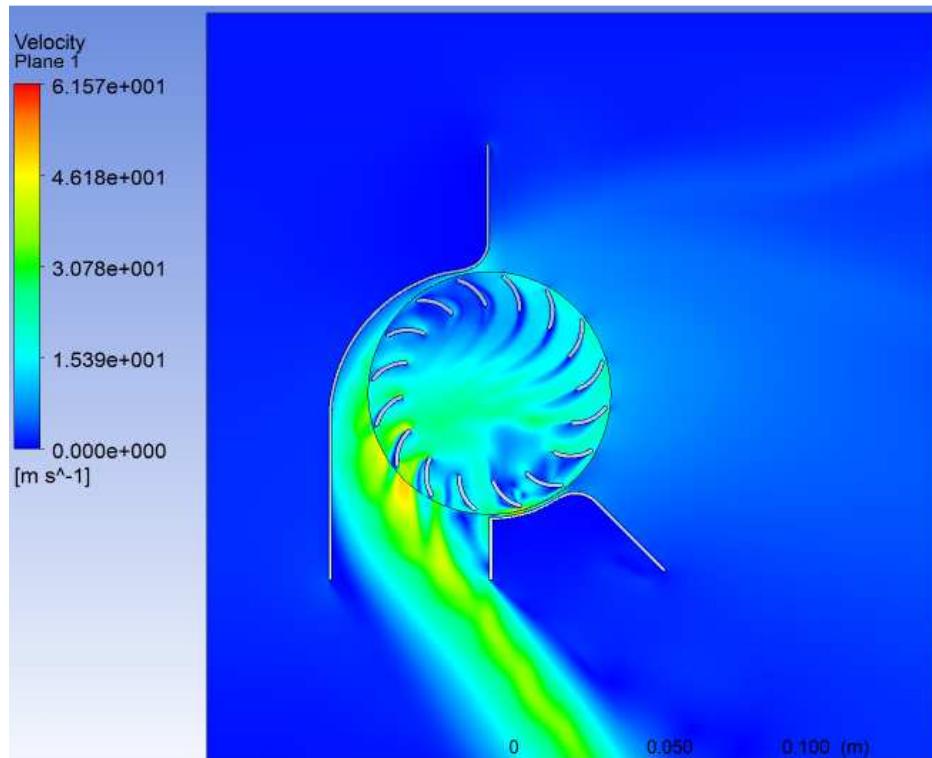


Figure 106. Velocity contour for 78 mm gap CFF configuration at 5,000 rpm

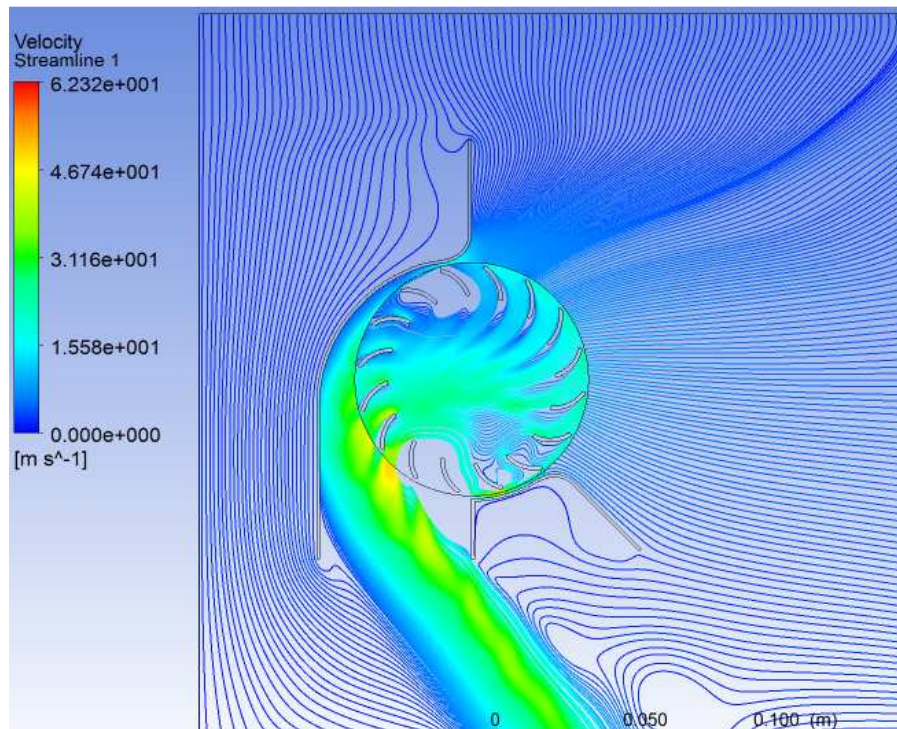


Figure 107. Velocity streamline for 78 mm gap CFF configuration at 5,000 rpm

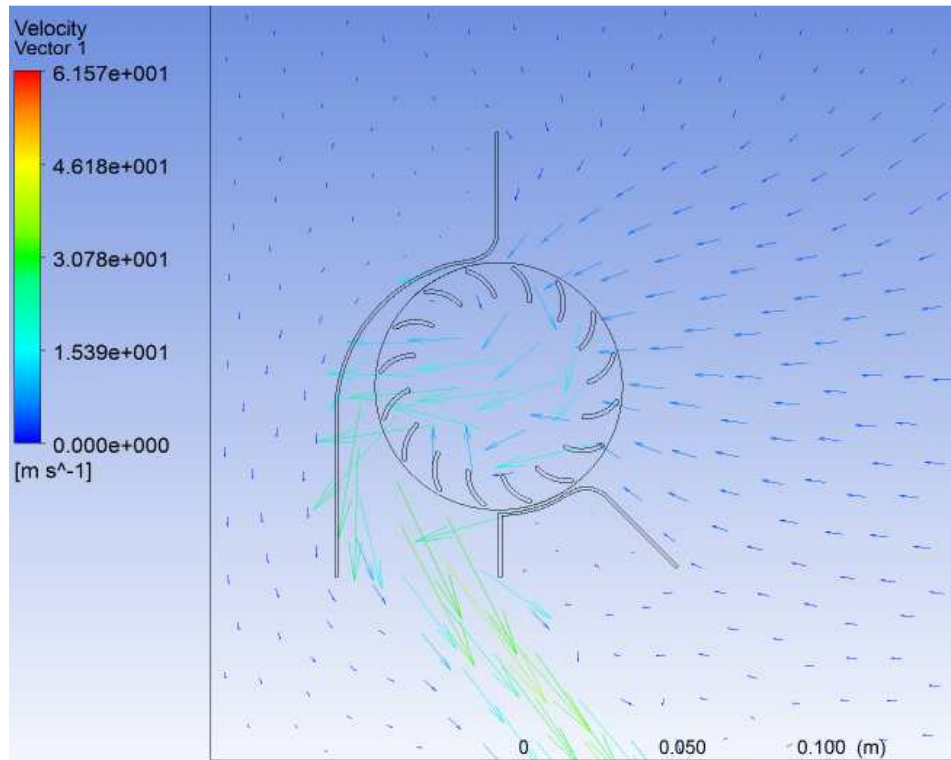


Figure 108. Velocity vector for 78 mm gap CFF configuration at 5,000 rpm

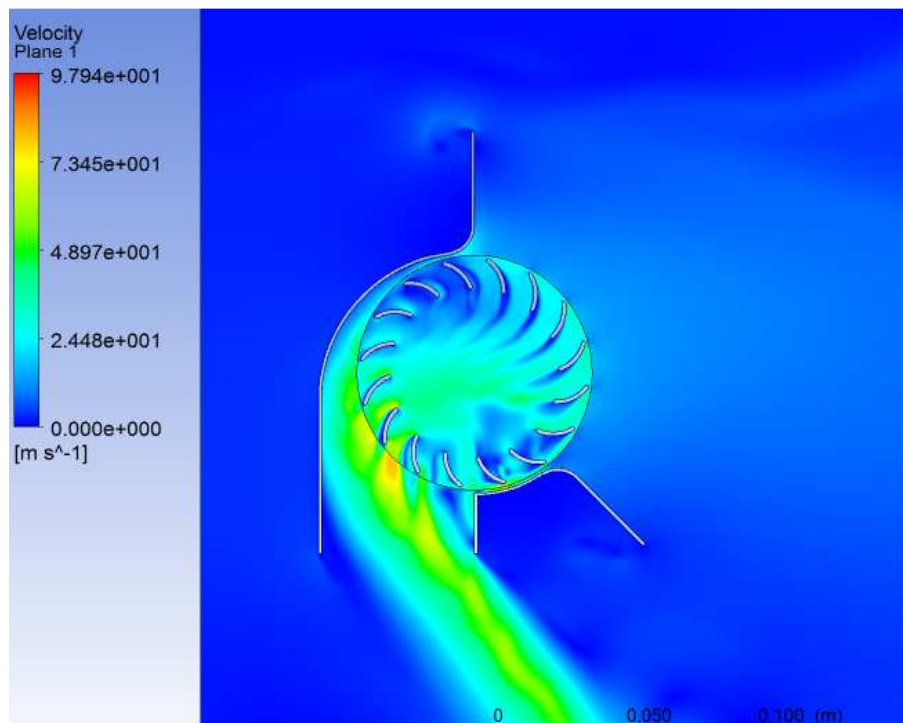


Figure 109. Velocity contour for 78 mm gap CFF configuration at 8,000 rpm

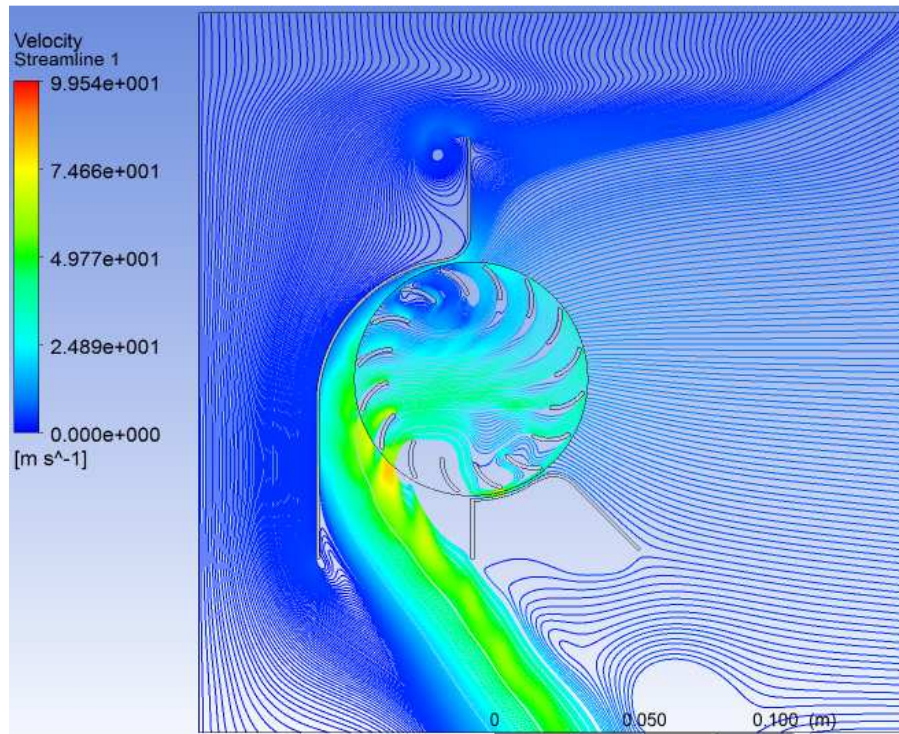


Figure 110. Velocity streamline for 78 mm gap CFF configuration at 8,000 rpm

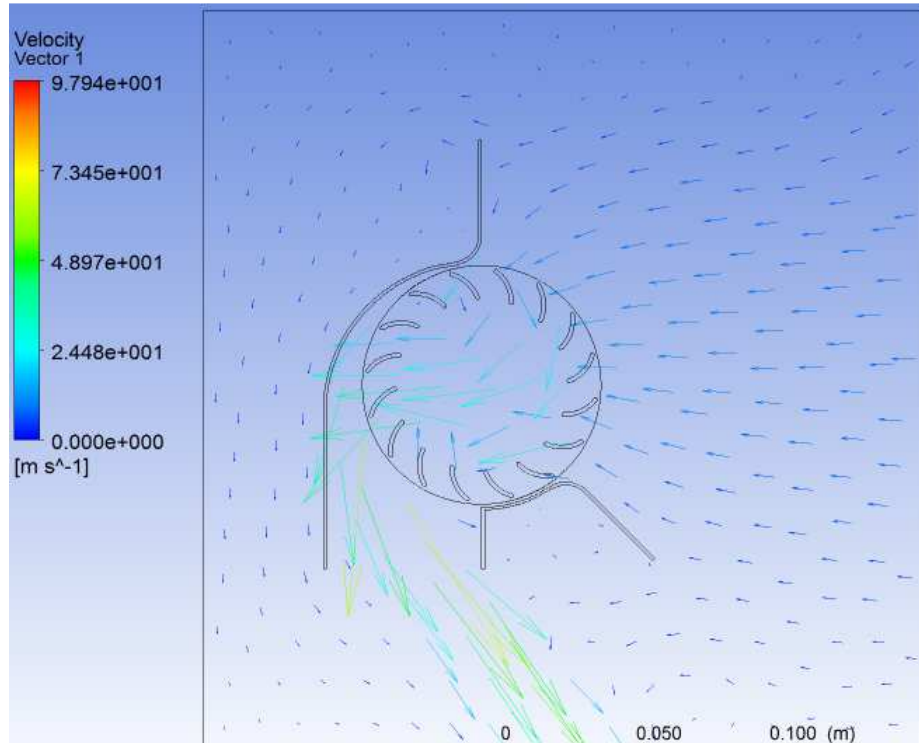


Figure 111. Velocity vector for 78 mm gap CFF configuration at 8,000 rpm

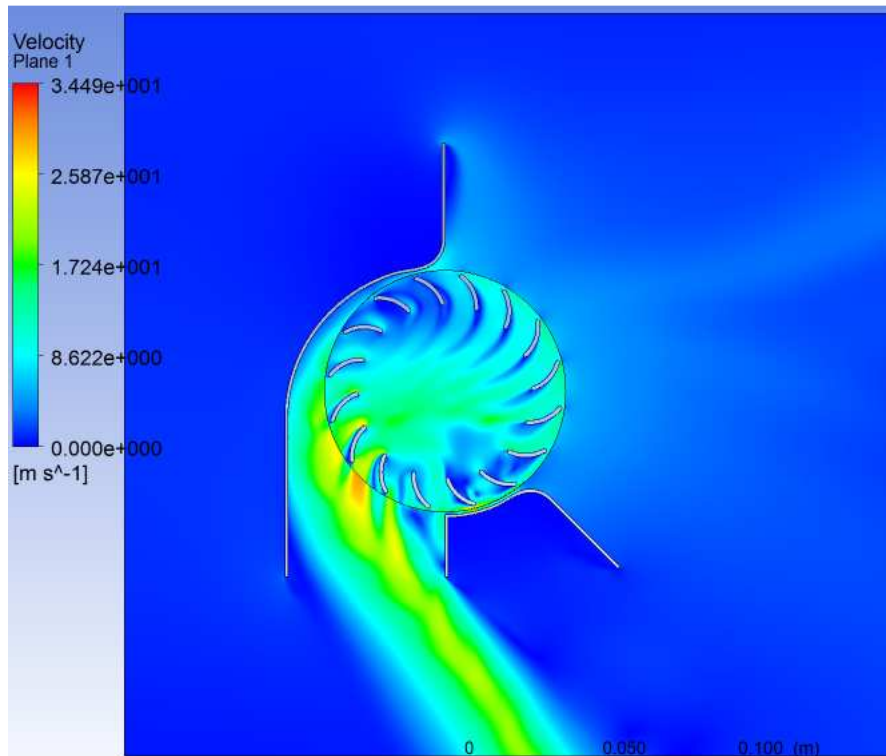


Figure 112. Velocity contour for 104 mm gap CFF configuration at 3,000 rpm

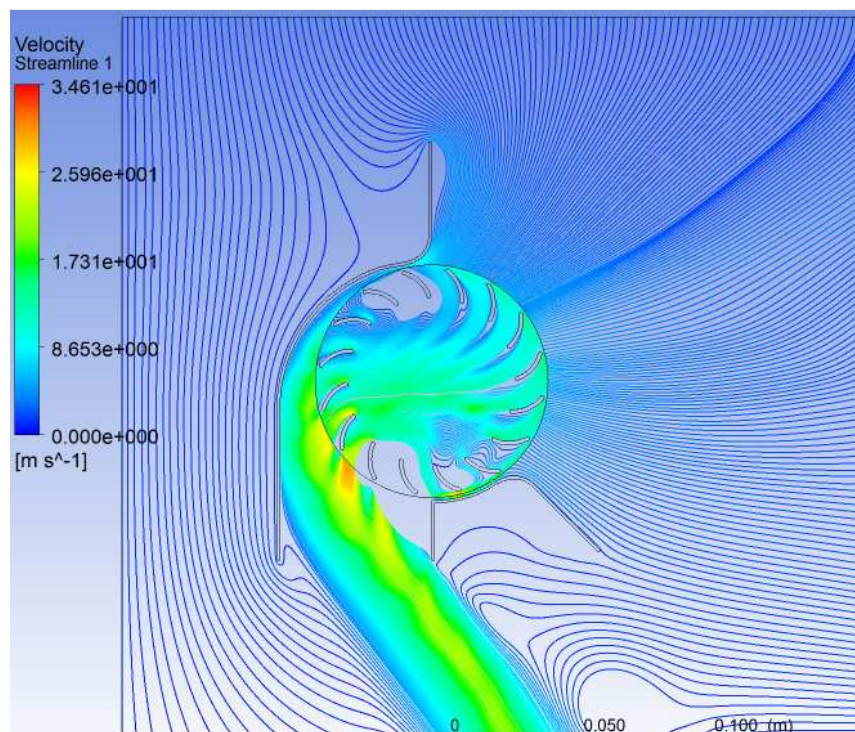


Figure 113. Velocity streamline for 104 mm gap CFF configuration at 3,000 rpm

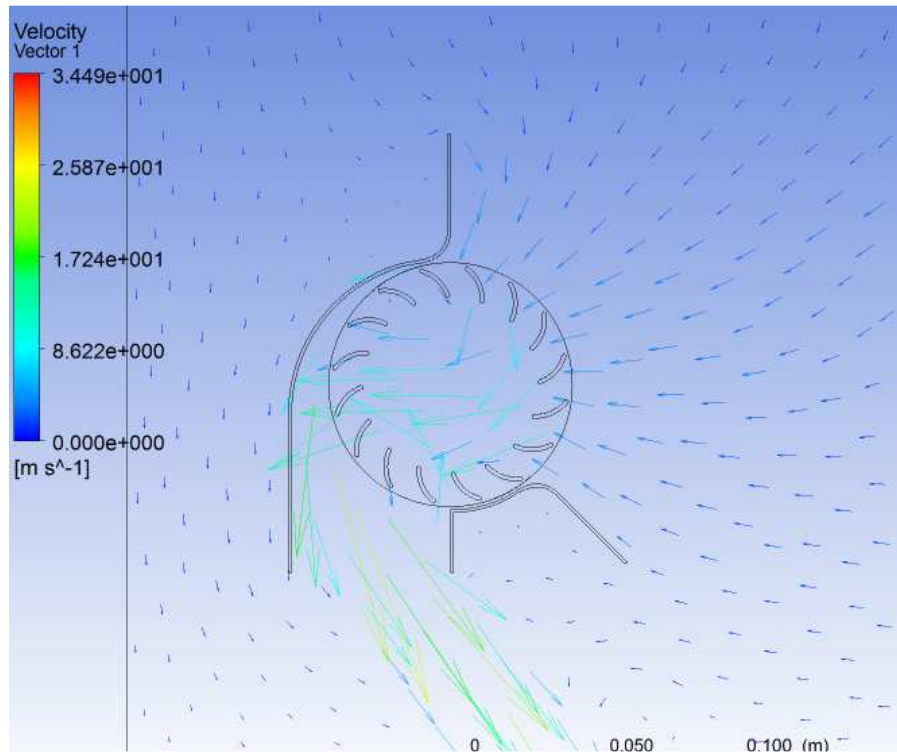


Figure 114. Velocity vector for 104 mm gap CFF configuration at 3,000 rpm

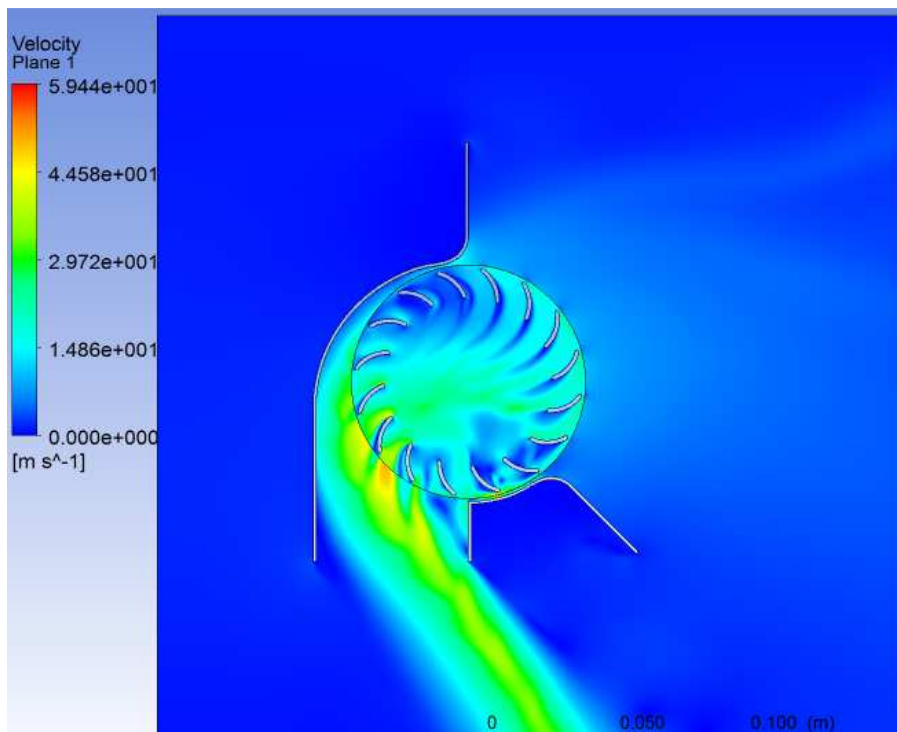


Figure 115. Velocity contour for 104 mm gap CFF configuration at 5,000 rpm

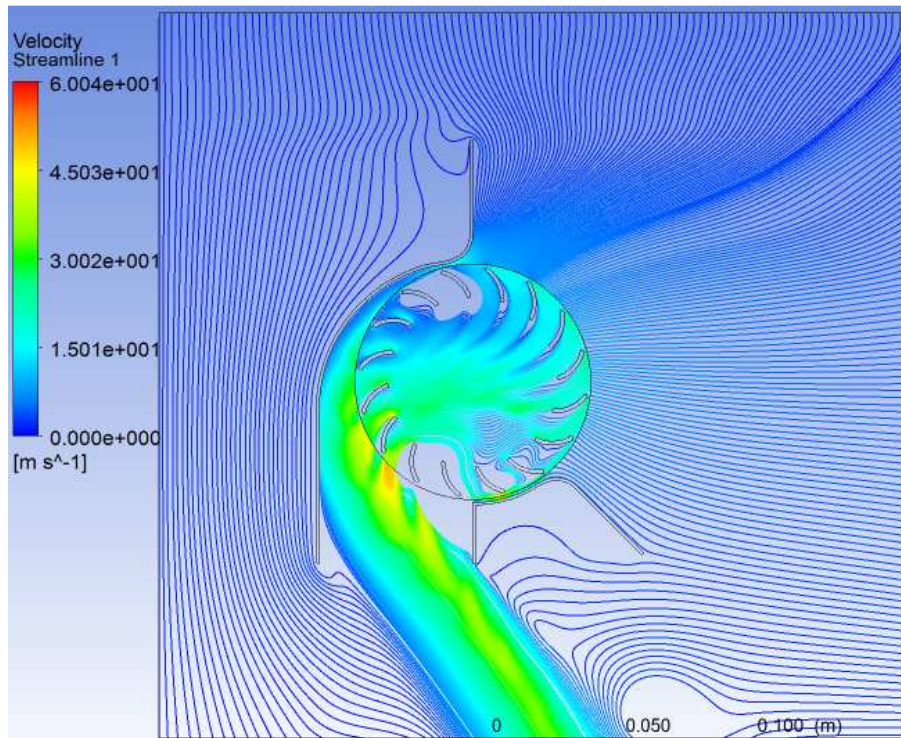


Figure 116. Velocity streamline for 104 mm gap CFF configuration at 5,000 rpm

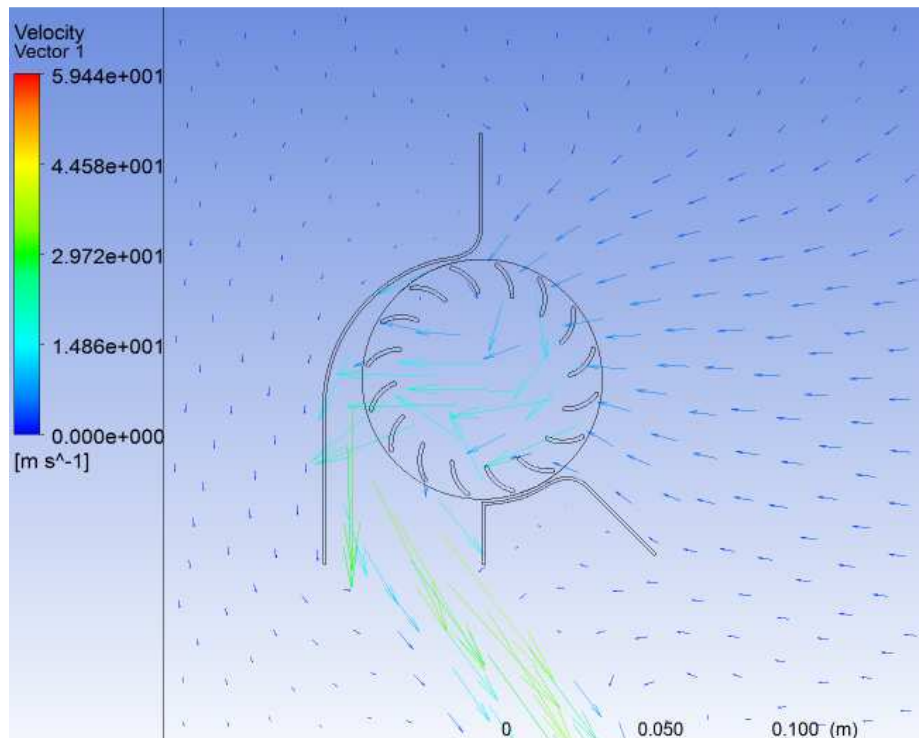


Figure 117. Velocity vector for 104 mm gap CFF configuration at 5,000 rpm

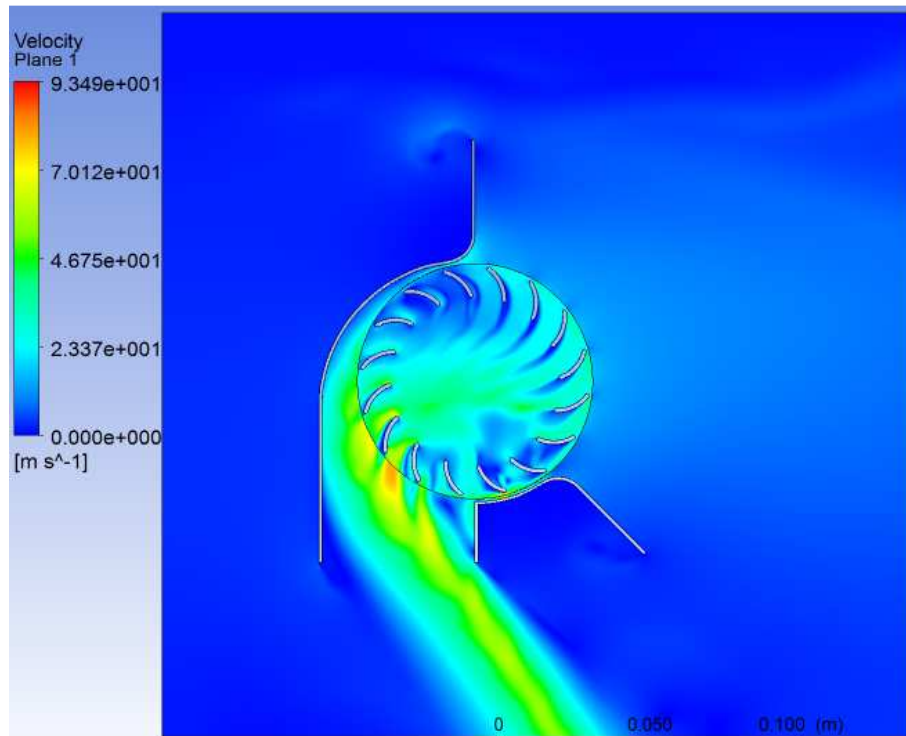


Figure 118. Velocity contour for 104 mm gap CFF configuration at 8,000 rpm

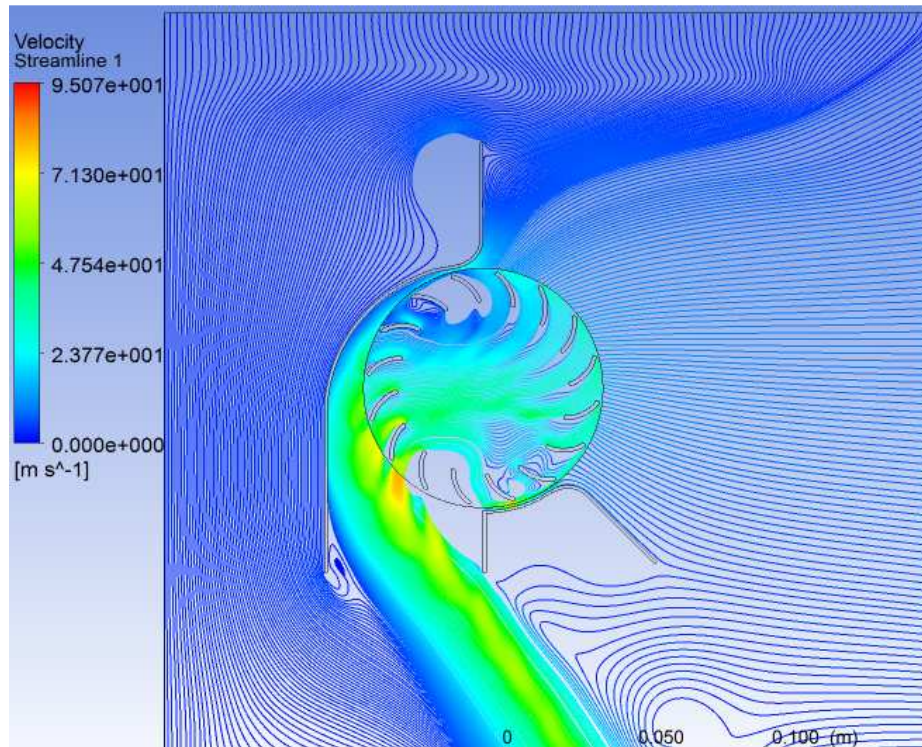


Figure 119. Velocity streamline for 104 mm gap CFF configuration at 8,000 rpm

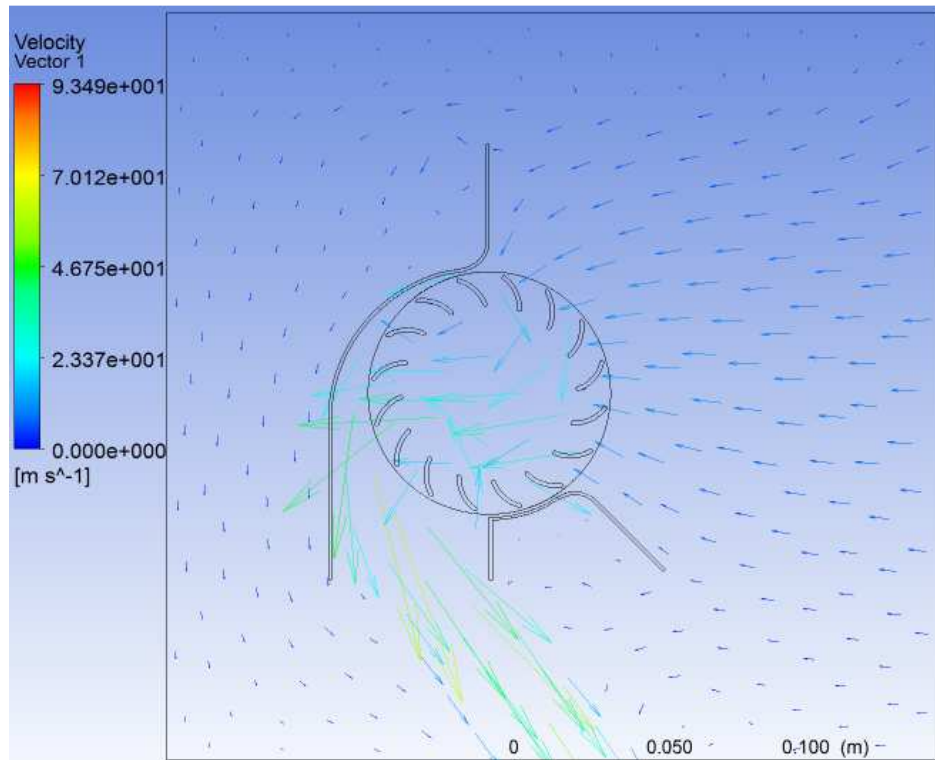


Figure 120. Velocity vector for 104 mm gap CFF configuration at 8,000 rpm

C. THRUST RESULTS

Table 13. Single DragonPlate CFF configuration simulation thrust results

SINGLE CFF CONFIGURATION				
Rotational Speed [rpm]	Thrust Per Unit Depth [N/mm]	Thrust (210mm Span) [N]	Thrust (420mm Span) [N]	% Difference From Experimental Results
3000	0.006802641	1.428554509	2.857109017	-28.62%
5000	0.015950757	3.349658888	6.699317777	-42.08%
8000	0.038786798	8.145227505	16.29045501	-42.64%

Table 14. 26 mm gap DragonPlate CFF configuration simulation thrust results

DUAL CFF CONFIGURATION (26 mm GAP)					
Rotational Speed [rpm]	Thrust Per Unit Depth [N/mm]	Thrust (1-Side) [N]	Thrust (Dual) [N]	Percentage Increase in Thrust [%]	% Difference From Experimental Results
3000	0.007201978	1.512415356	3.024830713	5.87%	-15.98%
5000	0.0201237	4.225976901	8.451953802	26.16%	-26.11%
8000	0.05180547	10.87914874	21.75829748	33.56%	-16.52%

Table 15. 52 mm gap DragonPlate CFF configuration simulation thrust results

DUAL CFF CONFIGURATION (52 mm GAP)					
Rotational Speed [rpm]	Thrust Per Unit Depth [N/mm]	Thrust (1-Side) [N]	Thrust (Dual) [N]	Percentage Increase in Thrust [%]	% Difference From Experimental Results
3000	0.007206136	1.513288607	3.026577214	5.93%	-13.09%
5000	0.020016308	4.203424606	8.406849211	25.49%	-19.91%
8000	0.05241879	11.00794596	22.01589192	35.15%	-14.96%

Table 16. 78 mm gap DragonPlate CFF configuration simulation thrust results

DUAL CFF CONFIGURATION (78 mm GAP)					
Rotational Speed [rpm]	Thrust Per Unit Depth [N/mm]	Thrust (1-Side) [N]	Thrust (Dual) [N]	Percentage Increase in Thrust [%]	% Difference From Experimental Results
3000	0.006921336	1.45348064	2.90696128	1.74%	-17.69%
5000	0.019186642	4.029194742	8.058389483	20.29%	-0.23%
8000	0.048516168	10.18839528	20.37679056	25.08%	-21.32%

Table 17. 104 mm gap DragonPlate CFF configuration simulation thrust results

DUAL CFF CONFIGURATION (104 mm GAP)					
Rotational Speed [rpm]	Thrust Per Unit Depth [N/mm]	Thrust (1-Side) [N]	Thrust (Dual) [N]	Percentage Increase in Thrust [%]	% Difference From Experimental Results
3000	0.006800048	1.428010039	2.856020079	-0.04%	-15.61%
5000	0.018520378	3.889279428	7.778558856	16.11%	-24.63%
8000	0.049180774	10.32796255	20.6559251	26.80%	-17.72%

APPENDIX F. DRAGONPLATE CFF EXPERIMENTAL RESULTS

Table 18. Single DragonPlate CFF configuration experimental thrust results

SINGLE CFF CONFIGURATION			
Rotational Speed [rpm]	Thrust Measured [g]	Thrust (Single) Calculated [N]	Thrust (2x) Calculated [N]
3000	178	1.746	3.492
5000	530	5.199	10.399
6000	769	7.544	15.088
8000	1325	12.998	25.997
8500	1475	14.470	28.940

Table 19. 26 mm gap DragonPlate CFF configuration experimental thrust results

26mm DUAL CFF CONFIGURATION			
Rotational Speed [rpm]	Thrust Measured [g]	Thrust Calculated [N]	Percentage Change in Thrust [%]
3000	329	3.227	-7.58%
5000	970	9.516	-8.49%
6000	1290	12.655	-16.12%
8000	2302.5	22.588	-13.11%
8500	2660	26.095	-9.83%
Average % Thrust Increase			-11.03%

Table 20. 52 mm gap DragonPlate CFF configuration experimental thrust results

52mm DUAL CFF CONFIGURATION			
Rotational Speed [rpm]	Thrust Measured [g]	Thrust Calculated [N]	Percentage Change in Thrust [%]
3000	340	3.335	-4.49%
5000	990	9.712	-6.60%
6000	1458	14.303	-5.20%
8000	2475	24.280	-6.60%
8500	2770	27.174	-6.10%
Average % Thrust Increase			-5.80%

Table 21. 78 mm gap DragonPlate CFF configuration experimental thrust results

78mm DUAL CFF CONFIGURATION			
Rotational Speed [rpm]	Thrust Measured [g]	Thrust Calculated [N]	Percentage Change in Thrust [%]
3000	342	3.350	-4.07%
5000	1007	9.874	-5.05%
6000	1438	14.110	-6.48%
8000	2486	24.388	-6.19%
8500	2743	26.912	-7.01%
Average % Thrust Increase			-6.18%

Table 22. 104 mm gap DragonPlate CFF configuration experimental thrust results

104mm DUAL CFF CONFIGURATION			
Rotational Speed [rpm]	Thrust Measured [g]	Thrust Calculated [N]	Percentage Change in Thrust [%]
3000	335	3.286	-5.90%
5000	1080	10.595	1.89%
6000	1540	15.107	0.13%
8000	2600	25.506	-1.89%
8500	2830	27.762	-4.07%
Average % Thrust Increase			-1.97%

Table 23. Thrust at various gap sizes for different rotational speeds

GAP SIZE [mm]	THRUST AT VARIOUS ROTATIONAL SPEEDS [N]				
	3000 rpm	5000 rpm	6000 rpm	8000 rpm	8500 rpm
26	3.227	9.516	12.655	22.588	26.095
52	3.335	9.712	14.303	24.280	27.174
78	3.350	9.874	14.110	24.388	26.912
104	3.286	10.595	15.107	25.506	27.762

Table 24. Percentage thrust increase at various gap sizes for different rotational speeds

GAP SIZE [mm]	% CHANGE IN THRUST AT VARIOUS ROTATIONAL SPEEDS [%]				
	<i>3000 rpm</i>	<i>5000 rpm</i>	<i>6000 rpm</i>	<i>8000 rpm</i>	<i>8500 rpm</i>
26	-7.58%	-8.49%	-16.12%	-13.11%	-9.83%
52	-4.49%	-6.60%	-5.20%	-6.60%	-6.10%
78	-4.07%	-5.05%	-6.48%	-6.19%	-7.01%
104	-5.90%	1.89%	0.13%	-1.89%	-4.07%

Table 25. Average percentage change in thrust at various gap sizes

GAP SIZE [mm]	AVERAGE % CHANGE IN THRUST [%]
26	-11.03%
52	-5.80%
78	-6.18%
104	-1.97%

THIS PAGE INTENTIONALLY LEFT BLANK

APPENDIX G. LARGER EXHAUST-GROUND DISTANCE DRAGONPLATE CFF EXPERIMENTAL RESULTS

Table 26. Single DragonPlate CFF configuration experimental thrust results (larger exhaust-ground distance)

SINGLE CFF CONFIGURATION			
Rotational Speed [rpm]	Thrust Measured [g]	Thrust (Single) Calculated [N]	Thrust (2x) Calculated [N]
3000	204	2.001	4.002
5000	589.5	5.783	11.566
6000	814.5	7.990	15.980
8000	1447.5	14.200	28.400
8500	1580	15.500	31.000

Table 27. 18 mm gap DragonPlate CFF configuration experimental thrust results (larger exhaust-ground distance)

18mm DUAL CFF CONFIGURATION			
Rotational Speed [rpm]	Thrust Measured [g]	Thrust Calculated [N]	Percentage Change in Thrust [%]
3000	377	3.698	-7.60%
5000	1120	10.987	-5.00%
6000	1604	15.735	-1.53%
8000	2780	27.272	-3.97%
8500	3100	30.411	-5.20%
Average % Thrust Increase			-4.66%

Table 28. 26 mm gap DragonPlate CFF configuration experimental thrust results (larger exhaust-ground distance)

26mm DUAL CFF CONFIGURATION			
Rotational Speed [rpm]	Thrust Measured [g]	Thrust Calculated [N]	Percentage Change in Thrust [%]
3000	367	3.600	-10.05%
5000	1166	11.438	-1.10%
6000	1548	15.186	-4.97%
8000	2657	26.065	-8.22%
8500	2975	29.185	-9.02%
Average % Thrust Increase			-6.67%

Table 29. 52 mm gap DragonPlate CFF configuration experimental thrust results (larger exhaust-ground distance)

52mm DUAL CFF CONFIGURATION			
Rotational Speed [rpm]	Thrust Measured [g]	Thrust Calculated [N]	Percentage Change in Thrust [%]
3000	355	3.483	-12.99%
5000	1070	10.497	-9.25%
6000	1537	15.078	-5.65%
8000	2639	25.889	-8.84%
8500	2926	28.704	-10.52%
Average % Thrust Increase			-9.45%

Table 30. 78 mm gap DragonPlate CFF configuration experimental thrust results (larger exhaust-ground distance)

78mm DUAL CFF CONFIGURATION			
Rotational Speed [rpm]	Thrust Measured [g]	Thrust Calculated [N]	Percentage Change in Thrust [%]
3000	360	3.532	-11.76%
5000	1072	10.516	-9.08%
6000	1540	15.107	-5.46%
8000	2640	25.898	-8.81%
8500	2965	29.087	-9.33%
Average % Thrust Increase			-8.17%

Table 31. 104 mm gap DragonPlate CFF configuration experimental thrust results (larger exhaust-ground distance)

104mm DUAL CFF CONFIGURATION			
Rotational Speed [rpm]	Thrust Measured [g]	Thrust Calculated [N]	Percentage Change in Thrust [%]
3000	345	3.384	-15.44%
5000	1052	10.320	-10.77%
6000	1459	14.313	-10.44%
8000	2559	25.104	-11.61%
8500	2845	27.909	-13.00%
Average % Thrust Increase			-12.25%

Table 32. Thrust at various gap sizes for different rotational speeds (larger exhaust-ground distance)

GAP SIZE [mm]	THRUST AT VARIOUS ROTATIONAL SPEEDS [N]				
	<i>3000 rpm</i>	<i>5000 rpm</i>	<i>6000 rpm</i>	<i>8000 rpm</i>	<i>8500 rpm</i>
18	3.698	10.987	15.735	27.272	30.411
26	3.600	11.438	15.186	26.065	29.185
52	3.483	10.497	15.078	25.889	28.704
78	3.532	10.516	15.107	25.898	29.087
104	3.384	10.320	14.313	25.104	27.909

Table 33. Percentage thrust increase at various gap sizes for different rotational speeds (larger exhaust-ground distance)

GAP SIZE [mm]	% CHANGE IN THRUST AT VARIOUS ROTATIONAL SPEEDS [%]				
	<i>3000 rpm</i>	<i>5000 rpm</i>	<i>6000 rpm</i>	<i>8000 rpm</i>	<i>8500 rpm</i>
18	-7.60%	-5.00%	-1.53%	-3.97%	-5.20%
26	-10.05%	-1.10%	-4.97%	-8.22%	-9.02%
52	-12.99%	-9.25%	-5.65%	-8.84%	-10.52%
78	-11.76%	-9.08%	-5.46%	-8.81%	-9.33%
104	-15.44%	-10.77%	-10.44%	-11.61%	-13.00%

Table 34. Average percentage change in thrust at various gap sizes (larger exhaust-ground distance)

GAP SIZE [mm]	AVERAGE % CHANGE IN THRUST [%]
18	-4.66%
26	-6.67%
52	-9.45%
78	-8.17%
104	-12.25%

THIS PAGE INTENTIONALLY LEFT BLANK

LIST OF REFERENCES

- [1] “VTOL,” in *Wikipedia*, <http://en.wikipedia.org/wiki/VTOL> [accessed August 5, 2012].
- [2] D. J. Allen, “The effects of rotor and casing geometry on the performance of cross-flow fans,” PhD dissertation, Durham University, Durham, United Kingdom, 1981.
- [3] “Mechanical Fans,” in *Wikipedia*, http://en.wikipedia.org/wiki/Mechanical_fan [accessed August 5, 2012].
- [4] D. H. Gossett, “Investigation of cross-flow fan propulsion for a lightweight VTOL aircraft,” M.S. thesis, Department of Aeronautics and Astronautics, Naval Postgraduate School, Monterey, California, March 2000.
- [5] V. Antoniadis, “Numerical and experimental investigation of performance improvements of a cross-flow fan,” M.S. thesis, Department of Mechanical and Aerospace Engineering, Naval Postgraduate School, Monterey, California, June 2010.
- [6] C. T. Delagrange, “Viability of cross-flow fan for vertical take-off and landing aircraft,” M.S. thesis, Department of Aeronautics and Astronautics, Naval Postgraduate School, Monterey, California, 2012.
- [7] J. Kummer, “Propulsive wing,” www.propulsivewing.com [accessed May 15, 2012].
- [8] “TP1430C Operating Manual,” in *Thunder Power RC*, <http://thunderpowerrc.com/html/documents/TP1430CManualandInputOutputchart.pdf> [accessed August 20, 2012].
- [9] “Quick Clinic - Thunder Power RC TP1430C, Programming and Operation” [video]. Available: <http://www.youtube.com/watch?v=5rL4vXjEtKc> [accessed August 20, 2012].

THIS PAGE INTENTIONALLY LEFT BLANK

INITIAL DISTRIBUTION LIST

1. Defense Technical Information Center
Ft. Belvoir, Virginia
2. Dudley Knox Library
Naval Postgraduate School
Monterey, California
3. Chairman, Code ME
Department of Mechanical and Aerospace Engineering
Naval Postgraduate School
Monterey, California
4. Professor Garth V. Hobson
Department of Mechanical and Aerospace Engineering
Naval Postgraduate School
Monterey, California
5. Research Assistant Professor Anthony Gannon
Department of Mechanical and Aerospace Engineering
Naval Postgraduate School
Monterey, California
6. Mr. Fong Saik Hay
CTO, Singapore Technologies Engineering Ltd
Singapore
7. Professor Yeo Tat Soon
Director, Temasek Defence Systems Institute
National University of Singapore
Singapore
8. Ms Tan Lai Poh
Senior Manager, Temasek Defence Systems Institute
National University of Singapore
Singapore